

Chemical inventory of the envelope of the Class I protostar L1551 IRS 5

P. Marchand¹, A. Coutens¹, J. Scigliuto^{1,2}, F. Cruz-Sáenz de Miera^{1,4}, A. Andreu¹, J.-C. Loison³, Á. Kóspál^{4,5,6}, P. Ábrahám^{4,5,7}

¹ Institut de Recherche en Astrophysique et Planétologie, Université de Toulouse, UT3-PS, CNRS, CNES, 9 av. du Colonel Roche, 31028 Toulouse Cedex 4, France

e-mail: pierre.marchand@irap.omp.eu

² Université Côte d'Azur, Observatoire de la Côte d'Azur, CNRS, Laboratoire Lagrange, France

³ Institut des Sciences Moléculaires (ISM), CNRS, Univ. Bordeaux, 351 cours de la Libération, F-33400 Talence, France

⁴ Konkoly Observatory, HUN-REN Research Centre for Astronomy and Earth Sciences, CSFK, MTA Centre of Excellence, Konkoly-Thege Miklós út 15-17, 1121 Budapest, Hungary

⁵ Institute of Physics and Astronomy, ELTE Eötvös Loránd University, Pázmány Péter sétány 1/A, 1117 Budapest, Hungary

⁶ Max Planck Institute for Astronomy, Königstuhl 17, 69117 Heidelberg, Germany

⁷ University of Vienna, Dept. of Astrophysics, Türkenschanzstr. 17, 1180, Vienna, Austria

ABSTRACT

Episodic accretion in protostars leads to luminosity outbursts that end up heating their surroundings. This rise in temperature pushes the snow lines back, enabling the desorption of chemical species from dust grain surfaces, which may significantly alter the chemical history of the accreting envelope. However, a limited number of extensive chemical surveys of eruptive young stars have been performed thus far. In the present study, we carry out a large spectral survey of the binary Class I protostar L1551 IRS 5, known to be a FUor-like object, in the 3mm and 2mm bands with the IRAM-30m telescope. As a result, we detected more than 400 molecular lines. The source displays a great chemical richness with the detection of 75 species, including isotopologues. Among these species, there are 13 hydrocarbons, 25 N-bearing species, 30 O-bearing species, 15 S-bearing species, 12 deuterated molecules, and a total of 10 complex organic molecules (I-C₄H₂, CH₃CCH, CH₂DCCH, CH₃CHO, CH₃CN, CH₃OCH₃, CH₃OCHO, CH₃OH, CH₂DOH, and HC₅N). With the help of local thermodynamic equilibrium (LTE) and non-LTE models, we determined the column densities of most molecules as well as excitation and kinetic temperatures. While most of those molecules trace the cold envelope ($\lesssim 20$ K), the OCS and CH₃OH emission arise from the warm (> 100 K) innermost ($< 2''$) regions. We compared the chemical inventory of L1551 IRS 5 and its column density ratios, including isotopic ratios, with other protostellar sources. A broad chemical diversity is seen among Class I objects. More observations with both single-dish telescopes and interferometers are needed to characterize the diversity in a larger sample of protostars, while more astrochemical models would help explain this diversity, in addition to the impact of luminosity outbursts on the chemistry of protostellar envelopes.

Key words. Astrochemistry, Stars: formation, ISM: molecules

1. Introduction

In low-mass star formation environments, chemical species are present in the gas phase, but also condensed at the surface of grains or trapped in ice mantles. As material falls closer to the protostar during the collapse of the envelope, the rise in temperature experienced by dust grains causes a thermal desorption of their icy mantle and, consequently, the release of new molecules in the gas phase (Ceccarelli et al. 2023). For example, CO and CH₄ thermally desorb at T $\sim 20\text{--}25$ K, while water sublimates above 100 K (Minissale et al. 2022). The sublimation of such species can trigger or impede gas phase reactions that affect the chemical content (e.g., a less efficient deuteration due to the destruction of H₃⁺ by CO, Vastel et al. 2006). Chemical species therefore show different spatial distributions in protostellar environments, and act as a proxy for the physical conditions of star formation (e.g., density, temperature, irradiation). The emission of relatively small molecules is usually detected at large scales, in cold protostellar envelopes. Conversely, water and complex organic molecules (COMs, i.e., molecules with carbon and at least six atoms) are very abundant in the gas phase in the warm

inner regions (~ 100 au) of low-mass protostars (e.g., Bottinelli et al. 2004). To fully understand how molecules are formed and destroyed in protostars, it is thus essential to characterize the chemical content at both small and large scales.

Single-dish telescopes are particularly suited to probe protostellar envelopes at large scale. This has been the focus of several observing programs with the Institut de RadioAstronomie Millimétrique (IRAM)-30m telescope. For example, the TIMASSS survey (Caux et al. 2011) has focused on the well-known Class 0 protostar IRAS 16293–2422. The ASAI large program (Lefloch et al. 2018) has surveyed several protostellar sources at different evolutionary stages, from prestellar cores to protoplanetary disks. Le Gal et al. (2020) also carried a spectral survey of seven Class I protostars with various physical properties. These studies provide chemical inventories and help us improve our understanding of the chemical processes at work in protostellar envelopes.

However, these above-mentioned surveys were directed toward relatively quiescent protostars, yet FUor sources are protostars that are known to experience bursts of accretion (Fischer

et al. 2023). Those lead to luminosity outbursts, which consequently warm up the protostellar envelope. The sudden increase in temperature can imply the thermal desorption of some key-species and potentially other changes in the chemical evolution of the system, even at the envelope scale (Visser et al. 2015; Rab et al. 2017).

In this work, we present a large spectral survey of the Class I FUor-like protostar L1551 IRS 5, performed with the IRAM-30m telescope at 3mm and 2mm. The objective is to compare its chemical content with other protostars. The paper is organised as follows. Section 2 describes the source and its observations. Section 3 presents the methodology of the analysis, the detected molecules, and their estimated column densities. We discuss those results and compare them with other surveys of quiescent protostars in Sect. 4. Section 5 presents our conclusions.

2. Observations

2.1. The source L1551 IRS 5

L1551 IRS 5 is a Class I proto-binary source (Looney et al. 1997) located in Taurus, at a distance of 141 ± 7 pc (Zucker et al. 2019). The northern and southern source ($M \approx 0.8 M_{\odot}$ and $M \approx 0.3 M_{\odot}$, respectively) (Liseau et al. 2005) are separated by $\sim 0.36''$ (~ 50 au) and have systemic velocities of ~ 9 km s $^{-1}$ and 6 km s $^{-1}$, respectively (Bianchi et al. 2020; Andreu et al. 2023). They each possess a circumstellar disk and are embedded in a ~ 300 au circumbinary disk (Cruz-Sáenz de Miera et al. 2019), which is itself embedded in a 2500 au to 8000 au scale collapsing envelope (Ohashi et al. 1996; Osorio et al. 2003) with a systemic velocity of ~ 6.4 km s $^{-1}$ (Chou et al. 2014; Mercimek et al. 2022). Based on its optical and near-infrared spectra, it has been classified as a FUor-like source (Connelley & Reipurth 2018, and references therein), suggesting that it experienced a surge of accretion leading to a luminosity outburst. The temperature increase induced by the luminosity outburst could explain the water detection towards the northern component with NOEMA (Andreu et al. 2023) and the reason why this low-mass protostar is one of the few Class I sources with a rich complex organic chemistry in its inner regions (Bianchi et al. 2020; Cruz-Sáenz de Miera et al. in prep.). However, the chemical composition of its envelope has been poorly known. Beside several dynamical studies of tracers such as ^{13}CO and CS (Kaifu et al. 1984; Ohashi et al. 1996; Fridlund et al. 2002; Chou et al. 2014; Takakuwa et al. 2020), few chemical surveys have been carried out to date. L1551 IRS 5 was observed by Roberts et al. (2002) with the NRAO 12m radio-telescope, and by Jørgensen et al. (2004) using the Onsala 20m radio-telescope and the 15m James Clerk Maxwell Telescope (JCMT). Both studies focused only on a few of the brightest species. More recently, Mercimek et al. (2022) performed a comparative survey including this source, using the IRAM-30m telescope at frequencies above 200 GHz. IRAM-30m deep surveys at 3mm and 2mm of this source are still lacking. We find that by probing larger scales with lower frequency observations, such surveys ought to provide more clues on the characterization of its colder gas.

2.2. Description of observations

Observations were carried out with the IRAM-30m telescope (projects 047-22 and 115-22) with the Eight MIXer Receivers (EMIR) in band E0 (3mm) and E1 (2mm). The telescope beam was centered on $\alpha_{J2000} = 04:31:34.161$, $\delta_{J2000} = +18:08:04.722$.

The large extent of the beam at those frequencies, from $16''$ (~ 2300 au) in the E1 band, to $35''$ (~ 5100 au) in the E0 band, is ideal to study the cold envelope. We used the position-switching (PSW) mode with an off-source reference located at a $(0, -900)''$ offset. The wide mode of the Fast Fourier Transform Spectrometer (FTS) provides a 2×8 GHz coverage for each setup with a resolution of 200 kHz (0.4 to 0.7 km s $^{-1}$). The E0 band has been entirely covered with the frequency range 71.75–115.75 GHz. In addition, we probed the ranges 135.25–143.25 GHz and 151.25–159.25 GHz in the E1 band.

We used complementary observations of the source in the frequency range 143.389–147.029 GHz (project 080-16), at the same coordinates. The off-source reference for the PSW mode in this case is located at a $(0, -300)''$ offset. For those observations, the fine mode of the FTS (50 kHz resolution) was used.

The observations were divided into six setups that are summarized in Table 1 with the dates of observations. Pointing and focusing were done on Mars, that was close to the source for all observations. Both vertical and horizontal polarisations were observed at the same time.

We reduced the data using CLASS from the GILDAS¹ package (Gildas Team 2013). The baselines were subtracted before the averaging of the spectra. We also averaged the vertical and horizontal polarizations. The data observed with a 50 kHz resolution were smoothed to match the spectral resolution of the other observations (200 kHz). The achieved noise levels are indicated in Table 1. The line identification and some of the analysis have been done with the CASSIS² software, using the CDMS (Müller et al. 2001, 2005) and JPL (Pickett et al. 1998) spectroscopic databases.

3. Results

3.1. Line identification and spectral fitting

The full reduced spectrum is displayed in Fig. 1. With a signal-to-noise ratio (S/N) criterion of 3rms , we detected 403 lines. Hyperfine structure transitions were counted as only one line when blended, which accounts for 80 more transitions. We identified 75 species, 37 of which are main isotopologues and 38 are secondary isotopologues. We detect 68 organic species including 13 hydrocarbons, 25 nitrogen-bearing species, 30 oxygen-bearing species, 15 sulfur-bearing species, and 12 deuterated molecules. 10 species are COMs, namely $1\text{-C}_4\text{H}_2$, CH_3CCH , CH_2DCCH , CH_3CHO , CH_3CN , CH_3OCH_3 , CH_3OCHO , CH_3OH , CH_2DOH , and HC_5N . The non-organic species are NH_2D , N_2H^+ , N_2D^+ , NS , SO , ^{34}SO , and SO_2 . We report two unidentified lines above 5rms , at 80.4805 GHz and 135.2495 GHz.

Each transition line has been fitted with a Gaussian curve using the Levenberg-Marquardt scheme of CASSIS, to obtain its full width at half maximum (FWHM), peak velocity, v , and peak intensity, Int . All lines, their properties, their fitting parameters, and their Gaussian fluxes with uncertainties are listed in Table A.1. The Gaussian flux, F , and its uncertainty, δF , are calculated

¹ <https://www.iram.fr/IRAMFR/GILDAS>

² CASSIS (<http://cassis.irap.omp.eu/>) has been developed by IRAP-UPS/CNRS

Table 1: Setup summary. For setups 1 to 4, two frequency ranges were observed at the same time, with the EO: [LO+LI]+[UI+UO] receiver for setups 1 and 2; E0/E1: [LO+LI] for setup 3 and 4; and E1: [LO+LI] for setups 5 and 6.

Setup	Freq. range 1 (GHz)	Freq. range 2 (GHz)	On-source time (h)	Resolution (kHz)	rms (mK) ^a	Date of observation
1	83.75-91.75	99.75-107.75	2.5	200	3.8	2022-10-10
2	91.75-99.75	107.75-115.75	3.33	200	4.0, 8.5 ^b	2022-09-01, 2022-10-10
3	71.75-79.75	151.25-159.25	4.0	200	3.8, 5.0 ^c	2022-09-01
4	79.75-87.75	135.25-143.25	2.0	200	6.0, 15.7 ^c	2023-02-14
5	143.389-145.210	–	0.7	50	17.0	2017-03-05
6	145.210-147.029	–	0.7	50	17.0	2017-10-20

Notes. ^a for a 200 kHz spectral resolution. ^b For frequencies larger than ~ 113 GHz. ^c For frequency range 2.

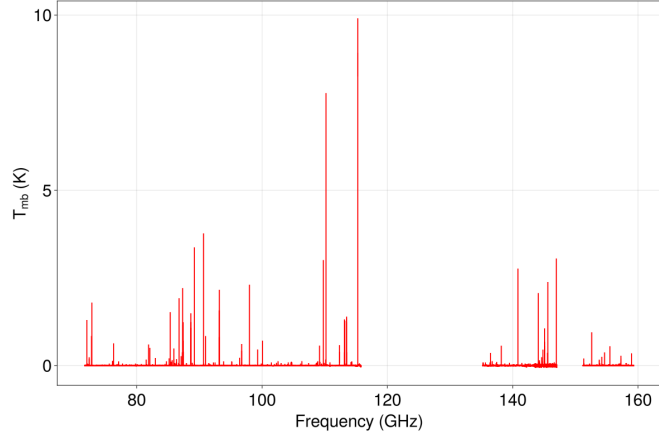


Fig. 1: Spectrum observed towards L1551 IRS 5 by the IRAM-30m telescope as part of this study. The line intensity is displayed in main beam temperature.

as:

$$F = \sqrt{\frac{\pi}{4 \ln 2}} Int \times FWHM, \quad (1)$$

$$\delta_F = F \sqrt{\left(\frac{\delta FWHM}{FWHM}\right)^2 + \left(\frac{\delta Int}{Int}\right)^2}, \quad (2)$$

where $\delta FWHM$ and δInt are the one sigma uncertainties on the FWHM and the peak intensity. If several transitions of the same species are blended into one apparent line, we used the same fit for all the transitions (indicated by ‘-’ instead of numbers for the FWHM, intensity, and flux in the tables). Several OCS and CH₃OH lines clearly exhibit at least two separated components, each of which were fit with a Gaussian profile. Table 2 summarizes the number of lines detected for each species, with the minimum and maximum upper energy level, E_{up} , of those transitions.

Figure 2 displays the FWHM and peak velocity of the fitted lines. Most lines are centered around ~ 6.5 km s⁻¹, close to the estimated source systemic velocity of ~ 6.4 km s⁻¹ (Mercimek et al. 2022), and have a width of ~ 1 km s⁻¹. There is however a group centered around ~ 9 km s⁻¹, composed of CH₃OH, CH₂DOH, OCS, and OC³⁴S. Several lines of these species actually exhibit doubly peaked profiles at ~ 6.5 km s⁻¹ and ~ 9 km s⁻¹, with the latter likely tracing the northern source as determined by ALMA and NOEMA observations (Bianchi et al. 2020; Andreu et al. 2023; Cruz-Sáenz de Miera et al. in prep.). The two components are probably not always clearly separated,

resulting in seemingly broad widths (≥ 3 km s⁻¹) for other lines of CH₃OH and OC³⁴S.

Likewise, we display the upper energy level E_{up} of the transitions as a function of the velocity shift in Fig. 3. The number of detected lines smoothly declines above 20 K, but varies more randomly below this energy level. This is partly due to the numerous hyperfine components of CN, ¹³CN, N₂H⁺, and N₂D⁺ creating peaks around 4 K, 6 K, and 11 K. At 6.4 km s⁻¹, points are distributed at all E_{up} values, from 3 K to ~ 200 K. However, most lines at ~ 9 km s⁻¹ have an E_{up} larger than 20 K. Above 100 K, there are more lines centered around 9 km s⁻¹ than 6.4 km s⁻¹. This suggests that this velocity regime traces hotter, and likely inner, emission, in agreement with interferometric studies (Bianchi et al. 2020; Andreu et al. 2023). Finally, we also display the FWHM as a function of E_{up} in Fig. 4. The FWHM remains nearly constant around ~ 1 km s⁻¹ for $E_{up} < 100$ K. Nonetheless, nearly all $E_{up} > 100$ K have FWHM $\gtrsim 2$ km s⁻¹, which is broader than the vast majority of the other lines, and could be related to the presence of emission at both ~ 6.4 and ~ 9 km s⁻¹.

3.2. Excitation temperatures and column densities

We used radiative transfer modeling, assuming both local thermodynamic equilibrium (LTE) and non-LTE, to determine the column densities of the detected species, using the spectroscopic data of the CDMS and JPL databases.

3.2.1. LTE modeling

In the LTE case, the lines were fitted with a Python code (Botinelli 2024). It uses the Levenberg-Marquardt scheme of the Python package lmfit with a least-squares method, based on the line intensity equation:

$$I(\nu) = \eta [J(\nu, T_{ex}) (1 - e^{-\tau(\nu)}) - J(\nu, T_{CMB}) (1 - e^{-\tau(\nu)})], \quad (3)$$

with

$$J(\nu, T) = \frac{h\nu}{k_B (e^{\frac{h\nu}{k_B T}} - 1)}, \quad (4)$$

$$\tau(\nu) = \tau_0 \exp \left[- \left(\frac{\nu - \nu_0}{\nu_0 (FWHM/c)} \right)^2 4 \ln(2) \right], \quad (5)$$

$$\tau_0(\nu, T_{ex}) = \frac{c^3 A_{ij} n_{up}(T_{ex}) (e^{\frac{h\nu}{k_B T_{ex}}} - 1)}{4\pi\nu_0^3 FWHM \sqrt{\pi/\ln(2)}}, \quad (6)$$

$$n_{up}(T_{ex}) = \frac{N_{tot} g_{up}}{Q(T_{ex}) e^{\frac{E_{up}}{k_B T_{ex}}}}. \quad (7)$$

Table 2: Chemical species detected in our survey, with the number of detected lines and minimum and maximum upper energy levels, E_{up} , of the transitions.

Species	Lines	$E_{\text{up,min}}$	$E_{\text{up,max}}$	Species	Lines	$E_{\text{up,min}}$	$E_{\text{up,max}}$
CCH	6	4.2	4.2	HC^{15}N	1	4.1	4.1
CCD	10	3.5	10.4	HNC	1	4.4	4.4
C^{13}CH	5	4.1	4.1	DNC	2	3.7	11.0
CCS	16	15.4	57.2	HN^{13}C	1	4.2	4.2
C_3H	8	7.8	12.5	H^{15}NC	1	4.3	4.3
c-C ₃ H	3	4.4	4.4	HNCO	3	10.6	29.5
c-C ₃ H ₂	14	6.4	82.6	HCO	4	4.2	4.2
c-C ₃ HD	12	5.7	22.5	HCO^+	1	4.3	4.3
c-CC ¹³ CH ₂	4	6.3	15.8	DCO ⁺	2	3.5	10.4
l-C ₃ H ₂	5	15.0	28.5	H^{13}CO^+	1	4.2	4.2
C_3N^a	5	17.1	26.1	HC^{18}O^+	1	4.1	4.1
C_3O	4	16.6	30.5	HC^{17}O^+	1	4.2	4.2
C_3S	4	25.2	47.4	D^{13}CO^+	1	10.2	10.2
C_4H^a	14	16.4	62.1	HC_3N	8	15.7	66.8
l-C ₄ H ₂	7	23.6	46.8	DC_3N	5	18.2	36.9
CH ₃ CCH	12	12.3	65.8	H^{13}CCCN	2	19.0	23.3
CH ₂ DCCH	2	16.3	21.7	HC^{13}CCN	2	23.9	33.9
CH ₃ CHO	23	5.0	42.5	HCC^{13}CN	4	15.6	28.7
CH ₃ CN	8	8.8	132.8	HC_5N	15	48.3	115.4
CH ₃ OCH ₃ ^a	1	40.4	40.4	H_2CO	3	3.5	21.9
CH ₃ OCHO	3	20.2	56.6	D_2CO	1	13.4	13.4
CH ₃ OH	46	7.0	233.6	H_2^{13}CO	4	4.3	22.4
CH ₂ DOH	7	6.4	25.8	H_2CCO	8	9.7	40.5
CN	9	5.4	5.4	HCS^+	1	6.1	6.1
¹³ CN	15	5.2	5.2	H_2CS	6	9.9	29.9
¹⁵ N	3	5.3	5.3	$\text{H}_2\text{C}^{33}\text{S}$	1	22.8	22.8
CO	1	5.5	5.5	HOCO^+	2	10.3	15.4
¹³ CO	1	5.3	5.3	HO CN	2	10.1	15.1
¹⁷ O ^a	2	5.4	5.4	NH_2D^a	10	20.7	21.3
¹⁸ O	1	5.3	5.3	$\text{N}_2\text{H}^+{}^a$	3	4.5	4.5
¹³ C ¹⁸ O	1	5.0	5.0	$\text{N}_2\text{D}^+{}^a$	5	3.7	11.1
CS	2	7.0	14.1	NS	1	8.9	8.9
¹³ CS	2	6.7	13.3	OCS	12	12.3	53.1
³³ S	1	7.0	7.0	OC^{34}S	1	25.6	25.6
³⁴ S	2	6.9	13.9	SO	6	9.2	38.6
HCN	3	4.2	4.2	³⁴ SO	2	9.1	15.6
DCN ^a	6	3.5	10.4	SO ₂	5	7.7	54.7
H^{13}CN	3	4.1	4.1				

Notes. ^a Species with one or several lines that are made of several transitions.

Here, ν is the frequency, η the filling factor, n_{up} the upper-level population, g_{up} the upper-level degeneracy, Q the partition function, E_{up} the upper-level energy, A_{ij} the spontaneous emission Einstein coefficient, $FWHM$ the full width at half maximum of the line in the velocity space, v_0 the frequency of the transition, T_{ex} the excitation temperature, $T_{\text{CMB}} = 2.7$ K, N_{tot} the column density, and τ the optical depth. Also, η is linked to the source size θ_s by:

$$\eta = \frac{\theta_s^2}{\theta_s^2 + \theta_B^2}, \quad (8)$$

where θ_B is the telescope beam size. Equation (3) is valid for a negligible continuum. N_{tot} , T_{ex} , θ_s , and $FWHM$ are unknowns and are used as parameters for the fit. We first fit the species showing transitions spanning several E_{up} values. When possible, for species with only one transition, we lift the degeneracy of

the parameters by assuming the excitation temperature derived for an isotopologue. Indeed, we independently find similar excitation temperatures for c-C₃H₂ and c-C₃HD (~ 10 K), HC₃N, and its D and ¹³C isotopologues (~ 20 K), and CS and C³⁴S (~ 10 K). When taking the error intervals into account, the only exception is ¹³CS that seems to show a lower excitation temperature (4.9 K) than CS (9.0 K). Assuming a temperature of 9.0 K for ¹³CS results in a less accurate fit and a 40% lower column density. For several molecules, the partition function data is unavailable below 9.375 K. In that case, we extrapolated the partition function at lower temperatures, assuming a power law in log space (correlation coefficient > 0.99 in every case). The resulting T_{ex} , N_{tot} , and θ_s (with their uncertainties) are listed in columns 2 to 4 of Table 3. All lines were fitted with a single component, except CH₃OH (see Sect. 3.2.3) and OCS. Uncertainties (indicated in parenthesis) are given by lmfit and correspond to a 1σ confidence interval. We show all excitation temperatures derived us-

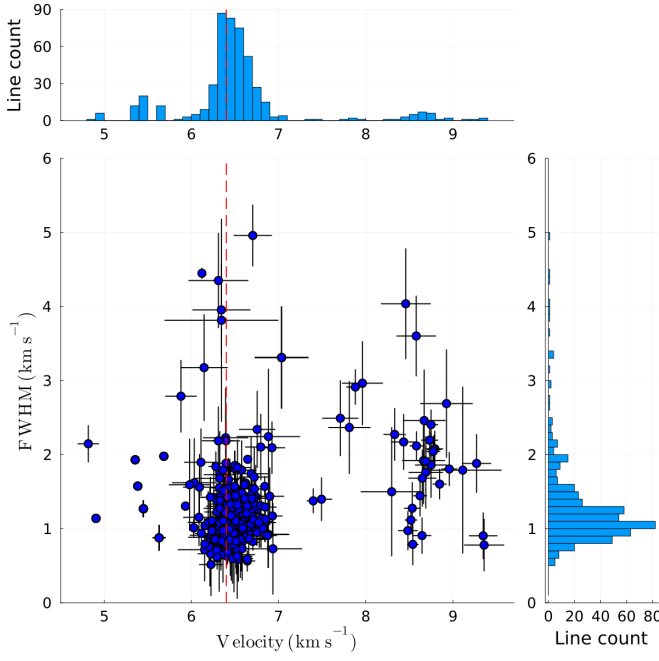


Fig. 2: FWHM as a function of the Doppler shift velocity for all the detected lines, obtained through Gaussian fitting (bottom-left). The dashed red line indicates the envelope local standard of rest velocity of 6.4 km s^{-1} . The top and right panels represent histograms of the line count for the Doppler shift velocity and the FWHM, respectively.

ing $\geq 2 E_{\text{up}}$ values, sorted by increasing T_{ex} , in Fig. 5. Fitting the emission of a species using a low number ($\lesssim 3$) of E_{up} is easier than with a larger number of E_{up} , as the latter may mathematically result in smaller confidence intervals. Therefore, we used different colors in Fig. 5 to illustrate the number of different E_{up} used to derive each excitation temperature. We also display the radiative transfer models for all species in Appendix B.

We also use CASSIS to perform rotational diagrams (Goldsmith & Langer 1999) for the species with more than two detected lines. All column densities found by fitting rotational diagrams agree within 20% with the fitting of line intensities, while most excitation temperatures agree within 25%. The exceptions are l-C₃H₂ (16.2 ± 3.7 K with the line intensity fitting vs 25.3 ± 3.8 K with the rotational diagram, respectively), CH₃CHO (8.3 ± 0.6 K vs 11.4 ± 0.9 K respectively), and H₂CO (18.4 ± 4.8 K vs 9.7 ± 3.6 K respectively). The values used in the rest of the paper are the ones obtained with the line intensity fitting method.

3.2.2. The case of OCS

Figure 6 shows the detected OCS transitions. The lines display broad ($\gtrsim 4 \text{ km s}^{-1}$) asymmetric profiles that can be fitted with two Gaussians, centered around $\sim 6.4 \text{ km s}^{-1}$ and $\sim 8.5 \text{ km s}^{-1}$. The narrow peak at 8.5 km s^{-1} is close to the velocity of the northern source (Bianchi et al. 2020; Andreu et al. 2023). We therefore model this emission using two components, one corresponding to the envelope and centered on the system velocity of 6.4 km s^{-1} , and a second one at 8.5 km s^{-1} . ALMA observations of L1551 IRS 5 by Bianchi et al. (2020) suggest that the size of the methanol emission region (the hot corino) is about $0.15''$. We therefore assume this source size for the second component. We fit the two components with the Levenberg-Marquardt

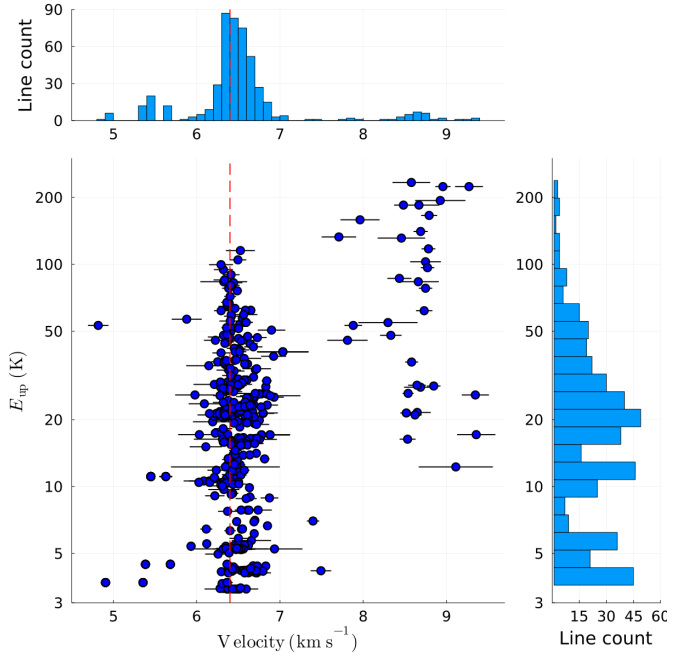


Fig. 3: Same as Fig. 2, for the E_{up} as a function of the Doppler shift velocity.

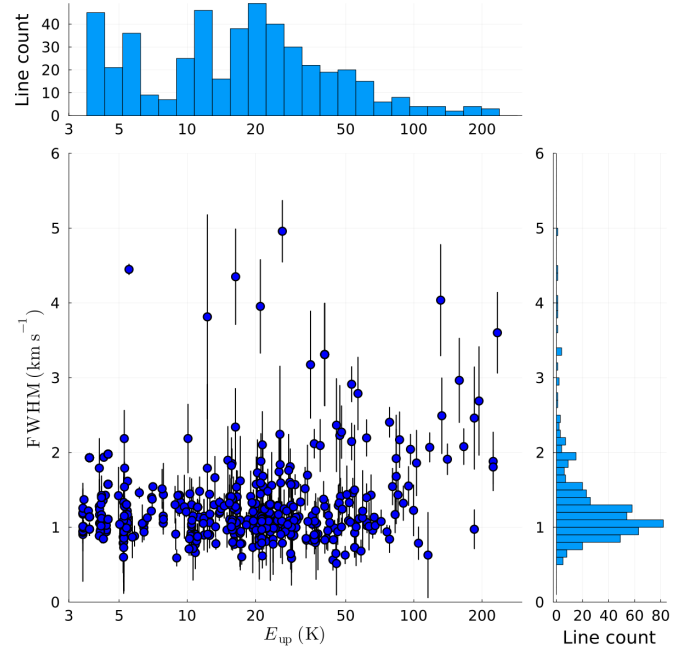


Fig. 4: Same as Fig. 2, for the FWHM as a function of the E_{up} .

scheme described above and display the model in red in Fig. 6. The results of the fit are quite uncertain. We find a size of $42.0 \pm 30.3''$ for the first component, with an excitation temperature of 98.0 ± 74.5 K, a FWHM of $4.8 \pm 0.2 \text{ km s}^{-1}$ and a column density of $(2.9 \pm 0.6) \times 10^{13} \text{ cm}^{-2}$. For the second component, we find a temperature of 400.9 ± 39.2 K and a column density of $(5.8 \pm 19.4) \times 10^{19} \text{ cm}^{-2}$. Although the model seems to reproduce the observation reasonably well, a nearly 100 K temperature at a scale of $40'' (> 5000 \text{ au})$ seems very unlikely. Moreover, the pa-

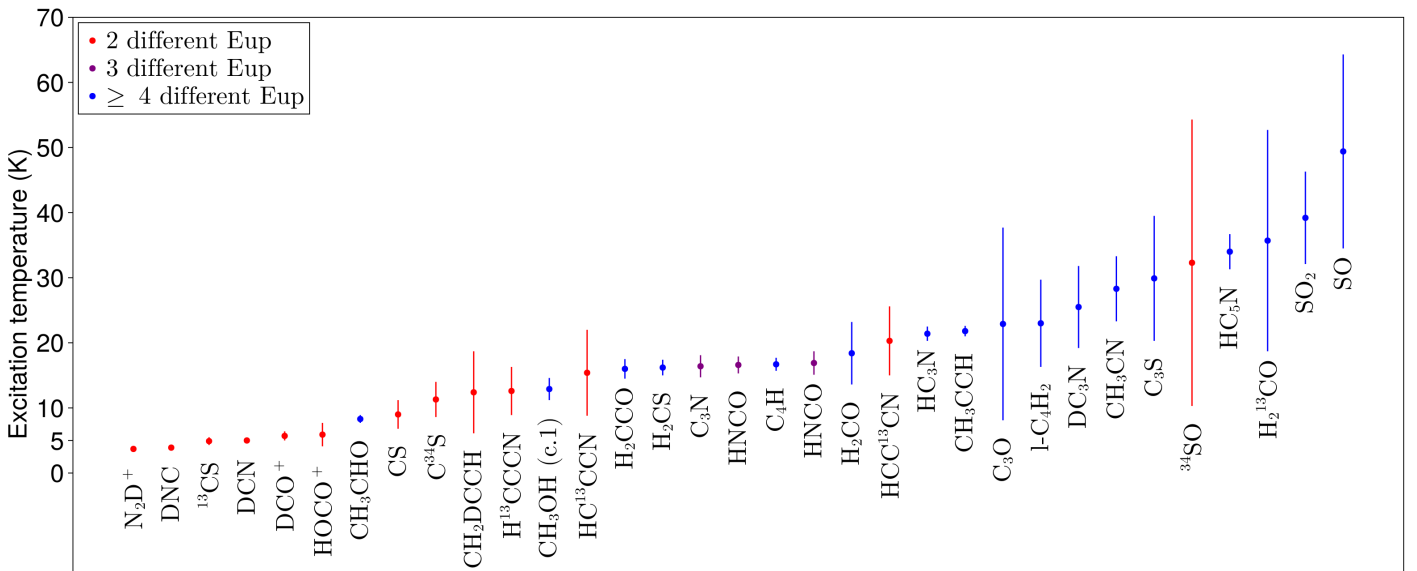


Fig. 5: Excitation temperatures derived for each species with our LTE modeling, excluding OCS that has a very high excitation temperature (see Sect. 3.2.1). The species are sorted by increasing excitation temperatures. The colors represent the number of different E_{up} available to derive the excitation temperatures: 2 (red), 3 (purple), and ≥ 4 (blue). The vertical lines represent the error bars.

rameters have large uncertainties. Those results therefore cannot be considered as reliable even if they seem to suggest a warm emission for OCS. With the IRAM-30m telescope, Mercimek et al. (2022) also observe broad OCS line profiles at higher frequencies (~ 220 GHz). They suggest that this emission originates from the 2'' circumbinary disk, as observed by Takakuwa et al. (2020) with ALMA at ~ 330 GHz.

3.2.3. The case of methanol

We detected 37 lines of methanol (CH₃OH), distributed into 28 lines showing a single peak profile, and 9 lines with a double peak profile. Accordingly, we have fitted those lines with one or two Gaussians. We were not able to model all lines using the LTE and non-LTE methods described above. Instead, we used CASSIS to plot and fit the rotational diagram, displayed in Fig. 7. We separated the lines in two groups. The blue points represent the component centered around the system velocity v_{lsr} of 6.4 km s⁻¹, while the red points are for the component centered around 8.5 km s⁻¹. The points in the first group all have $E_{\text{up}} < 100$ K, and forms a steep slope in the rotational diagram, indicative of a low excitation temperature. The linear regression on those points gives $T_{\text{ex}} = 12.9 \pm 1.7$ K and $N = (2.7 \pm 0.9) \times 10^{13}$ cm⁻². This emission likely originates from the cold envelope at large scale. The second group of points forms a very shallow slope and extends to $E_{\text{up}} > 200$ K, suggesting a hot emission. The velocity of 8.5 km s⁻¹ matches the northern source velocity. Following Bianchi et al. (2020), we therefore consider a $\theta_s = 0.15''$ emission region for the methanol in this source. The linear regression gives $T_{\text{ex}} = 273.6 \pm 161.2$ K and $N = (2.8 \pm 0.8) \times 10^{18}$ cm⁻², which is half an order of magnitude lower than the lower limit of 10¹⁹ cm⁻² derived by Bianchi et al. (2020) for CH₃OH in the northern source. However, the opacity of several of these excited lines is larger than 1, and the column density is consequently very probably underestimated. These two fits are listed in Table 3, with the labels "c.1" and "c.2."

We displayed the radiative transfer models of the lines combining those two fits in Fig. B.3. Overall, those parameters reproduced the emission poorly, with several lines either dimmer or significantly brighter than what is observed. Assuming different values for θ_s does not improve the results. Consequently, although it is fairly certain that the methanol emission can be decomposed into at least two components, namely, cold and hot, we did not use those fits in our further analysis.

3.2.4. Non-LTE modeling

We also carried out non-LTE models for the species with available collisional rate coefficients. We used the radiative transfer code Radex (van der Tak et al. 2007), assuming an expanding sphere geometry. The collision coefficients with H₂ (ortho, para or scaled from He) were taken from the Lamda, Basecol and EMAA databases (the references for each species are listed in the notes of Table 3). When both ortho and para-H₂ coefficients were available, we assumed an ortho/para ratio of 10⁻³, as long as the kinetic temperature remained below 20 K; otherwise we assumed the standard ratio at LTE (Faure et al. 2019). For each species, we run Radex for a grid of kinetic temperatures T_{kin} , column densities of the species N_{tot} , and number densities of the collider n(H₂). Each model gives an opacity and an excitation temperature for each transition that we use to reproduce the line profile using Equation (3). We choose parameters that reproduce the best our measured intensity on all lines for a given species, by minimizing the L2 norm of the weighted residuals:

$$\chi^2 = \sum_i \frac{(I_{\text{obs},i} - I_v(\theta))^2}{\sigma_i^2}. \quad (9)$$

Here, $I_{\text{obs},i}$ is the intensity in the spectral channel i of the transition lines, $I_v(\theta)$ is the modeled intensity calculated with the set of parameters θ following Equation (3), and σ_i^2 is the error on the intensity, calculated as

$$\sigma_i^2 = \text{rms}_i^2 + (\text{cal} \times I_{\text{obs},i})^2, \quad (10)$$

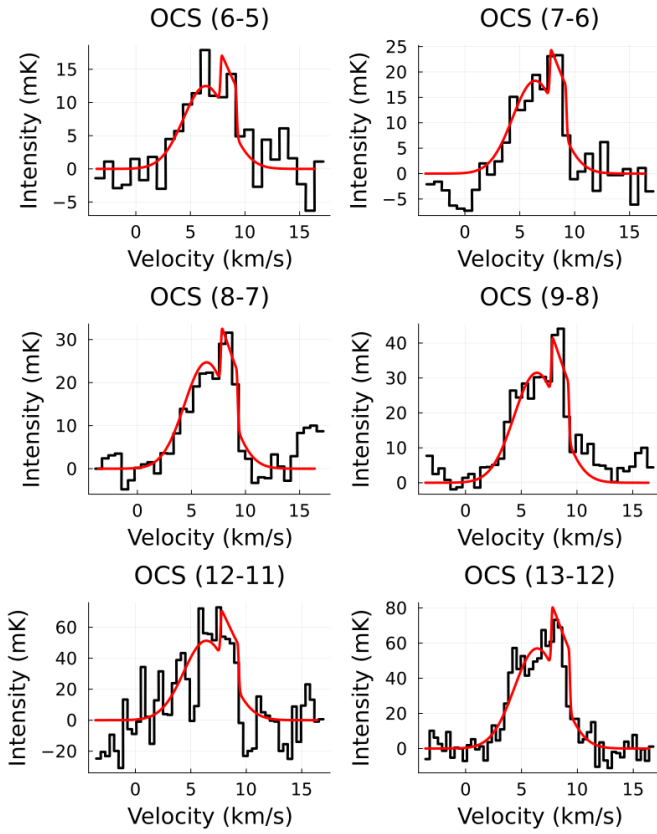


Fig. 6: Detected OCS transition lines in black with the two-component LTE fit in red. The component at 9 km s^{-1} is optically thick, which creates a sort of plateau.

where rms_i is the noise at the channel frequency and $cal = 0.1$, the estimated calibration error of our observations (10%). We define confidence intervals by calculating parameter ranges, where χ^2 is less than 1.5 than the minimum value, to evaluate how constrained those parameters are. The excitation temperatures, column densities, kinetic temperatures, and H_2 densities are listed in columns 5 to 8 of Table 3.

3.2.5. Comparison between the LTE and non-LTE models

The excitation temperatures given by both methods are similar for CS and ^{13}CS . On the other hand, the LTE modeling of DCN, DNC and DCO^+ converges toward very low $T_{\text{ex}} \leq 5 \text{ K}$, while the non-LTE models are closer to 10 K. The kinetic temperature of the gas is not well constrained since we only have access to two different E_{up} values for most of the modeled species here. The uncertainties are also large for the H_2 density.

The column densities are mostly consistent between LTE and non-LTE models. They are very close to each other for C^{34}S , DCN, and HC_3N , with a difference of less than 20%, while the difference is less than a factor of 2 for CS, ^{13}CS , DCO^+ , and H_2CO . However, DNC and HN^{13}C differ by a factor 2 to 3, and HCN by a factor 4.5. Those discrepancies do not seem correlated to the difference in excitation temperature between LTE and non-LTE.

The non-LTE modeling of ^{13}CS results in a large kinetic temperature (42 K) but an H_2 density of only a few 10^4 cm^{-3} . A temperature of 42 K is consistent with the inner envelope or a disk, while densities of 10^4 cm^{-3} are typical of outer envelopes

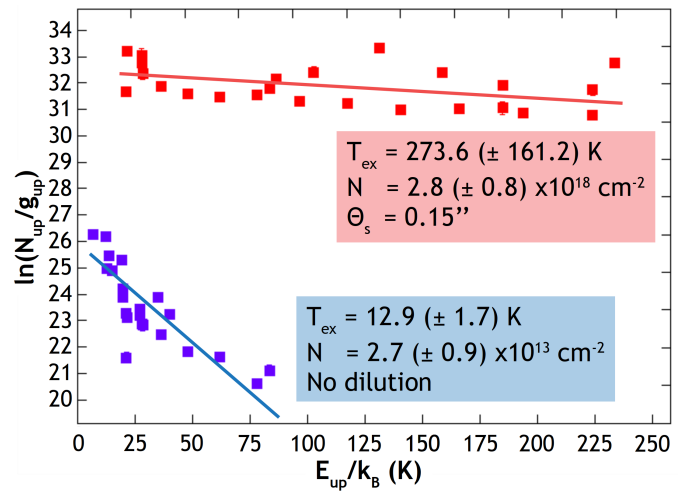


Fig. 7: Rotational diagram for CH_3OH . Blue points represent components peaking at the system velocity $v_{\text{Lsr}} = 6.4 \text{ km s}^{-1}$, for which we assume no beam dilution. Red points represent components peaking at 8.5 km s^{-1} for which we assume a $0.15''$ emission region. The blue and red lines represent the linear regressions on those points.

at $T \lesssim 10 \text{ K}$. In addition, for CS and C^{34}S , we find kinetic temperatures and excitation temperatures, both in LTE and non-LTE, close to 10 K. Those are indications that the $T_{\text{kin}} = 42 \text{ K}$ value for ^{13}CS needs to be taken with caution. However, the excitation temperature and column density match the LTE modeling with only a $\sim 30\%$ difference.

3.2.6. Upper limits

Here, we provide upper limits on the column densities of several non-detected isotopologues. For each species, we calculated the maximum line flux of all transitions covered by our spectral survey:

$$F_{\text{max}} = 3rms \sqrt{2dv \times FWHM}, \quad (11)$$

where rms is the noise level at the current frequency, dv is the channel width in km s^{-1} (200 kHz in frequency space), and $FWHM$ is the line width in km s^{-1} . The corresponding column densities are calculated based on F_{max} assuming LTE with the same excitation temperature, $FWHM$, and source size as the main isotopologue. The upper limit is taken as the lowest value among all transitions. The results are reported in Table 4 with the superscript ^a. Those upper limits range from 4.5×10^{10} to $1.7 \times 10^{12} \text{ cm}^{-2}$. ^{13}CCH and $\text{c-C}_3\text{D}_2$ are more than a hundred times less abundant than their main isotopologue. The upper limits on $\text{l-C}_3\text{HD}$ and $\text{l-C}_3\text{D}_2$ are only three times lower than the column density of $\text{l-C}_3\text{H}_2$, while the upper limits for HDCS and D_2CS are ten times lower compared to H_2CS .

We also calculated the upper limits of several species detected in other Class I protostars (see Sect. 4.4), listed with the superscript ^b in Table 4. We employed the same method and assumed no beam dilution and a $FWHM$ of 1 km s^{-1} . We ran the calculations for excitation temperatures of 10, 20, and 30 K and took the largest of the three upper limits. Apart from C_6H , which shows an upper limit of $2.0 \times 10^{12} \text{ cm}^{-2}$, all the other species have column densities lower than 10^{12} cm^{-2} .

Table 3: Best-fit parameters for each species, with both LTE and non-LTE modeling when possible. The number in parenthesis indicate the uncertainties. Bracketed values for the non-LTE T_{ex} indicate the range of excitation temperatures for the lines of the species.

Species	T_{ex} (K) (LTE)	N (cm $^{-2}$) (LTE)	$\Theta_s(\text{''})$ (LTE)	T_{ex} (K) (non-LTE)	N (cm $^{-2}$) (non-LTE)	T_{kin} (K) (non-LTE)	n(H $_2$) (cm $^{-3}$) (non-LTE)
CCH ^{b,g}	8.9	$3.6(0.2) \times 10^{14}$	> 100	-	-	-	-
CCD ^{e,g}	8.9 (0.7)	$9.4(0.3) \times 10^{12}$	-	-	-	-	-
C ^{13}CH ^{b,g}	8.9	$4.0(0.3) \times 10^{12}$	-	-	-	-	-
CCS ^e	12.1 (1.1)	$2.8(1.0) \times 10^{12}$	39.2 (18.1)	-	-	-	-
C $_3\text{H}$ ^e	9.0 (0.7)	$3.5(0.5) \times 10^{11}$	> 100	-	-	-	-
c-C $_3\text{H}_2$ ^e	10.4 (0.3)	$1.3(0.1) \times 10^{13}$	64.0 (16.8)	-	-	-	-
c-C $_3\text{HD}$ ^e	9.8 (0.8)	$9.3(1.4) \times 10^{11}$	52.2 (22.9)	-	-	-	-
c-CC $^{13}\text{CH}_2$ ^e	7.8 (2.7)	$3.6(0.5) \times 10^{11}$	> 100	-	-	-	-
l-C $_3\text{H}_2$ ^e	16.2 (3.7)	$1.7(0.2) \times 10^{11}$	> 100	-	-	-	-
C $_3\text{N}$ ^e	16.4 (1.7)	$2.3(0.3) \times 10^{11}$	> 100	-	-	-	-
C $_3\text{O}$ ^e	22.9 (14.8)	$1.2(0.2) \times 10^{11}$	> 100	-	-	-	-
C $_3\text{S}$	29.9 (9.6)	$2.0(0.3) \times 10^{11}$	> 100	-	-	-	-
C $_4\text{H}$ ^e	16.7 (1.0)	$4.3(0.7) \times 10^{12}$	> 100	-	-	-	-
l-C $_4\text{H}_2$ ^e	23.0 (6.7)	$2.6(1.6) \times 10^{11}$	> 100	-	-	-	-
CH $_3\text{CCH}$ ^e	21.8 (0.8)	$1.8(0.0) \times 10^{13}$	> 100	-	-	-	-
CH $_2\text{DCC}$	12.4 (6.3)	$3.3(0.8) \times 10^{12}$	> 100	-	-	-	-
CH $_3\text{CHO}$ ^{a,e}	8.3 (0.6)	$2.3(0.4) \times 10^{12}$	> 100	-	-	-	-
CH $_3\text{CN}$	28.3 (5.0)	$2.1(0.3) \times 10^{11}$	> 100	-	-	-	-
CH $_3\text{OH}$ (c.1) ^d	12.9 (1.7)	$2.7(0.9) \times 10^{13}$	> 100	-	-	-	-
CH $_3\text{OH}$ (c.2) ^d	273.6 (161.2)	$2.8(0.8) \times 10^{18}$	0.15	-	-	-	-
CS ^e	9.0 (2.2)	$1.2(0.2) \times 10^{13}$	> 100	[10.2 – 12.5]	$1.5(0.1) \times 10^{13}$	14.0 (3.7)	$6.7(93) \times 10^5$
^{13}CS ^{a,e}	4.9 (0.6)	$7.3(1.5) \times 10^{11}$	> 100	[4.8 – 5.5]	$5.0(0.1) \times 10^{11}$	42.0 (7.4)	$4.0(0.1) \times 10^4$
C ^{33}S ^{a,b}	9.0	$2.1(0.2) \times 10^{11}$	> 100	-	-	-	-
C ^{34}S	11.3 (2.7)	$1.4(0.1) \times 10^{12}$	> 100	13.0	$1.2(0.1) \times 10^{12}$	13.0 (10.8)	$1.0(1.0) \times 10^8$
HCN ^b	5.0	$3.0(0.7) \times 10^{13}$	> 100	10.0	$6.8(2.3) \times 10^{12}$	11.0	2.0×10^6
DCN ^{a,e}	5.0 (0.3)	$1.3(0.1) \times 10^{12}$	> 100	[6.1 – 12.3]	$1.1(0.3) \times 10^{12}$	11.0 (4.9)	$2.0(3.4) \times 10^6$
H ^{13}CN ^{a,b}	5.0	$6.1(0.3) \times 10^{11}$	> 100	-	-	-	-
HC ^{15}N ^{a,b}	5.0	$1.9(0.2) \times 10^{11}$	> 100	-	-	-	-
HNC ^b	- ^f	-	8.7	$1.2(0.1) \times 10^{13}$	9.0	1.2×10^6	
DNC	3.9 (0.3)	$5.2(2.4) \times 10^{12}$	> 100	[7.2 – 9.4]	$1.4(0.4) \times 10^{12}$	9.0 (4.7)	$1.2(8.8) \times 10^6$
HN ^{13}C ^b	3.9	$1.3(0.1) \times 10^{12}$	> 100	9.2	$5.6(0.5) \times 10^{11}$	9.0	1.2×10^6
H ^{15}NC ^{a,b}	3.9	$2.4(0.2) \times 10^{11}$	> 100	-	-	-	-
HNCO ^e	16.9 (1.8)	$1.1(0.2) \times 10^{12}$	> 100	-	-	-	-
DCO $^+$	5.7 (0.7)	$3.0(0.7) \times 10^{12}$	> 100	[9.1 – 10.9]	$2.0(0.1) \times 10^{12}$	10 ^c (2.4)	$1.4(98) \times 10^6$
H $^{13}\text{CO}^+$ ^b	5.7	$4.1(0.7) \times 10^{12}$	> 100	-	-	-	-
HC $^{18}\text{O}^+$ ^b	5.7	$2.7(0.2) \times 10^{11}$	> 100	-	-	-	-
HC $_3\text{N}$ ^e	21.4 (1.1)	$3.5(0.2) \times 10^{12}$	> 100	21.0	$3.6(0.5) \times 10^{12}$	21.0 (4.0)	$6.7(6.6) \times 10^7$
DC $_3\text{N}$ ^e	25.5 (6.3)	$1.2(0.1) \times 10^{11}$	> 100	-	-	-	-
H $^{13}\text{CCCN}$ ^e	12.6 (3.7)	$1.1(0.5) \times 10^{11}$	> 100	-	-	-	-
HC ^{13}CCN	15.4 (6.6)	$6.2(3.6) \times 10^{10}$	> 100	-	-	-	-
HCC ^{13}CN ^e	20.3 (5.3)	$7.2(1.4) \times 10^{10}$	> 100	-	-	-	-
HC $_5\text{N}$ ^e	34.0 (2.7)	$5.2(0.6) \times 10^{11}$	> 100	-	-	-	-
H $_2\text{CO}$ ^e	18.4 (4.8)	$2.2(0.5) \times 10^{13}$	> 100	[7.9 – 11.6]	$2.6(0.7) \times 10^{12}$	10.0 ^c (4.1)	$6.7(93) \times 10^5$
D $_2\text{CO}$ ^b	18.4	$2.7(0.2) \times 10^{12}$	> 100	-	-	-	-
H $_2^{13}\text{CO}$ ^e	35.7 (17.0)	$1.1(0.5) \times 10^{12}$	> 100	-	-	-	-
H $_2\text{CCO}$ ^e	16.0 (1.5)	$2.2(0.1) \times 10^{12}$	> 100	-	-	-	-
H $_2\text{CS}$ ^e	16.2 (1.2)	$2.4(0.1) \times 10^{12}$	> 100	-	-	-	-

3.3. Isotopic fractionation

probability that a D atom replaces a H atom in equivalent sites

The calculation of column densities allows us to determine the isotopic fractionation ratios of several molecules, for the isotopes D, ^{13}C , ^{17}O , ^{18}O , ^{15}N , ^{33}S , and ^{34}S . The results are listed in Table 5. The statistically corrected ratios, that account for the

Table 3 continued

Species	T_{ex} (K) (LTE)	N (cm^{-2}) (LTE)	$\Theta_s(\text{''})$ (LTE)	T_{ex} (K) (non-LTE)	N (cm^{-2}) (non-LTE)	T_{kin} (K) (non-LTE)	n(H_2) (cm^{-3}) (non-LTE)
HNCO	16.6 (1.3)	$1.1(0.1) \times 10^{12}$	> 100	-	-	-	-
HOCO ⁺	5.9 (1.8)	$2.2(1.1) \times 10^{11}$	> 100	-	-	-	-
$\text{N}_2\text{D}^+{}^a$	3.7 (0.0)	$1.2(0.0) \times 10^{12}$	> 100	-	-	-	-
SO ^e	49.4 (14.9)	$2.3(0.5) \times 10^{13}$	> 100	-	-	-	-
³⁴ SO	32.3 (22)	$9.4(2.9) \times 10^{11}$	33.1(33.3)	-	-	-	-
SO ₂ ^e	39.2 (7.1)	$7.3(4.2) \times 10^{12}$	17.3(7.8)	-	-	-	-

Notes. ^a The partition functions of those species have been extrapolated below 9.375 K. ^b The column densities of those species have been calculated using the excitation temperature of their isotopologue. ^c Minimum kinetic temperature below which collision coefficients are not available. ^d See Sect. 3.2.3. ^e Species for which a rotational diagram has been fitted (see Sect. 3.2.1). The following is the list of references for collision coefficients; CS: Denis-Alpizar et al. (2013), ¹³CS and ³⁴S: Lique et al. (2006), HCN: Goicoechea et al. (2022), DCN: Magalhães et al. (2018), HNC and DNC: Hernández Vera et al. (2017), HN¹³C: Dumouchel et al. (2010), DCO⁺: Flower (1999), HC₃N: Faure et al. (2016), H₂CO: Wiesenfeld & Faure (2013). ^f We could not find a good fit of HNC in LTE, so we did not include it in the Table. ^g We do not report our non-LTE results for CCH, CCD, and C¹³CH due to very poor constraints with the fitting method.

Table 4: Upper limit on column densities for undetected isotopologues.

Species	Column density (cm^{-2})
¹³ CCH ^a	$\leq 1.7 \times 10^{12}$
c-C ₃ D ₂ ^a	$\leq 1.1 \times 10^{11}$
l-C ₃ HD ^a	$\leq 5.6 \times 10^{10}$
l-C ₃ D ₂ ^a	$\leq 4.5 \times 10^{10}$
CH ₃ CCD ^a	$\leq 1.4 \times 10^{12}$
H ₂ C ¹⁸ O ^a	$\leq 3.4 \times 10^{11}$
HDCS ^a	$\leq 2.3 \times 10^{11}$
D ₂ CS ^a	$\leq 3.2 \times 10^{11}$
C ₂ H ₃ CN ^b	$\leq 2.8 \times 10^{11}$
C ₅ H ^b	$\leq 6.8 \times 10^{11}$
C ₆ H ^b	$\leq 2.0 \times 10^{12}$
HNCCC ^b	$\leq 8.9 \times 10^{10}$
HCCNC ^b	$\leq 3.1 \times 10^{11}$
HCCCHO ^b	$\leq 6.0 \times 10^{11}$
H ₂ CCN ^b	$\leq 1.1 \times 10^{11}$
HCNO ^b	$\leq 5.0 \times 10^{10}$
HSCN ^b	$\leq 1.3 \times 10^{11}$
NH ₂ CHO ^b	$\leq 3.8 \times 10^{11}$

Notes. ^a We assumed the same excitation temperature, FWHM and beam dilution than the main isotopologue in our LTE models (see Table 3). ^b We assumed no beam dilution, a FWHM of 1 km s⁻¹, and excitation temperatures of 10, 20, and 30 K. The displayed upper limit is the largest among the three.

in the molecule are calculated as:

$$\frac{XD}{XH} = \frac{XHD}{XH_2} = \frac{1}{2} \frac{N(XHD)}{N(XH_2)}, \quad (12)$$

$$\frac{XD}{XH} = \frac{XH_2D}{XH_3} = \frac{1}{3} \frac{N(XH_2D)}{N(XH_3)}, \quad (13)$$

$$\frac{XD}{XH} = \frac{XD_2}{XH_2} = \sqrt{\frac{N(XHD)}{N(XH_2)}}, \quad (14)$$

where $N(X)$ is the column density of molecule X. Similarly to the deuterium ratios, we have divided the c-C₃H₂/c-HCC¹³CH column density ratio by 2 to account for the statistical weight of the substituted atom. We also added upper and lower limits based on the estimates of Table 4.

The ¹²C/¹³C ratios lie between ~16 and ~60, except for CCH, which exhibits high column density ratios with both isotopologues: C¹³CH (90) and ¹³CCH (≥ 211) in LTE. The ¹³CCH/C¹³CH ratio is comparable to previous measurements in TMC1 and L1527 and is well explained by the H + ¹³CCH → H + C¹³CH reaction, which favors C¹³CH (Loison et al. 2020). Comparing with the ISM standard value of ~68 (Milam et al. 2005), we can infer that the lines of the main isotopologues of CS, HCN, HNC, and H₂CO are most likely optically thick; we consider the ratios involving those species as upper or lower limits. For HC₃N, there seems to be a slight enrichment in ¹³C, contrary to previous measurements in dense clouds (Table 1 of Loison et al. 2020). This apparent enrichment may be due to the ¹³C + HC₃N reaction (Loison et al. 2020) or (more likely) to a slightly optically thick emission of the main isotopologue.

For the mono-deuterated molecules, the deuterium fractionation ratios vary from 2% to 6% using the LTE column densities. Those values are higher than the cosmic D/H ratio of $\sim 1.4 \times 10^{-5}$ (Linsky 2003), but consistent with other protostellar environments (Ceccarelli et al. 2014; Riaz & Thi 2022; Giers et al. 2023). In Table 5, we also display several ratios of a secondary isotopologue with respect to the ¹³C isotopologue, for example, DCN/¹³CN that we renormalize by the standard factor of ¹²C/¹³C=68. This allows us to estimate the deuterium fractionation ratio of HCN, HNC, and HCO⁺. The DCN/(H¹³CN × 68) and DNC/(HN¹³C × 68) are about 3.1% and 5.8%, respectively, which are lower than the upper limits derived with the main isotopologues (<4.3% and <16%, respectively). The DCO⁺/ (H¹³CO⁺ × 68) is found to be ~1.1%. For the doubly deuterated molecules, we only provide upper limits on the statistically corrected ratios, due to their non-detection or the optical thickness of the lines of the main isotopologue. The lowest of those upper limits is ~9% for c-C₃D₂/c-C₃H₂, while the upper limits for l-C₃D₂/l-C₃H₂, D₂CO/H₂CO, and D₂CS/H₂CS stand above 35%.

We detect two species bearing the ¹⁵N isotope, HC¹⁵N, and H¹⁵NC. The direct ratio of HCN/HC¹⁵N only gives a lower limit of > 158 , since the HCN emission is optically thick. Using the ¹³C isotopologue, we find a ¹⁴N/¹⁵N ratio of 217.0 ± 54.4 for HCN and 367.2 ± 50.8 for HNC. Those values are in the range of what is found in other protostars using indirect measurements with H¹³CN and HN¹³C (~160–370 for HCN and ~240–460 for HNC, Wampfler et al. 2014; Yoshida et al. 2019) as well as a direct measurement for HCN in the Class 0 protostar L483

(321 ± 96 , Agúndez et al. 2019). However, indirect measurements using the ^{13}C isotopologues could lead to erroneous results if the $^{12}\text{C}/^{13}\text{C}$ differs from 68, as shown by observations toward molecular clouds and prestellar cores (e.g., Ikeda et al. 2002; Magalhães et al. 2018; Jensen et al. 2024) and theoretical studies (e.g., Roueff et al. 2015; Loison et al. 2020; Colzi et al. 2020). The actual HCN/ HC^{15}N and HNC/ H^{15}NC ratios in L1551 IRS 5 may therefore be different from the values we obtain through their ^{13}C isotopologues. Despite the many uncertainties surrounding measurements of the $^{14}\text{N}/^{15}\text{N}$ ratio in HCN and HNC, it seems that these measurements tend to give a $^{14}\text{N}/^{15}\text{N}$ ratio notably smaller than the solar value of 441.

$\text{H}_2\text{C}^{18}\text{O}$ and HC^{18}O^+ are the only two ^{18}O -bearing species that we detected. The local measurements of $\text{H}_2\text{CO}/\text{H}_2\text{C}^{18}\text{O}$ ratios typically gives values of $\gtrsim 500$ (e.g., Lucas & Liszt 1998; Wilson 1999). However, we only derived a very low lower limit of 65 for this ratio, due to the probably optically thick emission of H_2CO and the non-detection of $\text{H}_2\text{C}^{18}\text{O}$. We also obtain an $(\text{H}^{13}\text{CO}^+ \times 68)/\text{HC}^{18}\text{O}^+$ ratio of 1033 ± 190 , which is 50% higher than what is measured in diffuse molecular clouds for $\text{HCO}^+/\text{HC}^{18}\text{O}^+$ (672 ± 110 , Lucas & Liszt 1998) and in the protostar L1527 based on H^{13}CO^+ (Yoshida et al. 2019).

Yan et al. (2023) measured the sulfur isotopologue ratios in the Milky Way, and find $^{32}\text{S}/^{34}\text{S} \sim 15 - 25$, $^{32}\text{S}/^{33}\text{S} \sim 50 - 100$, and $^{34}\text{S}/^{33}\text{S} \sim 3 - 6$. We find consistent values here for L1551 IRS 5, in agreement with Esplugues et al. (2023) for the Class 0 protostar B335. The ratios are however on the lower end of the intervals for CS, which supports the idea of an optically thick CS emission.

4. Discussion

4.1. Comparison with previous studies of L1551 IRS 5

In this section, we compare the estimated physical parameters with what has been found by other observations of the same source. Roberts et al. (2002) observed a similar frequency range, focusing on HCN, H_2CO , and their isotopologues between ~ 72 GHz and ~ 150 GHz³. The observations were done with the NRAO 12m radio telescope, resulting in a beam twice larger than ours ($40''$ - $88''$ or ~ 5750 - 13000 au). They derived column densities in LTE assuming several excitation temperatures from 5 K to 40 K, except for HCN and DCN; in those cases, they found excitation temperatures of 5 K and 6 K, respectively, in accordance with our values. The column densities for DCN, H^{13}CN , and H_2^{13}CO only have a 20% difference with ours, sign of an extended emission from those species. We however find lower column densities on H_2CO (by a factor of 2) and HCN (by a factor of 3). This may be a bias due to the optical thickness of the detected lines, that Roberts et al. (2002) derive to be 2.4 for H_2CO and 16.9 for HCN. Our upper limit of 4.3% for the DCN/HCN ratio (in LTE) is therefore higher than their 1.9% estimate.

Jørgensen et al. (2004) performed observations in the 3mm, 2mm, and 1mm bands using the 15m James Clerk Maxwell Telescope and the Onsala 20m telescope. Comparing the integrated fluxes of the lines detected in both surveys, we obtained similar values for SO (2.3–1.2), with a 15% higher value in our case, and for CN (1–0), for which we have $\leq 30\%$ larger fluxes on each hyperfine component. We found a flux of $\approx 0.33 \pm 0.02$ K km s⁻¹ on the H^{13}CN (1 – 0) line when integrating the three hyperfine components, whereas they estimated an upper limit of

³ They also observed the (4,0,4–3,0,3) transition of HDCO at 256.585 GHz.

Table 5: Statistical isotopic fractionation ratios for molecules whose column density has been estimated, for the LTE and non-LTE cases.

Species	LTE ratio	non-LTE ratio
D / H		
CCD / CCH	0.026 ± 0.002	–
c-C ₃ HD / c-C ₃ H ₂	0.036 ± 0.006	–
c-C ₃ D ₂ / c-C ₃ H ₂ ^a	≤ 0.09	–
l-C ₃ HD / l-C ₃ H ₂ ^a	≤ 0.33	–
l-C ₃ D ₂ / l-C ₃ H ₂ ^a	≤ 0.51	–
CH ₂ DCCH / CH ₃ CCH	0.061 ± 0.015	–
CH ₃ CCD / CH ₃ CCH ^a	≤ 0.078	–
DCN / HCN	< 0.043	< 0.162
DCN / (H ¹³ CN $\times 68$)	0.031 ± 0.003	–
DNC / HNC	–	< 0.117
DNC / (H ¹³ C $\times 68$)	0.058 ± 0.028	0.037 ± 0.011
DC ₃ N / HC ₃ N	0.034 ± 0.003	–
D ₂ CO / H ₂ CO	< 0.35	–
HDCS / H ₂ CS ^a	≤ 0.095	–
D ₂ CS / H ₂ CS ^a	≤ 0.36	–
DCO ⁺ / (H ¹³ CO ⁺ $\times 68$)	0.011 ± 0.003	–
$^{12}\text{C} / ^{13}\text{C}$		
CCH / C ¹³ CH	90 ± 8.4	–
CCH / ¹³ CCH ^a	≥ 211	–
c-C ₃ H ₂ / c-HCC ¹³ CH	72.2 ± 10.4	–
CS / ¹³ CS	> 16.4	> 10.0
HCN / H ¹³ CN	> 49.2	–
HNC / HN ¹³ C	–	> 21.4
HC ₃ N / H ¹³ CCCN	31.8 ± 14.6	–
HC ₃ N / HC ¹³ CCN	56.5 ± 32.9	–
HC ₃ N / HCC ¹³ CN	48.6 ± 9.9	–
H ₂ CO / H ₂ ¹³ CO	> 20.0	–
$^{14}\text{N} / ^{15}\text{N}$		
HCN / HC ¹⁵ N	> 157.9	–
(H ¹³ CN $\times 68$) / HC ¹⁵ N	217.0 ± 54.4	–
(HN ¹³ C $\times 68$) / H ¹⁵ NC	367.2 ± 50.8	–
$^{16}\text{O} / ^{18}\text{O}$		
H ₂ CO / H ₂ C ¹⁸ O ^a	≥ 65	–
(H ¹³ CO ⁺ $\times 68$) / HC ¹⁸ O ⁺	1033 ± 190	–
$^{32}\text{S} / ^{34}\text{S}, ^{32}\text{S} / ^{33}\text{S}$		
CS / C ³⁴ S	> 8.6	> 12.5
CS / C ³³ S	> 57.1	–
C ³⁴ S / C ³³ S	6.7 ± 0.8	–
SO / ³⁴ SO	24.5 ± 9.2	–

Notes. ^a We provide upper and lower limits for non-detected species (see Table 4).

0.12 K km s⁻¹. Conversely, they measured a flux that is twice as high for N_2H^+ (1 – 0) despite their larger beam. This is probably a consequence of a strong large-scale N_2H^+ emission, as observed by Tatematsu et al. (2004).

Mercimek et al. (2022) surveyed the frequency range 214.5–238.0 GHz with the IRAM-30m telescope. They therefore probed the source with a smaller beam (11'' or ~ 1500 au). They derive excitation temperatures and column densities using a rotational diagram analysis. We estimated higher column densities for DCN (3 times higher), N_2D^+ (10 times in LTE, 4 times in non-LTE), ¹³CS (3 times in LTE, 2 times in non-LTE), and DCO⁺ (9 times). Those species with excitation temperatures < 10 K are usually associated with the colder envelope. How-

ever, Mercimek et al. (2022) assumed a 20–35 K rotational temperature in their analysis. The differences may therefore be due to the excitation temperature used to derive the column density, or to a decreasing column density of those species in the inner regions. We also find lower excitation temperatures than the 20–35 K assumed in their analysis for CCD (8.9 K in our case), CCS (12.1 K) and c-C₃H₂ (24.4 K in Mercimek et al. 2022, 10.4 K in our case), but our column densities are similar within 20% for those three species. There are also a few species for which our estimated column density is much lower than Mercimek et al. (2022), namely H₂CCO (10 times lower), CH₃CN (5 times), CH₃CCH (3 times), OCS (2 times), and CH₃CHO (7 times). Except for CH₃CHO, those species have excitation temperatures > 15 K, which suggests that their emission region is not as extended (and therefore not as cold) as species with $T_{\text{ex}} < 10$ K, resulting in different dilution factors (η in Equations (3) and (8)). We however find excitation temperatures and column densities in agreement within 10% for SO, SO₂, and o-D₂CO, despite their excitation temperatures of $\gtrsim 20$ K.

4.2. Isotopic ratios

Excluding the upper limits, most deuterium fractionation ratios range from 1 to 6%, and are consistent with values found in other Class 0/I sources; namely DC₃N/HC₃N (Agúndez et al. 2019; Bianchi et al. 2019), c-C₃HD/c-C₃H₂ (Agúndez et al. 2019; Giers et al. 2022), HDCS/H₂CS (Agúndez et al. 2019) as well as DNC/HNC, DCO⁺/H¹³CO⁺, DCN/H¹³CN, and DNC/HN¹³C (Riaz & Thi 2022). These values are higher than the HDO/H₂O ratio of $\sim 0.1\%$ found by Andreu et al. (2023) in L1551 IRS 5, but this difference between water and organic species is observed in other sources (Parise et al. 2005; Coutens et al. 2012; Jørgensen et al. 2018). Our D₂CO/H₂CO upper limit (<35%) is lower than the high ratio found by Mercimek et al. (2022) in L1551 IRS 5 (45–84%), which is likely due to the optical thickness of the H₂CO lines. Our upper limit of <9.5% for the HDCS/H₂CS ratio is consistent with their estimate of 9% to 14%.

The highest (non-upper limit) ratio is CH₂DCCH/CH₃CCH with 6.1%, which is almost twice the level of deuteration of the other species in our study. This is also consistent with other measurements, as Markwick et al. (2002) found a ratio of $\geq 10\%$ in TMC-1 with the Onsala 20m telescope, while Agúndez et al. (2019) measured 6.5% in L483 with the IRAM-30m. Our upper limit of 7.8% on the CH₃CCD/CH₃CCH ratio is also high, while Agúndez et al. (2019) measured a 5.9% ratio, close to their CH₂DCCH/CH₃CCH ratio of 6.5%. The proximity of both ratios is also supported by chemical models (Agúndez et al. 2021). We could therefore expect a CH₃CCD/CH₃CCH also close to 6%. CH₃CCH is a relatively complex molecule with seven atoms. ALMA observations of IRAS 16293–2422 show that the deuteration of the largest COMs is higher by a factor of about 2–4 than the simplest COMs (Jørgensen et al. 2018). A similar trend is seen in our data between the simplest species and CH₃CCH. Jørgensen et al. (2018) suggested that for the COMs, it could be due to different timescales with the most complex ones forming at a later stage with denser and colder conditions. However, this explanation could be different in the case of the present study as CH₃CCH is predicted to form very early on by chemical models (e.g., Coutens et al. 2020) and it is also detected in various molecular clouds (Turner et al. 2000). D–H exchanges could potentially occur at later stages and increases the D/H ratio of CH₃CCH. Conversely, DCO⁺ seems to display a much lower deuteration ratio of $\sim 1\%$, reflecting its formation in the diffuse ISM.

We found a high CCH/C¹³CH ratio of 90 with the LTE models, at the same level as in the prestellar core L1544 and the Class 0 protostars HH211 and L483 (Agúndez et al. 2019; Giers et al. 2023). This may indicate that this ratio experiences little variation during the evolution of a protostar, at least in the envelope. Similarly, an even higher CCH/¹³CCH ratio is found in those sources (> 150), which may be consistent with our lower limit of 211. However, single-dish observations of L1527 by Yoshida et al. (2019) and TMC1 by Sakai et al. (2010) show ratios almost twice larger for both isotopologues, which suggests that the carbon fractionation in CCH may be sensitive to the environment in which it occurs.

The three HC₃N isotopologues containing single ¹³C substitutions show similar fractionation ratios. However, their relative abundances H¹³CCCN : HC¹³CCN : HCC¹³CN of $\sim 1:0.6 \pm 0.4:0.7 \pm 0.3$ are quite different from other protostellar sources, which display a 1:1:x ratio, with $x \approx 1.2\text{--}2.1$ (see Agúndez et al. 2019, and references therein). Despite relatively large error bars on our measurements, HCC¹³CN does not seem to be more abundant than the two others in L1551 IRS 5.

4.3. Abundance ratios as evolutionary tracers

Abundance ratios are often proposed as evolution tracers in protostellar environments. Agúndez et al. (2019) and Esplugues et al. (2023) propose that the SO₂/CCS and SO/CS abundance ratios should increase with the evolutionary stage (from starless core to Class I). They find overall increasing ratios going from the starless core TMC1, then to the prestellar core L1544, to the Class 0 protostars B335, L483, and B1-b. As a Class I protostar, L1551 IRS 5 represents the next evolutionary stage, and we plot those ratios alongside our measurements in Fig. 8. Our points lie in the same ranges as the Class 0 sources and so is the SO₂/CCS ratio for the Class I protostar L1455 IRS 1. These results need to be taken with caution, as we measure very different excitation temperatures for the two species in each ratio (39.2 K and 12.1 K for SO₂ and CCS respectively, and 49.4 K and 9.0 K for SO and CS), indicating that their emission originates from different regions. That is not apparent in Agúndez et al. (2019) that assume a ~ 10 K rotational temperature for deriving the column densities, while Esplugues et al. (2023) assume a kinetic temperature of 15 K for their non-LTE calculations. Assuming a 10 K excitation temperature for those species results in a SO/CS ratio that is three times greater and a SO₂/CCS ratio three times lower, which does not change the trend. We therefore conclude that the increasing trends may be good indicators of evolutionary stages, but only in the early phases of the star formation process.

4.4. Comparison with other Class I protostars

Here, we compare the chemical composition of L1551 IRS 5 with other Class I protostars for which large spectral surveys with the IRAM-30m telescope are available. L1527 and SVS 13A have been observed as part of the ASAI large program (Lefloch et al. 2018). The survey spans several frequency ranges from 85 GHz to 272 GHz with a spectral resolution of 200 kHz, and achieves a rms of 2 to 7 mK. L1489 IRS, B5 IRS 1 and L1455 IRS 1 were observed by Mercimek et al. (2022) at 2mm, also with a spectral resolution of 200 kHz and a rms of 10 mK. The distance and luminosity of each source is listed in Table 6, alongside L1551 IRS 5. Except for SVS 13A (another an eruptive young star), those sources are dimmer than the 22 L_⊙ of L1551 IRS 5 (Froebrich 2005). We do not include the sources

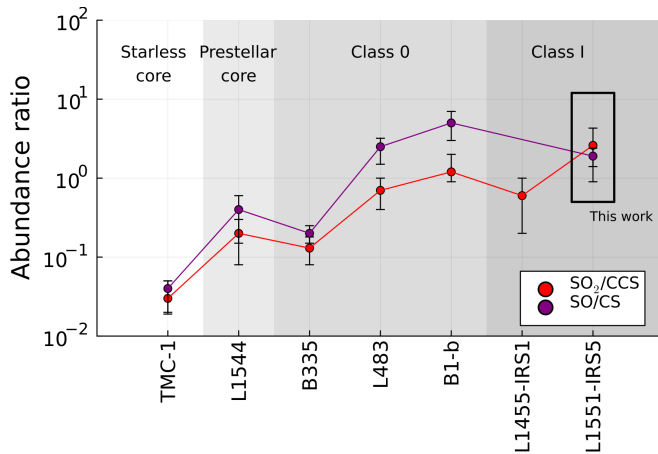


Fig. 8: Abundance ratios of SO_2/CCS (red) and SO/CS (purple) in several sources and in L1551 IRS 5. The ratios for TMC-1, L1544, L483 and B1-b are taken from Agúndez et al. (2019), B335 from Esplugaes et al. (2023), and the value for L1455 IRS 1 is taken from Mercimek et al. (2022).

surveyed by Le Gal et al. (2020) because they only reported the molecules with ≤ 3 atoms so far.

Table 7 lists the species detected in each source. Comparing the detections (\mathbf{Y}) with non-detections (\mathbf{N}), L1527 and L1551 IRS 5 show the largest numbers of species. Particularly, L1527 is known for its rich carbon-chain chemistry (Sakai et al. 2008). Comparatively, we do not detect several species in L1551 IRS 5 that are present in L1527; namely $\text{C}_2\text{H}_3\text{CN}$, C_5H , C_6H , HCCCHO, HCCNC, H_2CCN , HNCCC, HCNO, and HSCN. We provide upper limits on the column densities of those species in Table 4. Yoshida et al. (2019) performed a survey towards L1527 with the Nobeyama 45m telescope at 3mm and calculated a column density for C_5H of $(5.3 \pm 1.1) \times 10^{11} \text{ cm}^{-2}$, which is about 400 times less abundant than C_4H . A similar ratio in L1551 IRS 5 would yield a C_5H column density of $\sim 10^{10} \text{ cm}^{-2}$, which is consistent with the upper limit of $6.8 \times 10^{11} \text{ cm}^{-2}$ we derived. In the same manner, Araki et al. (2017) determined a $\text{C}_4\text{H}/\text{C}_6\text{H}$ abundance ratio of 153 in L1527. This would mean for L1551 IRS 5 a C_6H column density of $2.8 \times 10^{10} \text{ cm}^{-2}$, which is lower than the upper limit of $2.0 \times 10^{12} \text{ cm}^{-2}$. Marcelino et al. (2010) calculated column densities for HCNO and its isomers in several protostellar sources including L1527. They found HCNO/HNCO ratios of 40 in L1527 and ranging from ~ 20 to ~ 80 in the other sources. Similar ratios in L1551 IRS 5 result in an HCNO column density between 1.4 and $5.5 \times 10^{10} \text{ cm}^{-2}$, also consistent with our upper limit of $5.0 \times 10^{10} \text{ cm}^{-2}$. HCCNC and HNCCC are both isomers of HC_3N . Their relative abundance have been measured in TMC-1 by Cernicharo et al. (2020), with ratios of 77 ± 8 for $\text{HC}_3\text{N}/\text{HCCNC}$, and 392 ± 22 for $\text{HC}_3\text{N}/\text{HNCCC}$. Applying those ratios to HC_3N , we find column densities of $4.5 \times 10^{10} \text{ cm}^{-2}$ for HCCNC and $8.9 \times 10^9 \text{ cm}^{-2}$ for HNCCC, both lower than the upper limits. In summary, C_5H , C_6H , HCCNC, HNCCC, and HCNO may still be present in L1551 IRS 5 with the same abundances relative to C_4H (for C_5H and C_6H) or their isomer as L1527, but the lower abundances of C_4H and the main isomers in L1551 IRS 5 make their detection more difficult.

Except HCCCHO, all O-bearing COMs detected in L1527 are also present in L1551 IRS 5 as well as in SVS 13A. On the other hand, a fewer number of COMs are detected in the three

Table 6: Properties of the selected sources from the ASAI program (Lefloch et al. 2018) and from Mercimek et al. (2022).

Source	Lum. (L_\odot)	Dist. (pc)	Location
L1551 IRS 5	22	141	Taurus
L1527	2.75	141	Taurus
L1489 IRS	3.5	141	Taurus
SVS 13A	34	260	Perseus
B5 IRS 1	5.0	294	Perseus
L1455 IRS 1	3.6	294	Perseus

sources L1489 IRS, B5 IRS 1, and L1455 IRS 1 by the survey of Mercimek et al. (2022). Notably, CH_3CHO and CH_3OCHO are missing despite being detected in L1551 IRS 5 within the same study. Those three sources and SVS 13A also show a lower number of hydrocarbons than L1527 and L1551 IRS 5, with the lack of detection of $\text{c-C}_3\text{H}$, $\text{l-C}_3\text{H}_2$, and $\text{l-C}_4\text{H}_2$. The survey of Mercimek et al. (2022) only covers transitions with $E_{\text{up}} > 50 \text{ K}$ for the last two species though. More generally, all species detected in L1489 IRS, B5 IRS 1, and L1455 IRS 1 are also detected in L1551 IRS 5, but not the opposite. H_2CCO and CH_3CN are not detected by the survey of Mercimek et al. (2022) in any of those three sources, while CCS, H_2S , HNCO, and OCS are only seen in L1455 IRS 1 (in addition to L1551 IRS 5). The most notable exception is SiO, that is detected in L1455 IRS 1 and SVS 13A, but not in L1527 and L1551 IRS 5 despite their closer distance. The lack of SiO may suggest the absence of shocks in those systems, although shocked gas have been reported in L1551 IRS 5 using other tracers (Yang et al. 2022). NH_2CHO is also a species detected in SVS 13 A but not seen in L1551 IRS 5.

4.5. Consequences of a luminosity outburst

As a FUor-like protostar, L1551 IRS 5 probably experienced a luminosity outburst that could have impacted the chemical history of its envelope. The starting date, duration, and intensity of this burst are however unconstrained, and its influence on the envelope composition unknown.

Visser et al. (2015) suggest that the line flux ratio $\text{H}^{13}\text{CO}^+ (1-0)/\text{N}_2\text{H}^+ (1-0)$ (integrated over the hyperfine components) is an outburst tracer, due to the desorption of CO from grain mantles that promotes the formation of HCO^+ and that is anti-correlated with N_2H^+ . A high ratio ($\gtrsim 1$) would therefore be indicative of a recent ($< 10^3$ years) outburst. Figure 9 displays this ratio for L1551 IRS 5, compared to other Class I protostars measured in the spectral survey of Le Gal et al. (2020). We find a rather low ratio, although in the same range of values as the other protostars, which are not known to experience outbursts. The results of this method to characterize the outburst are therefore inconclusive in our case. Using this principle, Hsieh et al. (2019) measured the location of the peak of N_2H^+ emission in Class 0/I sources using ALMA. They compare it with the theoretical CO snowline derived from the luminosity of the protostar to determine whether the source experienced a recent outburst. Similar observations of L1551 IRS 5 may be necessary to characterize its luminosity history.

5. Conclusion

We have performed a spectral survey at 3mm and 2mm of the Class I protostar L1551 IRS 5 with the IRAM-30m telescope. Our main results are as follows:

Table 7: List of detected species (only the main isotopologues) in Class I protostars with IRAM-30m surveys.

Species	L1527	SVS 13A	L1489 IRS	B5 IRS 1	L1455 IRS 1	L1551 IRS 5 ^a	L1551 IRS 5 (This work)
CCH	Y	Y	Y	Y	Y	Y	Y
C ₂ H ₃ CN	Y	N	-	-	-	-	N
CCS	Y	Y	N	N	Y	Y	Y
C ₃ H	Y	N	h	h	h	h	Y
c-C ₃ H	Y	N	N	N	N	Y	Y
c-C ₃ H ₂	Y	Y	Y	Y	Y	Y	Y
l-C ₃ H ₂	Y	N	h	h	h	h	Y
C ₃ N	Y	N	h	h	h	h	Y
C ₃ O	Y	N	h	h	h	h	Y
C ₃ S	Y	Y	r	r	r	r	Y
C ₄ H	Y	Y	h	h	h	h	Y
l-C ₄ H ₂	Y	N	h	h	h	h	Y
C ₅ H	Y	N	r	r	r	r	N
C ₆ H	Y	N	r	r	r	r	N
CH ₃ CCH	Y	Y	N	N	N	Y	Y
CH ₃ CHO	Y	Y	N	N	N	Y	Y
CH ₃ CN	Y	Y	N	N	N	Y	Y
CH ₃ OCH ₃	Y	Y	-	-	-	-	Y
CH ₃ OCHO	Y	Y	N	N	N	Y	Y
CH ₃ OH	Y	Y	N	Y	Y	Y	Y
CN	Y	Y	Y	Y	Y	Y	Y
CO	Y	Y	Y	Y	Y	Y	Y
CS	Y	Y	-	Y	Y	Y	Y
HCCCHO	Y	N	N	N	N	N	N
HC ₃ N	Y	Y	h	h	h	h	Y
HC ₅ N	Y	Y	r	r	r	r	Y
HCCNC	Y	Y	h	h	h	h	N
HCN	Y	Y	Y	Y	Y	Y	Y
HCNO	Y	N	h	h	h	h	N
HCO	Y	Y	-	-	-	-	Y
HCO ⁺	Y	Y	Y	Y	Y	Y	Y
HCS ⁺	Y	Y	r	r	r	r	Y
H ₂ CO	Y	Y	Y	Y	Y	Y	Y
H ₂ CCN	Y	Y	h	h	h	h	N
H ₂ CCO	Y	N	N	N	N	Y	Y
H ₂ CS	Y	Y	N	Y	Y	Y	Y
H ₂ S	h	h	N	N	Y	Y	r
HNC	Y	Y	r	r	r	r	Y
HNCCC	Y	N	h	h	h	h	N
HNCO	Y	Y	N	N	Y	Y	Y
HNO	Y	N	r	r	r	r	Y
HO CN	Y	N	h	h	h	h	Y
HOCO ⁺	Y	N	h	h	h	h	Y
HSCN	Y	N	h	h	h	h	N
NH ₂ CHO	N	Y	-	-	-	-	N
NH ₃ / NH ₂ D	Y	Y	h	h	h	h	Y
N ₂ H ⁺ / N ₂ D ⁺	Y	Y	N	Y	Y	Y	Y
NS	-	-	r	r	r	r	Y
OCS	Y	Y	N	N	Y	Y	Y
SiO	N	Y	N	N	Y	N	N
SO	Y	Y	Y	Y	Y	Y	Y
SO ₂	Y	Y	N	Y	Y	Y	Y
Total	48/50	33/50	7/23	12/24	17/24	23/25	41/52
Fraction	96%	66%	30%	50%	71%	92%	72%

Notes. Data for L1527 and SVS 13A are taken from [Lefloch et al. \(2018\)](#) in the [80 – 116] GHz frequency range, and data for L1489 IRS, B5 IRS 1, L1455 IRS 1 and L1551 IRS 1 (with the superscript ^a) are taken from [Mercimek et al. \(2022\)](#) in the [214.5 – 238] GHz range. Bold-font letters stand for confirmed detections (**Y**) and non-detections (**N**). Dashes (-) stand for species that have not been reported. The letter r (as in "range") indicates that the species that do not have transitions in the frequency ranges of the studies. The letter h (as in "hot") indicates that the species have transitions within the frequency range of the studies but only with high E_{up} values (≥ 50 K) and they were not reported. The "total" line counts the number of **Y** over the number of **Y+N** for each source.

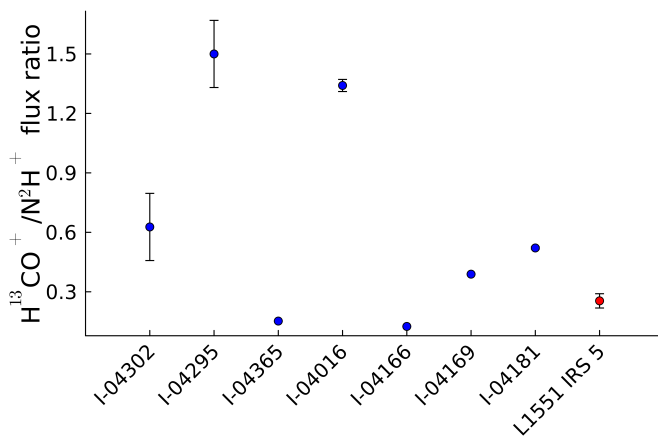


Fig. 9: $H^{13}CO^+ / N_2H^+$ 1-0 line flux ratios for L1551 IRS 5 (red point) compared to the Class I sources in Le Gal et al. (2020) (blue points). Black lines represent error bars. The N_2H^+ line flux for I-04302 provided by Le Gal et al. (2020) is an upper limit.

- We detect 403 molecular lines from 75 chemical species including 38 secondary isotopologues. Among these species, we find 13 hydrocarbons, 25 N-bearing species, 30 O-bearing species, 15 S-bearing species, and 12 deuterated molecules. Ten complex organic molecules ($I-C_4H_2$, CH_3CCH , CH_2DCCH , CH_3CHO , CH_3CN , CH_3OCH_3 , CH_3OCHO , CH_3OH , CH_2DOH , and HC_5N) are also detected. Most lines are centered around the velocity of the envelope $v_{lsr} = 6.4 \text{ km s}^{-1}$, but a few lines are also found around 8.5 km s^{-1} , the velocity of the northern source.
- Column densities, source sizes and excitation temperatures were derived for most detected species with LTE models. When possible, non-LTE models were also used. The models reveal that most species trace the cold envelope with temperatures $\lesssim 10 \text{ K}$: CCH, CCS, C_3H , $c-C_3H_2$, CH_3CHO , CS, HCN, HNC, DCO^+ , $HOCO^+$, N_2D^+ , and their respective isotopologues. We also see several high-temperature ($\gtrsim 30 \text{ K}$) species tracing warmer regions, typically molecules with ≥ 5 atoms such as CH_3CN and HC_5N , and the S-bearing species C_3S , SO, and SO_2 . The lines of CH_3OH and OCS exhibit a component whose emission seems to originate from the warm innermost regions ($< 2''$).
- Using the derived column densities, we calculated isotopic fractionation ratios for C, H, N, O, and S. They are found to be in agreement with other protostellar sources, in particular the $^{33}S/^{32}S$ and $^{34}S/^{32}S$ ratios in CS and SO. The $^{12}C/^{13}C$ ratios are very low for CS, HCN, HNC, and H_2CO , which suggests that their emission is optically thick at those frequencies. We detect both $HC^{15}N$ and $H^{15}NC$ with $^{14}N/^{15}N$ isotopic ratios of ~ 200 and ~ 370 (using the indirect double isotope method with ^{13}C). The $^{16}O/^{18}O$ ratio of HCO^+ when using $H^{13}CO^+$ and a $^{12}C/^{13}C$ of 68 is $\gtrsim 1000$, namely, significantly higher than the values measured in diffuse molecular clouds and L1527. The D/H ratios range from 1% for HCO^+ to 6% for CH_3CCH with in between CCH, $c-C_3H_2$, HCN, and HC_3N that all show D/H ratios close to 3%.
- Comparisons of our results with spectral surveys of other Class I protostars show that there exists a large diversity of chemistry between those sources. The origin of these differences still needs to be explained.

In conclusion, this work is a first step toward improving our understanding of the impact of protostellar outbursts on protostellar envelopes. Additional studies, both theoretical and observational, are needed to further constrain this effect and to provide statistically significant results.

Acknowledgements. This study is part of a project that has received funding from the European Research Council (ERC) under the European Union’s Horizon 2020 research and innovation program (Grant agreement No. 949278, Chemtrip). This work is based on observations carried out under project numbers 047-22, 115-22, and 080-16 with the IRAM 30m telescope. IRAM is supported by INSU/CNRS (France), MPG (Germany) and IGN (Spain). We thank the people at the IRAM-30m facility that were very kind and made these observations possible. This work was also supported by the NKFIH excellence grant TKP2021-NKTA-64.

References

- Agúndez, M., Marcelino, N., Cernicharo, J., Roueff, E., & Tafalla, M. 2019, A&A, 625, A147
 Agúndez, M., Roueff, E., Cabezas, C., Cernicharo, J., & Marcelino, N. 2021, A&A, 649, A171
 Andreu, A., Coutens, A., Cruz-Sáenz de Miera, F., et al. 2023, A&A, 677, L17
 Araki, M., Takano, S., Sakai, N., et al. 2017, Astrophys. J., 847, 51
 Bianchi, E., Ceccarelli, C., Codella, C., et al. 2019, ACS Earth and Space Chemistry, 3, 2659
 Bianchi, E., Chandler, C. J., Ceccarelli, C., et al. 2020, MNRAS, 498, L87
 Bottinelli, S. 2024, CASSIS-LTE-Python, [swsh:1:dir: d5035c6236579dd2adc3ef4b8c86f2ea037405b2;origin=https://gitlab.in2p3.fr/sandrine.bottinelli/cassis-lte-python;visit=swsh:1:snp:f4cc6d47ad48c80bc475f46769b7a5f91a30d6cb;anchor=swsh:1:rev:822ff24749746721c5443b65d2c013893cf89554">swsh:1:dir: d5035c6236579dd2adc3ef4b8c86f2ea037405b2;origin=https://gitlab.in2p3.fr/sandrine.bottinelli/cassis-lte-python;visit=swsh:1:snp:f4cc6d47ad48c80bc475f46769b7a5f91a30d6cb;anchor=swsh:1:rev:822ff24749746721c5443b65d2c013893cf89554](https://gitlab.in2p3.fr/sandrine.bottinelli/cassis-lte-python)
 Bottinelli, S., Ceccarelli, C., Lefloch, B., et al. 2004, Astrophys. J., 615, 354
 Caux, E., Kahane, C., Castets, A., et al. 2011, A&A, 532, A23
 Ceccarelli, C., Caselli, P., Bockelée-Morvan, D., et al. 2014, in Protostars and Planets VI, ed. H. Beuther, R. S. Klessen, C. P. Dullemond, & T. Henning, 859–882
 Ceccarelli, C., Codella, C., Balucani, N., et al. 2023, in Astronomical Society of the Pacific Conference Series, Vol. 534, Protostars and Planets VII, ed. S. Inutsuka, Y. Aikawa, T. Muto, K. Tomida, & M. Tamura, 379
 Cernicharo, J., Marcelino, N., Agúndez, M., et al. 2020, A&A, 642, L8
 Chou, T.-L., Takakuwa, S., Yen, H.-W., Ohashi, N., & Ho, P. T. P. 2014, Astrophys. J., 796, 70
 Colzi, L., Sipilä, O., Roueff, E., Caselli, P., & Fontani, F. 2020, A&A, 640, A51
 Connelley, M. S. & Reipurth, B. 2018, Astrophys. J., 861, 145
 Coutens, A., Commerçon, B., & Wakelam, V. 2020, A&A, 643, A108
 Coutens, A., Vastel, C., Caux, E., et al. 2012, A&A, 539, A132
 Cruz-Sáenz de Miera, F., Kóspál, Á., Ábrahám, P., Liu, H. B., & Takami, M. 2019, Astrophys. J. Lett., 882, L4
 Cruz-Sáenz de Miera et al. in prep.
 Denis-Alpizar, P., Stoecklin, T., Halvick, P., & Duberne, M. 2013, The Journal of Chemical Physics, 139, 20
 Dumouchel, F., Faure, A., & Lique, F. 2010, MNRAS, 406, 2488
 Esplugues, G., Rodriguez-Baras, M., San Andrés, D., et al. 2023, A&A, 678, A199
 Faure, A., Hily-Blant, P., Rist, C., et al. 2019, MNRAS, 487, 3392
 Faure, A., Lique, F., & Wiesenfeld, L. 2016, MNRAS, 460, 2103
 Fischer, W. J., Hillenbrand, L. A., Herczeg, G. J., et al. 2023, in Astronomical Society of the Pacific Conference Series, Vol. 534, Protostars and Planets VII, ed. S. Inutsuka, Y. Aikawa, T. Muto, K. Tomida, & M. Tamura, 355
 Flower, D. R. 1999, MNRAS, 305, 651
 Fridlund, C. V. M., Bergman, P., White, G. J., Pilbratt, G. L., & Tauber, J. A. 2002, A&A, 382, 573
 Froebrich, D. 2005, Astrophys. J., Suppl. Ser., 156, 169
 Giers, K., Spezzano, S., Alves, F., et al. 2022, A&A, 664, A119
 Giers, K., Spezzano, S., Caselli, P., et al. 2023, A&A, 676, A78
 Gildas Team. 2013, GILDAS: Grenoble Image and Line Data Analysis Software, Astrophysics Source Code Library, record ascl:1305.010
 Goicoechea, J. R., Lique, F., & Santa-Maria, M. G. 2022, A&A, 658, A28
 Goldsmith, P. F. & Langer, W. D. 1999, Astrophys. J., 517, 209
 Hernández Vera, M., Lique, F., Dumouchel, F., Hily-Blant, P., & Faure, A. 2017, MNRAS, 468, 1084
 Hsieh, T.-H., Murillo, N. M., Belloche, A., et al. 2019, Astrophys. J., 884, 149
 Ikeda, M., Hirota, T., & Yamamoto, S. 2002, Astrophys. J., 575, 250
 Jensen, S. S., Spezzano, S., Caselli, P., et al. 2024, arXiv e-prints, arXiv:2403.04408
 Jørgensen, J. K., Müller, H. S. P., Calcutt, H., et al. 2018, A&A, 620, A170

- Jørgensen, J. K., Schöier, F. L., & van Dishoeck, E. F. 2004, A&A, 416, 603
 Kaifu, N., Suzuki, S., Hasegawa, T., et al. 1984, A&A, 134, 7
 Le Gal, R., Öberg, K. I., Huang, J., et al. 2020, Astrophys. J., 898, 131
 Lefloch, B., Bachiller, R., Ceccarelli, C., et al. 2018, MNRAS, 477, 4792
 Linsky, J. L. 2003, Space Sci. Rev., 106, 49
 Lique, F., Spielfiedel, A., & Cernicharo, J. 2006, A&A, 451, 1125
 Liseau, R., Fridlund, C. V. M., & Larsson, B. 2005, Astrophys. J., 619, 959
 Loison, J.-C., Wakelam, V., Gratier, P., & Hickson, K. M. 2020, MNRAS, 498, 4663
 Looney, L. W., Mundy, L. G., & Welch, W. J. 1997, Astrophys. J., Lett., 484, L157
 Lucas, R. & Liszt, H. 1998, A&A, 337, 246
 Magalhães, V. S., Hily-Blant, P., Faure, A., Hernandez-Vera, M., & Lique, F. 2018, A&A, 615, A52
 Marcelino, N., Brünken, S., Cernicharo, J., et al. 2010, A&A, 516, A105
 Markwick, A. J., Millar, T. J., & Charnley, S. B. 2002, A&A, 381, 560
 Mercimek, S., Codella, C., Podio, L., et al. 2022, A&A, 659, A67
 Milam, S. N., Savage, C., Brewster, M. A., Ziurys, L. M., & Wyckoff, S. 2005, Astrophys. J., 634, 1126
 Minissale, M., Aikawa, Y., Bergin, E., et al. 2022, ACS Earth and Space Chemistry, 6, 597
 Müller, H. S. P., Schlöder, F., Stutzki, J., & Winnewisser, G. 2005, Journal of Molecular Structure, 742, 215
 Müller, H. S. P., Thorwirth, S., Roth, D. A., & Winnewisser, G. 2001, A&A, 370, L49
 Ohashi, N., Hayashi, M., Ho, P. T. P., Momose, M., & Hirano, N. 1996, Astrophys. J., 466, 957
 Osorio, M., D'Alessio, P., Muzerolle, J., Calvet, N., & Hartmann, L. 2003, Astrophys. J., 586, 1148
 Parise, B., Caux, E., Castets, A., et al. 2005, A&A, 431, 547
 Pickett, H. M., Poynter, R. L., Cohen, E. A., et al. 1998, J. Quant. Spectr. Rad. Transf., 60, 883
 Rab, C., Elbakyan, V., Vorobyov, E., et al. 2017, A&A, 604, A15
 Riaz, B. & Thi, W. F. 2022, MNRAS, 511, 6110
 Roberts, H., Fuller, G. A., Millar, T. J., Hatchell, J., & Buckle, J. V. 2002, A&A, 381, 1026
 Roueff, E., Loison, J. C., & Hickson, K. M. 2015, A&A, 576, A99
 Sakai, N., Sakai, T., Hirota, T., & Yamamoto, S. 2008, Astrophys. J., 672, 371
 Sakai, N., Saruwatari, O., Sakai, T., Takano, S., & Yamamoto, S. 2010, A&A, 512, A31
 Takakuwa, S., Saigo, K., Matsumoto, T., et al. 2020, Astrophys. J., 898, 10
 Tatematsu, K., Umemoto, T., Kandori, R., & Sekimoto, Y. 2004, Astrophys. J., 606, 333
 Turner, B. E., Herbst, E., & Terzieva, R. 2000, Astrophys. J., Suppl. Ser., 126, 427
 van der Tak, F. F. S., Black, J. H., Schöier, F. L., Jansen, D. J., & van Dishoeck, E. F. 2007, A&A, 468, 627
 Vastel, C., Caselli, P., Ceccarelli, C., et al. 2006, Astrophys. J., 645, 1198
 Visser, R., Bergin, E. A., & Jørgensen, J. K. 2015, A&A, 577, A102
 Wampfler, S. F., Jørgensen, J. K., Bizzarro, M., & Bisschop, S. E. 2014, A&A, 572, A24
 Wiesenfeld, L. & Faure, A. 2013, MNRAS, 432, 2573
 Wilson, T. L. 1999, Reports on Progress in Physics, 62, 143
 Yan, Y. T., Henkel, C., Kobayashi, C., et al. 2023, A&A, 670, A98
 Yang, Y.-L., Evans, N. J., Karska, A., et al. 2022, Astrophys. J., 925, 93
 Yoshida, K., Sakai, N., Nishimura, Y., et al. 2019, PASJ, 71, S18
 Zucker, C., Speagle, J. S., Schlafly, E. F., et al. 2019, Astrophys. J., 879, 125

Appendix A: Detected lines

Table A.1: Identified lines in the survey. Line characteristics (columns 1 to 6) : frequency in GHz, species name, molecular tag, coefficient in s^{-1} . Gaussian fitting parameters (columns 7 to 14): FWHM in km s^{-1} , error on the FWHM, velocity shift in km s^{-1} , error on the velocity shift, intensity in K, error on the intensity, Gaussian flux in K km s^{-1} , and error on the Gaussian flux. An empty fitting parameter indicates that the line is blended with the line just above.

Freq. (GHz)	Species	Tag	Transition	E_{up} (K)	A_{ij} (s^{-1})	FWHM (km s^{-1})	δFWHM (km s^{-1})	v (km s^{-1})	δv (km s^{-1})	Int (K)	δInt (K)	Flux (K km s^{-1})	δFlux (K km s^{-1})
87.2841	CCH	25501	1 1.5 1 - 0 0.5 1	4.19	2.60×10^{-7}	1.035	0.0176	6.5652	0.0076	0.3988	0.0056	0.4394	0.0097
87.3169	CCH	25501	1 1.5 2 - 0 0.5 1	4.19	1.53×10^{-6}	1.0501	0.0236	6.5589	0.0078	2.434	0.0405	2.7208	0.0761
87.3286	CCH	25501	1 1.5 1 - 0 0.5 0	4.19	1.27×10^{-6}	1.0708	0.0171	6.5329	0.0046	1.3954	0.0165	1.5905	0.0316
87.4020	CCH	25501	1 0.5 1 - 0 0.5 1	4.2	1.27×10^{-6}	1.1387	0.0119	6.5709	0.0041	1.3772	0.0111	1.6693	0.0222
87.4072	CCH	25501	1 0.5 0 - 0 0.5 1	4.2	1.54×10^{-6}	1.0094	0.0091	6.5947	0.0044	0.7321	0.0056	0.7866	0.0093
87.4465	CCH	25501	1 0.5 1 - 0 0.5 0	4.2	2.61×10^{-7}	1.0434	0.0074	6.6026	0.0042	0.3963	0.0026	0.4402	0.0043
72.1018	CCD	26501	1 1.5 1.5 - 0 0.5 1.5	3.46	3.28×10^{-7}	1.1752	0.02261	6.5954	0.1391	0.0206	0.0036	0.0257	0.0067
72.1077	CCD	26501	1 1.5 2.5 - 0 0.5 1.5	3.46	8.60×10^{-7}	0.9035	0.22	6.4646	0.0632	0.0804	0.0201	0.0774	0.0277
72.1091	CCD	26501	1 1.5 0.5 - 0 0.5 0.5	3.46	7.84×10^{-7}	0.9334	0.65553	6.3623	0.2627	0.0187	0.0117	0.0186	0.0175
72.1123	CCD	26501	1 1.5 1.5 - 0 0.5 0.5	3.46	5.32×10^{-7}	1.1916	0.3242	6.4922	0.1309	0.0234	0.0052	0.0297	0.0104
72.1877	CCD	26501	1 0.5 1.5 - 0 0.5 1.5	3.46	5.34×10^{-7}	0.9497	0.1622	6.3867	0.1336	0.0314	0.004	0.0318	0.0068
72.1897	CCD	26501	1 0.5 0.5 - 0 0.5 1.5	3.46	7.86×10^{-7}	1.2559	0.2433	6.514	0.122	0.0214	0.0037	0.0286	0.0074
144.2419	CCD	26501	2 2.5 3.5 - 1 1.5 2.5	10.38	8.26×10^{-6}	0.7159	0.0904	6.3732	0.0394	0.1627	0.0178	0.124	0.0207
144.2430	CCD	26501	2 2.5 1.5 - 1 1.5 0.5	10.38	6.28×10^{-6}	0.8894	0.1252	6.3075	0.0527	0.1334	0.0162	0.1263	0.0235
144.2431	CCD	26501	2 2.5 2.5 - 1 1.5 1.5	10.38	7.03×10^{-6}	0.8998	0.1244	6.476	0.0525	0.134	0.016	0.1284	0.0235
144.2967	CCD	26501	2 1.5 2.5 - 1 0.5 1.5	10.39	6.73×10^{-6}	0.9242	0.1599	6.4853	0.0683	0.1	0.015	0.0984	0.0225
85.2293	C^{13}CH	26503	1 1.5 2.2.5 - 0 0.5 1.5	4.1	1.42×10^{-6}	1.1676	0.0949	6.6202	0.0442	0.0265	0.0019	0.0329	0.0045
85.2328	C^{13}CH	26503	1 1.5 2 1.5 - 0 0.5 1.0.5	4.1	1.34×10^{-6}	1.0539	0.1585	6.6261	0.0841	0.0203	0.0027	0.0227	0.0038
85.2477	C^{13}CH	26503	1 1.5 1 0.5 - 0 0.5 0.5	4.09	1.39×10^{-6}	1.2805	0.3604	6.7222	0.1656	0.0123	0.0031	0.0168	0.0044
85.257	C^{13}CH	26503	1 1.5 1 1.5 - 0 0.5 0.5	4.09	1.36×10^{-6}	1.7914	0.3949	6.5769	0.1654	0.0125	0.0024	0.0238	0.0049
85.3075	C^{13}CH	26503	1 0.5 1 1.5 - 0 0.5 1.1.5	4.1	1.29×10^{-6}	1.2398	0.188	6.7069	0.0919	0.0183	0.0025	0.0242	0.0042
72.3238	CCS	56502	6 5 - 5 4	19.21	1.60×10^{-5}	1.0903	0.1848	6.6952	0.0461	0.0604	0.0083	0.0701	0.0153
77.7317	CCS	56502	6 6 - 5 5	21.76	2.03×10^{-5}	1.1005	0.074	6.6721	0.0464	0.0586	0.0037	0.0686	0.0063
81.5052	CCS	56502	6 7 - 5 6	15.39	2.43×10^{-5}	1.1043	0.0365	6.5519	0.0213	0.174	0.0054	0.2045	0.0093
86.1814	CCS	56502	7 6 - 6 5	23.35	2.78×10^{-5}	1.3116	0.0933	6.6856	0.0362	0.0521	0.0031	0.0727	0.0067
90.6864	CCS	56502	7 7 - 6 6	26.12	3.29×10^{-5}	1.0111	0.0873	6.7777	0.0261	0.0668	0.0045	0.0719	0.0079
93.8701	CCS	56502	7 8 - 6 7	19.89	3.74×10^{-5}	1.2509	0.03	6.7524	0.0118	0.1382	0.0028	0.1841	0.0058
99.8665	CCS	56502	8 7 - 7 6	28.14	4.40×10^{-5}	1.0301	0.0796	6.8306	0.0316	0.0633	0.0041	0.0694	0.007
103.6408	CCS	56502	8 8 - 7 7	31.09	4.98×10^{-5}	1.1411	0.0785	6.6828	0.035	0.0486	0.003	0.0591	0.0055
106.3477	CCS	56502	8 9 - 7 8	25.0	5.48×10^{-5}	1.0911	0.0353	6.6893	0.0153	0.1323	0.0037	0.1537	0.0066
113.4102	CCS	56502	9 8 - 8 7	33.58	6.53×10^{-5}	0.8274	0.1196	6.7051	0.0383	0.0601	0.0069	0.053	0.0098
140.1807	CCS	56502	11 10 - 10 9	46.4	1.26×10^{-4}	1.2899	0.2739	6.5028	0.1153	0.0379	0.0069	0.052	0.0145
142.5017	CCS	56502	11 11 - 10 10	49.74	1.33×10^{-4}	0.6294	0.1148	6.4073	0.0674	0.0525	0.009	0.0351	0.0088
144.2448	CCS	56502	11 12 - 10 11	43.94	1.39×10^{-4}	0.564	0.1368	6.6414	0.0859	0.0822	0.0176	0.0494	0.0116
153.4498	CCS	56502	12 11 - 11 10	53.76	1.66×10^{-4}	1.4586	0.1967	6.5169	0.0827	0.0281	0.0033	0.0437	0.0078
155.4545	CCS	56502	12 12 - 11 11	57.2	1.73×10^{-4}	1.1142	0.1238	6.5503	0.0518	0.0363	0.0035	0.0431	0.0063

Table A.1 continued

Freq. (GHz)	Species	Tag	Transition	E_{up} (K)	A_{ij} (s $^{-1}$)	FWHM (km s $^{-1}$)	δFWHM (km s $^{-1}$)	v (km s $^{-1}$)	δv (km s $^{-1}$)	Int (K)	δInt (K)	Flux (K km s $^{-1}$)	δFlux (K km s $^{-1}$)
156.9817	CCS	56502	12 13 - 11 12	51.47	1.80×10^{-4}	1.0882	0.0833	6.5033	0.0351	0.0608	0.004	0.0704	0.0071
76.1987	C ₃ H	37501	4 1 0 3.54 - 3 -1 0 2.5 3	7.83	2.78×10^{-5}	1.055	0.1462	6.6106	0.0869	0.0322	0.0038	0.0362	0.0066
76.1999	C ₃ H	37501	4 1 0 3.5 3 - 3 -1 0 2.5 2	7.83	2.64×10^{-5}	1.1507	0.1834	6.6282	0.1122	0.0238	0.0036	0.0292	0.0064
76.2042	C ₃ H	37501	4 -1 0 3.54 - 3 1 0 2.5 3	7.84	2.78×10^{-5}	1.1077	0.1179	6.5347	0.0706	0.0328	0.0031	0.0387	0.0055
76.2051	C ₃ H	37501	4 -1 0 3.5 3 - 3 1 0 2.5 2	7.84	2.64×10^{-5}	1.4364	0.4178	6.7378	0.1601	0.0137	0.0033	0.021	0.0079
97.9952	C ₃ H	37501	4 1 0 4.5 5 - 4 -1 0 3.5 4	12.54	6.12×10^{-5}	1.0765	0.1314	6.3909	0.0625	0.0269	0.003	0.0308	0.0051
97.9959	C ₃ H	37501	4 1 0 4.5 4 - 4 -1 0 3.5 3	12.54	5.95×10^{-5}	1.0632	0.1609	6.3715	0.0678	0.023	0.003	0.0261	0.0052
98.0116	C ₃ H	37501	4 -1 0 4.5 5 - 4 -1 0 3.5 4	12.54	6.13×10^{-5}	0.9051	0.1043	6.5215	0.0573	0.0283	0.0029	0.0273	0.0042
98.0125	C ₃ H	37501	4 -1 0 4.5 4 - 4 -1 0 3.5 3	12.54	5.96×10^{-5}	0.8917	0.1687	6.3822	0.0775	0.0248	0.0039	0.0236	0.0058
91.4976	c-C ₃ H	37003	2 1 2 2.5 2 - 1 1 1 1.5 1	4.39	1.38×10^{-5}	0.9398	0.0617	6.83	0.0334	0.0565	0.0033	0.0566	0.005
91.6995	c-C ₃ H	37003	2 1 2 1.5 2 - 1 1 1 0.5 1	4.4	1.37×10^{-5}	0.9664	0.1415	6.678	0.0431	0.0497	0.0057	0.0511	0.0095
91.4943	c-C ₃ H	37003	2 1 2 2.5 3 - 1 1 1 1.5 2	4.39	1.59×10^{-5}	1.0266	0.0599	6.7286	0.0216	0.0774	0.0036	0.0846	0.0063
77.1000	c-C ₃ H ₂	38508	5 3 2 - 5 2 3	44.72	1.40×10^{-5}	0.9896	0.1037	6.3688	0.0704	0.0628	0.0055	0.0661	0.009
80.7232	c-C ₃ H ₂	38508	4 2 2 - 4 1 3	28.82	1.33×10^{-5}	0.884	0.6573	6.2124	0.2455	0.0469	0.0229	0.0441	0.0392
82.0935	c-C ₃ H ₂	38508	2 0 2 - 1 1 1	6.43	1.89×10^{-5}	0.9947	0.013	6.5385	0.0086	0.5074	0.006	0.5372	0.0095
82.9662	c-C ₃ H ₂	38508	3 1 2 - 3 0 3	16.05	9.92×10^{-6}	1.0269	0.0456	6.3943	0.0096	0.2704	0.0093	0.2956	0.0166
84.7277	c-C ₃ H ₂	38508	3 2 2 - 3 1 3	16.14	1.04×10^{-5}	0.9093	0.0234	6.4166	0.016	0.123	0.0027	0.1191	0.004
85.3389	c-C ₃ H ₂	38508	2 1 2 - 1 0 1	6.45	2.32×10^{-5}	1.0639	0.0032	6.5507	0.0016	1.5677	0.0042	1.7755	0.0072
85.6564	c-C ₃ H ₂	38508	4 3 2 - 4 2 3	29.07	1.52×10^{-5}	0.9192	0.0204	6.4398	0.0124	0.159	0.003	0.1555	0.0045
87.4353	c-C ₃ H ₂	38508	5 4 2 - 5 3 3	45.26	1.85×10^{-5}	0.6502	0.193	6.5359	0.1892	0.0204	0.0029	0.0141	0.0046
90.3441	c-C ₃ H ₂	38508	6 5 2 - 6 4 3	64.71	2.16×10^{-5}	1.4305	0.2702	6.3783	0.1115	0.018	0.0029	0.0274	0.0068
112.4908	c-C ₃ H ₂	38508	7 4 3 - 7 3 4	82.64	4.10×10^{-5}	1.1712	0.2433	6.443	0.1011	0.0236	0.0042	0.0295	0.0081
145.0896	c-C ₃ H ₂	38508	3 1 2 - 2 2 1	16.05	6.77×10^{-5}	0.8128	0.0161	6.4139	0.0072	1.0519	0.0184	0.9102	0.0241
151.3439	c-C ₃ H ₂	38508	5 1 4 - 5 0 5	35.42	3.96×10^{-5}	0.8521	0.022	6.3431	0.0095	0.1969	0.0044	0.1786	0.0061
151.3611	c-C ₃ H ₂	38508	5 2 4 - 5 1 5	35.42	3.96×10^{-5}	0.8209	0.0594	6.3523	0.0258	0.0644	0.0041	0.0563	0.0054
155.5183	c-C ₃ H ₂	38508	3 2 2 - 2 1 1	16.14	1.12×10^{-4}	0.7717	0.0106	6.3964	0.0043	0.581	0.0067	0.4772	0.0086
79.8123	c-C ₃ HD	39508	2 1 2 - 1 0 1	5.85	1.64×10^{-5}	0.8822	0.1341	6.5016	0.1025	0.0506	0.0059	0.0475	0.0091
77.1884	c-C ₃ HD	39508	2 0 2 - 1 0 1	5.72	2.81×10^{-6}	0.869	0.2764	6.6575	0.2313	0.0136	0.0031	0.0126	0.0049
106.2561	c-C ₃ HD	39508	4 1 3 - 4 0 4	22.3	1.53×10^{-5}	0.8214	0.3289	6.3372	0.0865	0.0184	0.0058	0.016	0.0082
102.4223	c-C ₃ HD	39508	3 0 3 - 2 1 2	10.85	3.96×10^{-5}	0.7718	0.0333	6.3795	0.0219	0.0929	0.0036	0.0763	0.0044
104.1871	c-C ₃ HD	39508	3 1 3 - 2 1 2	10.88	7.29×10^{-6}	0.8571	0.1971	6.4516	0.0818	0.021	0.004	0.0192	0.0057
104.7997	c-C ₃ HD	39508	4 2 3 - 4 1 4	22.49	1.69×10^{-5}	1.0278	0.2554	6.4179	0.111	0.015	0.0032	0.0164	0.0054
106.8111	c-C ₃ HD	39508	3 0 3 - 2 0 2	10.85	7.87×10^{-6}	0.6616	0.2154	6.2198	0.1439	0.0166	0.0041	0.0117	0.0048
107.4237	c-C ₃ HD	39508	3 1 3 - 2 0 2	10.88	4.47×10^{-5}	0.9071	0.0707	6.3562	0.0251	0.0796	0.005	0.0768	0.0077
135.6409	c-C ₃ HD	39508	4 0 4 - 3 1 3	17.39	9.92×10^{-5}	0.782	0.09	6.224	0.0399	0.0878	0.0088	0.0731	0.0112
136.3709	c-C ₃ HD	39508	4 1 4 - 3 0 3	17.39	1.01×10^{-4}	0.6048	0.0997	6.2974	0.0338	0.1004	0.0132	0.0647	0.0136
137.4545	c-C ₃ HD	39508	2 2 0 - 1 1 1	8.98	4.88×10^{-5}	0.5903	0.1079	6.6395	0.0542	0.0631	0.0095	0.0396	0.0094
158.4208	c-C ₃ HD	39508	4 1 3 - 3 2 2	22.3	8.87×10^{-5}	0.8108	0.091	6.3387	0.038	0.0493	0.0048	0.0426	0.0063
84.1856	c-CC ¹³ CH ₂	39510	2 1 2 - 1 0 1	6.33	2.17×10^{-5}	1.0515	0.2479	6.4005	0.0635	0.0311	0.0057	0.0348	0.0104
114.8974	c-CC ¹³ CH ₂	39510	3 0 3 - 2 1 2	11.85	6.37×10^{-5}	1.1483	0.2246	6.5074	0.0946	0.038	0.0064	0.0465	0.012

Table A.1 continued

Freq. (GHz)	Species	Tag	Transition	E_{up} (K)	A_{ij} (s $^{-1}$)	FWHM (km s $^{-1}$)	δFWHM (km s $^{-1}$)	v (km s $^{-1}$)	δv (km s $^{-1}$)	Int (K)	δInt (K)	Flux (K km s $^{-1}$)	δFlux (K km s $^{-1}$)	
115.5244	c-CC $^{13}\text{CH}_2$	39510	3 1 3 - 2 0 2	11.85	6.50×10^{-5}	0.8954	0.2012	6.23558	0.1013	0.0359	0.0075	0.0342	0.0105	
153.8946	c-CC $^{13}\text{CH}_2$	39510	3 2 2 - 2 1 1	15.85	1.05×10^{-4}	0.7995	0.1047	6.3192	0.0437	0.0404	0.0045	0.0344	0.0059	
82.3951	1-C $_3\text{H}_2$	38501	4 1 4 - 3 1 3	23.24	4.56×10^{-5}	0.9402	0.6489	6.5388	0.1494	0.0276	0.0157	0.0277	0.0248	
83.9337	1-C $_3\text{H}_2$	38501	4 1 3 - 3 1 2	23.43	4.82×10^{-5}	1.174	0.2486	6.6104	0.0876	0.0268	0.0046	0.0335	0.0091	
102.9924	1-C $_3\text{H}_2$	38501	5 1 5 - 4 1 4	28.19	9.33×10^{-5}	1.0872	0.1422	6.4957	0.0534	0.0343	0.0037	0.0397	0.0067	
103.9529	1-C $_3\text{H}_2$	38501	5 0 5 - 4 0 4	14.97	9.99×10^{-5}	0.9642	0.2311	6.4898	0.0784	0.0231	0.0044	0.0237	0.0073	
104.9156	1-C $_3\text{H}_2$	38501	5 1 4 - 4 1 3	28.46	9.86×10^{-5}	1.8108	0.2373	6.4956	0.0996	0.0216	0.0024	0.0417	0.0072	
79.1510	C $_3\text{N}$	50511	8 8.5 7.5 - 7 7.5 6.5	17.09	2.17×10^{-5}	1.0962	0.3435	6.7784	0.1489	0.0154	0.004	0.018	0.0073	
79.1510	C $_3\text{N}$	50511	8 8.5 8.5 - 7 7.5 7.5	17.09	2.18×10^{-5}	-	-	-	-	-	-	-	-	
79.1510	C $_3\text{N}$	50511	8 8.5 9.5 - 7 7.5 8.5	17.09	2.21×10^{-5}	-	-	-	-	-	-	-	-	
79.1697	C $_3\text{N}$	50511	8 7.5 6.5 - 7 6.5 5.5	17.1	2.14×10^{-5}	0.9225	0.4464	6.8811	0.2351	0.0124	0.0047	0.0122	0.0075	
79.1698	C $_3\text{N}$	50511	8 7.5 7.5 - 7 6.5 6.5	17.1	2.15×10^{-5}	-	-	-	-	-	-	-	-	
79.1698	C $_3\text{N}$	50511	8 7.5 8.5 - 7 6.5 7.5	17.1	2.19×10^{-5}	-	-	-	-	-	-	-	-	
89.0643	C $_3\text{N}$	50511	9 8.5 7.5 - 8 7.5 6.5	21.37	3.09×10^{-5}	1.1363	0.3864	6.7978	0.1261	0.0129	0.0034	0.0156	0.0067	
89.0644	C $_3\text{N}$	50511	9 8.5 8.5 - 8 7.5 7.5	21.37	3.10×10^{-5}	-	-	-	-	-	-	-	-	
89.0644	C $_3\text{N}$	50511	9 8.5 9.5 - 8 7.5 8.5	21.37	3.14×10^{-5}	-	-	-	-	-	-	-	-	
98.9400	C $_3\text{N}$	50511	10 10.5 9.5 - 9 9.5 8.5	26.11	4.32×10^{-5}	0.9485	0.1711	6.7513	0.0938	0.0145	0.0024	0.0147	0.0036	
98.9400	C $_3\text{N}$	50511	10 10.5 10.5 - 9 9.5 9.5	26.11	4.32×10^{-5}	-	-	-	-	-	-	-	-	
98.9588	C $_3\text{N}$	50511	10 10.5 11.5 - 9 9.5 10.5	26.11	4.36×10^{-5}	-	-	-	-	-	-	-	-	
98.9588	C $_3\text{N}$	50511	10 9.5 8.5 - 9 8.5 7.5	26.12	4.29×10^{-5}	1.0833	0.2567	6.8441	0.1192	0.0125	0.0027	0.0145	0.0046	
98.9588	C $_3\text{N}$	50511	10 9.5 9.5 - 9 8.5 8.5	26.12	4.29×10^{-5}	-	-	-	-	-	-	-	-	
98.9588	C $_3\text{N}$	50511	10 9.5 10.5 - 9 8.5 9.5	26.12	4.34×10^{-5}	-	-	-	-	-	-	-	-	
76.9726	C $_3\text{O}$	52501	8 - 7	16.62	1.43×10^{-5}	1.2469	0.5066	6.5607	0.2239	0.0092	0.0032	0.0122	0.0065	
86.5937	C $_3\text{O}$	52501	9 - 8	20.78	2.05×10^{-5}	0.8173	0.5091	6.5826	0.1872	0.0156	0.0084	0.0136	0.0112	
96.2146	C $_3\text{O}$	52501	10 - 9	25.4	2.82×10^{-5}	-	1.742	0.4995	6.6848	0.2056	0.0117	0.0028	0.0216	0.0081
105.8354	C $_3\text{O}$	52501	11 - 10	30.48	3.77×10^{-5}	1.0956	0.2335	6.4998	0.1013	0.0149	0.0028	0.0174	0.0049	
75.1479	C $_3\text{S}$	68503	13 - 12	25.25	3.26×10^{-5}	1.1723	0.2205	6.9294	0.1115	0.0248	0.0041	0.0309	0.0077	
80.9282	C $_3\text{S}$	68503	14 - 13	29.13	4.09×10^{-5}	1.0545	0.5232	6.4426	0.1419	0.0241	0.0093	0.0271	0.017	
92.4885	C $_3\text{S}$	68503	16 - 15	37.73	6.13×10^{-5}	0.9121	0.4806	6.5709	0.1999	0.0105	0.0045	0.0102	0.0069	
104.0485	C $_3\text{S}$	68503	18 - 17	47.44	8.75×10^{-5}	1.4118	0.2432	6.6125	0.1018	0.0172	0.0025	0.0258	0.0058	
76.1174	C $_4\text{H}$	49503	8 8.5 8 - 7 7.5 7	16.44	1.06×10^{-5}	1.0224	0.0823	6.6982	0.0157	0.161	0.0107	0.1753	0.0183	
76.1174	C $_4\text{H}$	49503	8 8.5 9 - 7 7.5 8	16.44	1.07×10^{-5}	-	-	-	-	-	-	-	-	
76.1174	C $_4\text{H}$	49503	8 7.5 7 - 7 6.5 6	16.45	1.05×10^{-5}	1.063	0.0365	6.6469	0.0178	0.141	0.004	0.1595	0.0071	
76.1174	C $_4\text{H}$	49503	8 7.5 8 - 7 6.5 7	16.45	1.06×10^{-5}	-	-	-	-	-	-	-	-	
85.6334	C $_4\text{H}$	49503	9 9.5 9 - 8 8.5 8	20.55	1.52×10^{-5}	1.0522	0.0211	6.6877	0.0125	0.1427	0.0027	0.1599	0.0044	
95.1504	C $_4\text{H}$	49503	10 10.5 10 - 9 9.5 9	25.11	2.10×10^{-5}	1.2922	0.04	6.63	0.0168	0.1137	0.003	0.1565	0.0064	
95.1504	C $_4\text{H}$	49503	10 10.5 11 - 9 9.5 10	25.11	2.11×10^{-5}	-	-	-	-	-	-	-	-	

Table A.1 continued

Freq. (GHz)	Species	Tag	Transition	E_{up} (K)	A_{ij} (s $^{-1}$)	FWHM (km s $^{-1}$)	δFWHM (km s $^{-1}$)	v (km s $^{-1}$)	δv (km s $^{-1}$)	Int (K)	δInt (K)	Flux (K km s $^{-1}$)	δFlux (K km s $^{-1}$)
95.1889	C ₄ H	49503	10 9.5 9 – 9 8.5 8	25.13	2.08×10^{-5}	1.2818	0.0348	6.6027	0.0146	0.0993	0.0023	0.1355	0.0048
95.1889	C ₄ H	49503	10 9.5 10 – 9 8.5 9	25.13	2.10×10^{-5}	-	-	-	-	-	-	-	-
104.6666	C ₄ H	49503	11 11.5 11 – 10 10.5 10	30.14	2.80×10^{-5}	0.9986	0.0364	6.6017	0.0136	0.1205	0.0035	0.1281	0.006
104.6666	C ₄ H	49503	11 11.5 12 – 10 10.5 11	30.14	2.81×10^{-5}	-	-	-	-	-	-	-	-
104.7051	C ₄ H	49503	11 10.5 10 – 10 9.5 9	30.16	2.79×10^{-5}	1.133	0.0455	6.571	0.0187	0.1023	0.0035	0.1234	0.0065
104.7051	C ₄ H	49503	11 10.5 11 – 10 9.5 10	30.16	2.81×10^{-5}	-	-	-	-	-	-	-	-
114.1825	C ₄ H	49503	12 12.5 12 – 11 11.5 11	35.62	3.66×10^{-5}	1.155	0.0734	6.6099	0.0313	0.094	0.0052	0.1155	0.0097
114.1825	C ₄ H	49503	12 12.5 13 – 11 11.5 12	35.62	3.67×10^{-5}	-	-	-	-	-	-	-	-
114.2210	C ₄ H	49503	12 11.5 11 – 11 10.5 10	35.64	3.64×10^{-5}	1.0421	0.0741	6.5774	0.0309	0.0987	0.006	0.1095	0.0102
114.2210	C ₄ H	49503	12 11.5 12 – 11 10.5 11	35.64	3.66×10^{-5}	-	-	-	-	-	-	-	-
142.7288	C ₄ H	49503	15 15.5 15 – 14 14.5 14	54.8	7.21×10^{-5}	0.7302	0.1296	6.5812	0.0632	0.0571	0.0093	0.0444	0.0107
142.7288	C ₄ H	49503	15 15.5 16 – 14 14.5 15	54.79	7.22×10^{-5}	-	-	-	-	-	-	-	-
142.7673	C ₄ H	49503	15 14.5 14 – 14 13.5 13	54.82	7.19×10^{-5}	0.9244	0.1752	6.5937	0.0739	0.0495	0.0081	0.0487	0.0122
142.7673	C ₄ H	49503	15 14.5 15 – 14 13.5 14	54.82	7.21×10^{-5}	-	-	-	-	-	-	-	-
152.2436	C ₄ H	49503	16 16.5 16 – 15 15.5 15	62.1	8.77×10^{-5}	1.0225	0.0933	6.6499	0.0388	0.0497	0.0039	0.0541	0.0065
152.2436	C ₄ H	49503	16 16.5 17 – 15 15.5 16	62.1	8.78×10^{-5}	-	-	-	-	-	-	-	-
152.2821	C ₄ H	49503	16 15.5 15 – 15 14.5 14	62.13	8.75×10^{-5}	1.0616	0.0942	6.5854	0.0396	0.0498	0.0038	0.0563	0.0066
152.2821	C ₄ H	49503	16 15.5 16 – 15 14.5 15	62.13	8.77×10^{-5}	-	-	-	-	-	-	-	-
88.9402	1-C ₄ H ₂	50503	10 11.0 – -9 19	37.0	6.49×10^{-5}	0.8197	0.5155	6.4575	0.0524	0.0249	0.0143	0.0217	0.0185
89.3145	1-C ₄ H ₂	50503	10 0.10 – -9 09	23.58	6.64×10^{-5}	1.5607	0.4401	6.0923	0.1836	0.0125	0.003	0.0208	0.0077
89.687	1-C ₄ H ₂	50503	10 19 – -9 18	37.2	6.65×10^{-5}	1.0541	0.2124	6.4745	0.1026	0.0177	0.0031	0.0198	0.0053
97.8336	1-C ₄ H ₂	50503	11 11.11 – -10 11.0	41.69	8.69×10^{-5}	0.9545	0.2633	6.4907	0.0905	0.0131	0.0029	0.0133	0.0047
98.6551	1-C ₄ H ₂	50503	11 11.0 – -10 19	41.93	8.91×10^{-5}	1.1585	0.2112	6.4516	0.0857	0.0223	0.0034	0.0275	0.0066
106.7268	1-C ₄ H ₂	50503	12 11.2 – -11 11.1	46.82	1.13×10^{-4}	1.3261	0.2539	6.7288	0.1074	0.0189	0.0031	0.0267	0.0067
107.175	1-C ₄ H ₂	50503	12 0.12 – -10 11	33.43	1.16×10^{-4}	0.8502	0.2589	6.3855	0.1417	0.0139	0.0039	0.0125	0.0052
85.4508	CH ₃ CCH	40502	5 2 – 4 2	41.21	1.70×10^{-6}	0.8488	0.1407	6.5166	0.1094	0.0231	0.0031	0.0209	0.0045
85.4557	CH ₃ CCH	40502	5 1 – 4 1	19.53	1.95×10^{-6}	0.9828	0.0363	6.4799	0.0203	0.1027	0.0033	0.1074	0.0053
85.4573	CH ₃ CCH	40502	5 0 – 4 0	12.3	2.03×10^{-6}	0.9075	0.0527	6.3488	0.0185	0.1303	0.0061	0.1259	0.0094
102.5401	CH ₃ CCH	40502	6 2 – 5 2	46.13	3.16×10^{-6}	0.9422	0.1712	6.3912	0.0762	0.0232	0.0036	0.0233	0.0056
102.5460	CH ₃ CCH	40502	6 1 – 5 1	24.45	3.46×10^{-6}	0.9856	0.03	6.3774	0.0109	0.1258	0.0031	0.132	0.0052
102.5480	CH ₃ CCH	40502	6 0 – 5 0	17.23	3.56×10^{-6}	0.9464	0.0268	6.3725	0.0086	0.1508	0.0034	0.152	0.0055
136.7176	CH ₃ CCH	40502	8 2 – 7 2	58.43	8.06×10^{-6}	0.6827	0.147	6.4163	0.0835	0.0384	0.0078	0.0279	0.0083
136.7254	CH ₃ CCH	40502	8 1 – 7 1	36.76	8.47×10^{-6}	0.7953	0.083	6.3482	0.0344	0.1016	0.009	0.086	0.0118
136.7280	CH ₃ CCH	40502	8 0 – 7 0	29.53	8.60×10^{-6}	0.8907	0.0679	6.3705	0.0274	0.1341	0.0086	0.1271	0.0127
153.8055	CH ₃ CCH	40502	9 2 – 8 2	65.82	1.17×10^{-5}	0.9599	0.1052	6.3665	0.0442	0.048	0.0045	0.049	0.0071
153.8143	CH ₃ CCH	40502	9 1 – 8 1	44.14	1.22×10^{-5}	0.834	0.0357	6.3391	0.0153	0.1269	0.0047	0.1127	0.0064
153.8172	CH ₃ CCH	40502	9 0 – 8 0	36.91	1.23×10^{-5}	0.9091	0.0325	6.3559	0.0137	0.1544	0.0048	0.1494	0.0071
97.0807	CH ₂ DCCH	41502	6 0 6 – 5 0 5	16.31	3.02×10^{-6}	2.3403	0.5147	6.7545	0.2039	0.0111	0.002	0.0277	0.0079
113.2582	CH ₂ DCCH	41502	7 0 7 – 6 0 6	21.74	4.85×10^{-6}	1.015	0.3054	6.2778	0.1361	0.0172	0.0046	0.0185	0.0074
74.8917	CH ₃ CHO	44003	4 1 4 0 – 3 1 3 0	11.26	1.24×10^{-5}	1.1364	0.2212	6.5307	0.0637	0.0332	0.0051	0.0401	0.0099

Table A.1 continued

Freq. (GHz)	Species	Tag	Transition	E_{up} (K)	A_{ij} (s $^{-1}$)	FWHM (km s $^{-1}$)	δFWHM (km s $^{-1}$)	v (km s $^{-1}$)	δv (km s $^{-1}$)	Int (K)	δInt (K)	Flux (K km s $^{-1}$)	δFlux (K km s $^{-1}$)
74.9241	CH ₃ CHO	44003	4 1 4 1 – 3 1 3 1	11.33	1.24×10^{-5}	1.4812	0.1917	6.3976	0.0898	0.0272	0.0032	0.0428	0.0075
76.8664	CH ₃ CHO	44003	4 0 4 2 – 3 0 3 2	9.33	1.43×10^{-5}	1.3371	0.1279	6.4333	0.0627	0.0362	0.0032	0.0515	0.0067
76.8790	CH ₃ CHO	44003	4 0 4 0 – 3 0 3 0	9.23	1.43×10^{-5}	1.2377	0.0904	6.4153	0.0501	0.0424	0.0029	0.0558	0.0056
79.0993	CH ₃ CHO	44003	4 1 3 2 – 3 1 2 2	11.84	1.46×10^{-5}	1.1188	0.2526	6.5718	0.0575	0.0332	0.0057	0.0396	0.0112
79.1502	CH ₃ CHO	44003	4 1 3 0 – 3 1 2 0	11.77	1.46×10^{-5}	1.0519	0.1278	6.4254	0.0829	0.0316	0.0035	0.0354	0.0058
84.2197	CH ₃ CHO	44003	2 1 2 0 – 1 0 1 0	4.97	2.29×10^{-6}	1.423	0.3788	6.2571	0.1506	0.0158	0.0035	0.0239	0.0083
93.5809	CH ₃ CHO	44003	5 1 5 0 – 4 1 4 0	15.75	2.53×10^{-5}	1.8535	0.1954	6.499	0.082	0.0214	0.0019	0.0422	0.0058
93.5952	CH ₃ CHO	44003	5 1 5 1 – 4 1 4 1	15.82	2.53×10^{-5}	1.1006	0.1412	6.4147	0.0499	0.0301	0.0031	0.0353	0.0058
95.9474	CH ₃ CHO	44003	5 0 5 2 – 4 0 4 2	13.93	2.84×10^{-5}	1.2807	0.1128	6.4389	0.047	0.0348	0.0026	0.0474	0.0055
95.9635	CH ₃ CHO	44003	5 0 5 0 – 4 0 4 0	13.84	2.84×10^{-5}	1.1867	0.0964	6.5602	0.0434	0.0407	0.0029	0.0514	0.0056
96.4755	CH ₃ CHO	44003	5 2 3 2 – 4 2 2 2	23.03	2.42×10^{-5}	1.197	0.3932	6.6653	0.166	0.0098	0.0028	0.0124	0.0054
98.8633	CH ₃ CHO	44003	5 1 4 2 – 4 1 3 2	16.59	2.99×10^{-5}	1.4082	0.1608	6.5003	0.0675	0.027	0.0026	0.0404	0.006
98.9009	CH ₃ CHO	44003	5 1 4 0 – 4 1 3 0	16.51	2.99×10^{-5}	1.2267	0.1355	6.5312	0.056	0.0316	0.003	0.0413	0.006
112.2487	CH ₃ CHO	44003	6 1 6 0 – 5 1 5 0	21.13	4.50×10^{-5}	1.8832	0.3689	6.3961	0.1546	0.0208	0.0035	0.0417	0.0108
112.2545	CH ₃ CHO	44003	6 1 6 1 – 5 1 5 1	21.21	4.50×10^{-5}	1.1437	0.1703	6.387	0.0724	0.0298	0.0038	0.0362	0.0071
114.9402	CH ₃ CHO	44003	6 0 6 2 – 5 0 5 2	19.45	4.96×10^{-5}	0.7321	0.3397	6.5147	0.0822	0.0399	0.0145	0.0311	0.0183
114.9599	CH ₃ CHO	44003	6 0 6 0 – 5 0 5 0	19.35	4.96×10^{-5}	1.0368	0.2658	6.6066	0.1104	0.0337	0.0073	0.0371	0.0125
138.3196	CH ₃ CHO	44003	7 1 6 0 – 6 1 5 0	28.84	8.57×10^{-5}	0.5861	0.1884	6.5323	0.1285	0.0293	0.0086	0.0183	0.008
152.6352	CH ₃ CHO	44003	8 0 8 0 – 7 0 7 0	33.1	1.18×10^{-4}	1.5166	0.2852	6.4495	0.1199	0.0202	0.0033	0.0326	0.0081
157.9377	CH ₃ CHO	44003	8 1 7 2 – 7 1 6 2	36.5	1.29×10^{-4}	1.0816	0.2662	6.3254	0.1122	0.0205	0.0044	0.0236	0.0077
157.9746	CH ₃ CHO	44003	8 1 7 0 – 7 1 6 0	36.43	1.29×10^{-4}	0.8319	0.1868	6.2525	0.0774	0.0252	0.0048	0.0223	0.0066
155.1796	CH ₃ CHO	44003	8 2 6 2 – 7 2 5 2	42.54	1.15×10^{-4}	1.0616	0.2489	6.6811	0.1044	0.0167	0.0034	0.0188	0.0058
73.5888	CH ₃ CN	41505	4 1 0 – 3 1 0	15.98	2.97×10^{-5}	1.255	0.4118	6.6026	0.1145	0.0248	0.0063	0.0331	0.0139
73.5902	CH ₃ CN	41505	4 0 0 – 3 0 0	8.83	3.17×10^{-5}	1.3024	0.245	6.5942	0.1215	0.0275	0.0047	0.0382	0.0097
91.9853	CH ₃ CN	41505	5 1 0 – 4 1 0	20.39	6.08×10^{-5}	1.7293	0.4405	6.3258	0.1794	0.0184	0.0039	0.0339	0.0112
91.9871	CH ₃ CN	41505	5 0 0 – 4 0 0	13.24	6.33×10^{-5}	1.6638	0.2834	6.4258	0.1147	0.0225	0.0032	0.0398	0.0088
110.3495	CH ₃ CN	41505	6 4 0 – 5 4 0	132.84	6.17×10^{-5}	2.4912	0.505	7.7082	0.2024	0.0141	0.0024	0.0373	0.0099
110.3750	CH ₃ CN	41505	6 2 0 – 5 2 0	47.12	9.88×10^{-5}	2.228	0.6668	6.3926	0.2537	0.0144	0.0034	0.0341	0.013
110.3814	CH ₃ CN	41505	6 1 0 – 5 1 0	25.69	1.08×10^{-4}	1.839	0.1973	6.2802	0.0789	0.0287	0.0026	0.0562	0.0079
110.3835	CH ₃ CN	41505	6 0 0 – 5 0 0	18.54	1.11×10^{-4}	1.1025	0.0903	6.5178	0.0389	0.0381	0.0027	0.0447	0.0048
153.0545	CH ₃ OCH ₃	46514	9 0 9 0 – 8 1 8 0	40.4	2.19×10^{-5}	3.3104	0.6838	7.0347	0.303	0.0123	0.0021	0.0433	0.0116
153.0548	CH ₃ OCH ₃	46514	9 0 9 1 – 8 1 8 1	40.4	2.19×10^{-5}	-	-	7.811	0.2893	-	-	-	-
153.0552	CH ₃ OCH ₃	46514	9 0 9 5 – 8 1 8 5	40.4	2.19×10^{-5}	-	-	8.4934	0.2764	-	-	-	-
153.0552	CH ₃ OCH ₃	46514	9 0 9 3 – 8 1 8 3	40.4	2.19×10^{-5}	-	-	8.4919	0.2591	-	-	-	-
89.3147	CH ₃ OCHO	60003	8 1 8 1 – 7 1 7 1	20.15	1.02×10^{-5}	1.5752	0.3643	6.4413	0.148	0.0133	0.0026	0.0224	0.0068
153.3505	CH ₃ OCHO	60003	14 1 1 4 1 – 1 3 1 1 3 1	56.65	5.33×10^{-5}	2.7886	0.4848	5.8803	0.1751	0.0148	0.0019	0.044	0.0095
153.5669	CH ₃ OCHO	60003	12 2 1 0 0 – 1 1 2 9 0	50.6	5.20×10^{-5}	1.4377	0.3819	6.8991	0.1606	0.0138	0.0032	0.0211	0.0074
84.5212	CH ₃ OH	32504	5 1 5 2 – 4 0 4 1	40.39	1.97×10^{-6}	1.278	0.1042	6.4633	0.0373	0.0572	0.0038	0.0778	0.0082
94.5418	CH ₃ OH	32504	8 3 6 1 – 9 2 8 1	131.28	4.0369	0.7429	8.459	0.2805	0.0114	0.0016	0.0489	0.0113	
95.1694	CH ₃ OH	32504	8 0 8 0 – 7 1 7 0	83.54	4.26×10^{-6}	1.6796	0.6316	6.3249	0.2764	0.0135	0.0031	0.0242	0.0107

Table A.1 continued

Freq. (GHz)	Species	Tag	Transition	E_{up} (K)	A_{ij} (s $^{-1}$)	FWHM (km s $^{-1}$)	δFWHM (km s $^{-1}$)	v (km s $^{-1}$)	δv (km s $^{-1}$)	Int (K)	δInt (K)	Flux (K km s $^{-1}$)	δFlux (K km s $^{-1}$)
95.1694	CH ₃ OH	32504	8 0 8 0 -7 1 7 0	83.54	4.26×10^{-6}	1.9195	0.5794	8.6619	0.2414	0.0166	0.0029	0.0338	0.0118
95.9143	CH ₃ OH	32504	2 1 2 0 -1 1 1 0	21.44	2.49×10^{-6}	2.1029	0.4435	6.796	0.1746	0.0116	0.0027	0.0358	0.0097
96.7394	CH ₃ OH	32504	2 1 2 2 -1 1 1 2	12.54	2.56×10^{-6}	1.4417	0.0176	6.4812	0.0074	0.4258	0.0045	0.6534	0.0106
96.7414	CH ₃ OH	32504	2 0 2 0 -1 0 1 0	6.96	3.41×10^{-6}	1.3988	0.0129	6.4799	0.0054	0.6276	0.0049	0.9345	0.0113
96.7445	CH ₃ OH	32504	2 0 2 1 -1 0 1 1	20.09	3.41×10^{-6}	1.317	0.0563	6.4526	0.0229	0.0864	0.0031	0.1211	0.0068
96.7555	CH ₃ OH	32504	2 1 1 1 -1 1 0 1	28.01	2.62×10^{-6}	1.046	0.1709	6.287	0.0839	0.0218	0.0031	0.0243	0.0053
96.7555	CH ₃ OH	32504	2 1 1 1 -1 1 0 1	28.01	2.62×10^{-6}	1.7604	0.4817	8.6887	0.1928	0.0116	0.0026	0.0218	0.0077
97.5828	CH ₃ OH	32504	2 1 1 0 -1 1 0 0	21.56	2.63×10^{-6}	1.5505	0.2676	6.5068	0.1144	0.0187	0.002	0.0309	0.0063
97.5828	CH ₃ OH	32504	2 1 1 0 -1 1 0 0	21.56	2.63×10^{-6}	1.6823	0.3793	8.6488	0.1576	0.0141	0.0019	0.0253	0.0066
100.6389	CH ₃ OH	32504	13 2 1 2 1 -1 2 3 1 0 1	233.61	1.69×10^{-6}	3.6015	0.539	8.5786	0.2217	0.0146	0.0019	0.0561	0.0111
104.3003	CH ₃ OH	32504	11 1 1 1 2 -1 0 2 8 2	158.64	1.96×10^{-6}	2.9646	0.562	7.9621	0.2298	0.0123	0.002	0.0389	0.0097
105.0638	CH ₃ OH	32504	13 1 1 3 0 -1 2 2 1 0 0	223.84	2.14×10^{-6}	1.8809	0.3906	9.2711	0.1629	0.0129	0.0023	0.0258	0.0071
107.0138	CH ₃ OH	32504	3 1 3 0 -4 0 4 0	28.35	6.13×10^{-6}	1.6022	0.2005	8.8474	0.0761	0.0316	0.003	0.0539	0.0085
108.8939	CH ₃ OH	32504	0 0 0 1 -1 1 1 2	13.12	1.47×10^{-5}	1.3011	0.0481	6.4868	0.0201	0.1295	0.0041	0.1794	0.0087
111.2895	CH ₃ OH	32504	7 2 5 0 -8 1 8 0	102.72	2.50×10^{-6}	1.8597	0.4363	8.7488	0.1797	0.0165	0.0033	0.0327	0.0101
145.0938	CH ₃ OH	32504	3 0 3 1 -2 0 2 1	27.05	1.23×10^{-5}	0.9833	0.1343	6.3566	0.0559	0.1216	0.0142	0.1272	0.0229
145.0974	CH ₃ OH	32504	3 1 3 2 -2 1 2 2	19.5	1.10×10^{-5}	1.2081	0.0314	6.4486	0.013	0.557	0.0123	0.7163	0.0244
145.1032	CH ₃ OH	32504	3 0 3 0 -2 0 2 0	13.93	1.23×10^{-5}	1.2071	0.0293	6.4623	0.0123	0.7324	0.0152	0.941	0.0301
145.1319	CH ₃ OH	32504	3 1 2 1 -2 1 1 1	34.98	1.12×10^{-5}	3.1744	0.7154	6.1457	0.2659	0.0534	0.0086	0.1805	0.05
146.3683	CH ₃ OH	32504	3 1 2 0 -2 1 1 0	28.59	1.13×10^{-5}	0.6479	0.2077	6.3389	0.0633	0.0895	0.0224	0.0617	0.0251
146.3683	CH ₃ OH	32504	3 1 2 0 -2 1 1 0	28.59	1.13×10^{-5}	0.907	0.2392	8.6457	0.1015	0.0685	0.0156	0.0662	0.0231
151.8602	CH ₃ OH	32504	13 0 1 3 1 -1 3 1 3 2	223.82	1.15×10^{-5}	1.8062	0.2233	8.9578	0.0865	0.0277	0.0027	0.0533	0.0084
152.7084	CH ₃ OH	32504	9 4 6 0 -1 0 3 7 0	184.79	4.48×10^{-6}	2.4606	0.6826	8.6699	0.2392	0.0171	0.0027	0.0448	0.0143
152.7402	CH ₃ OH	32504	9 4 5 0 -1 0 3 8 0	184.79	4.49×10^{-6}	0.9738	0.2596	8.4836	0.1077	0.0184	0.0042	0.0191	0.0067
153.2813	CH ₃ OH	32504	12 0 1 2 1 -1 2 1 1 2 2	193.79	1.29×10^{-5}	2.6892	0.7247	8.9259	0.2971	0.0208	0.0029	0.0597	0.0181
154.4258	CH ₃ OH	32504	11 0 1 1 1 -1 1 1 1 2	166.05	1.42×10^{-5}	2.0787	0.2384	8.7923	0.091	0.0319	0.0029	0.0706	0.0103
155.3209	CH ₃ OH	32504	10 0 1 0 1 -1 0 1 1 0 2	140.6	1.55×10^{-5}	1.9098	0.2043	8.6898	0.0801	0.0341	0.0029	0.0693	0.0095
155.9975	CH ₃ OH	32504	9 0 9 1 -9 1 9 2	117.46	1.67×10^{-5}	2.069	0.1942	8.7841	0.0779	0.0379	0.0029	0.0835	0.0101
156.6024	CH ₃ OH	32504	2 1 2 0 -3 0 3 0	21.44	1.78×10^{-5}	1.1173	0.1601	8.518	0.0673	0.0308	0.0038	0.0366	0.0069
156.1275	CH ₃ OH	32504	6 2 4 0 -7 1 7 0	86.46	6.54×10^{-6}	2.1708	0.3712	8.4346	0.1395	0.0246	0.0027	0.0568	0.0115
156.4889	CH ₃ OH	32504	8 0 8 1 -8 1 8 2	96.61	1.78×10^{-5}	2.0427	0.1998	8.7727	0.0763	0.0402	0.003	0.0874	0.0108
156.6024	CH ₃ OH	32504	2 1 2 0 -3 0 3 0	21.44	1.78×10^{-5}	0.6174	0.1621	6.2949	0.0567	0.027	0.0057	0.0178	0.006
157.0486	CH ₃ OH	32504	2 1 2 0 -3 0 3 0	21.44	1.78×10^{-5}	1.1173	0.1601	8.518	0.0673	0.0308	0.0038	0.0366	0.0069
157.8285	CH ₃ OH	32504	7 0 7 1 -7 1 7 2	78.08	1.88×10^{-5}	0.8415	0.1782	6.3842	0.0738	0.0236	0.004	0.0212	0.0058
156.8285	CH ₃ OH	32504	7 0 7 1 -7 1 7 2	78.08	1.88×10^{-5}	2.4047	0.1986	8.749	0.0754	0.04	0.0024	0.1023	0.0104
157.1779	CH ₃ OH	32504	5 0 5 1 -5 1 5 2	47.93	2.04×10^{-5}	1.0048	0.1186	6.3229	0.0492	0.0521	0.0049	0.0557	0.0084
157.1779	CH ₃ OH	32504	5 0 5 1 -5 1 5 2	47.93	2.04×10^{-5}	2.2727	0.3501	8.3321	0.1238	0.0351	0.003	0.085	0.015
157.2461	CH ₃ OH	32504	4 0 4 1 -4 1 4 2	36.34	2.10×10^{-5}	0.8993	0.0518	6.3326	0.0217	0.0922	0.0042	0.0883	0.0065
157.2461	CH ₃ OH	32504	4 0 4 1 -4 1 4 2	36.34	2.10×10^{-5}	2.1178	0.1916	8.5815	0.0731	0.042	0.0028	0.0946	0.0106

Table A.1 continued

Freq. (GHz)	Species	Tag	Transition	E_{up} (K)	A_{ij} (s $^{-1}$)	FWHM (km s $^{-1}$)	δFWHM (km s $^{-1}$)	v (km s $^{-1}$)	δv (km s $^{-1}$)	Int (K)	δInt (K)	Flux (K km s $^{-1}$)	δFlux (K km s $^{-1}$)
157.2708	CH ₃ OH	32504	1 0 1 1 - 1 1 1 2	15.45	2.20×10^{-5}	1.2991	0.0292	6.4125	0.0122	0.2547	0.0049	0.3523	0.0104
157.2723	CH ₃ OH	32504	3 0 3 1 - 3 1 3 2	27.05	2.15×10^{-5}	0.9431	0.0377	6.3858	0.0158	0.148	0.0051	0.1485	0.0078
157.276	CH ₃ OH	32504	2 0 2 1 - 2 1 2 2	20.09	2.18×10^{-5}	0.9602	0.0261	6.4298	0.0109	0.2121	0.0049	0.2168	0.0077
86.6688	CH ₂ DOH	33004	2 1 1 0 - 2 0 2 0	10.6	4.65×10^{-6}	1.1537	0.382	6.0873	0.1765	0.0113	0.0033	0.0138	0.0061
88.7545	CH ₂ DOH	33004	3 1 2 0 - 3 0 3 0	17.13	4.92×10^{-6}	1.6206	0.5949	6.0325	0.25	0.0087	0.0027	0.0115	0.0072
88.7545	CH ₂ DOH	33004	3 1 2 0 - 3 0 3 0	17.13	4.92×10^{-6}	0.779	0.349	9.3577	0.2253	0.0125	0.0042	0.0103	0.0058
89.4078	CH ₂ DOH	33004	2 0 2 0 - 1 0 1 0	6.44	2.02×10^{-6}	0.9365	0.1038	6.1154	0.0669	0.0263	0.0027	0.0262	0.004
90.7798	CH ₂ DOH	33004	2 1 1 0 - 1 1 0 0	10.6	1.57×10^{-6}	0.7163	0.422	6.1519	0.3039	0.0107	0.0044	0.0081	0.0058
91.5868	CH ₂ DOH	33004	4 1 3 0 - 4 0 4 0	25.84	5.29×10^{-6}	1.5932	0.6149	5.9797	0.2332	0.0093	0.0027	0.0157	0.0076
91.5868	CH ₂ DOH	33004	4 1 3 0 - 4 0 4 0	25.84	5.29×10^{-6}	0.9043	0.3094	9.3472	0.1586	0.0119	0.0034	0.0115	0.0051
113.1234	CN	26504	1 0 0 5 0 5 - 0 0 5 0 5	5.43	1.29×10^{-6}	0.9753	0.0145	6.5106	0.0062	0.3937	0.0051	0.4087	0.0081
113.1442	CN	26504	1 0 0 5 0 5 - 0 0 5 1 5	5.43	1.05×10^{-5}	1.0362	0.0156	6.5171	0.0063	1.3711	0.0175	1.5124	0.0299
113.1705	CN	26504	1 0 0 5 1 5 - 0 0 5 0 5	5.43	5.14×10^{-6}	1.0699	0.0156	6.4502	0.0063	1.3249	0.0164	1.5088	0.0289
113.1913	CN	26504	1 0 0 5 1 5 - 0 0 5 1 5	5.43	6.68×10^{-6}	1.2195	0.0087	6.5014	0.0037	1.2796	0.0079	1.6611	0.0157
113.4881	CN	26504	1 0 1 5 1 5 - 0 0 5 0 5	5.45	6.74×10^{-6}	1.1292	0.0134	6.5186	0.0057	1.3525	0.0139	1.6258	0.0255
113.4910	CN	26504	1 0 1 5 2 5 - 0 0 5 1 5	5.45	1.19×10^{-5}	1.6165	0.0462	6.6222	0.0193	1.4289	0.035	2.4587	0.0925
113.4996	CN	26504	1 0 1 5 0 5 - 0 0 5 0 5	5.45	1.06×10^{-5}	1.0571	0.0144	6.5336	0.006	1.2265	0.0144	1.3801	0.0248
113.5089	CN	26504	1 0 1 5 1 5 - 0 0 5 1 5	5.45	5.19×10^{-6}	1.1696	0.0141	6.5088	0.006	1.3	0.0136	1.6185	0.0258
113.5204	CN	26504	1 0 1 5 0 5 - 0 0 5 1 5	5.45	1.30×10^{-6}	0.9769	0.0148	6.5762	0.0068	0.3828	0.0052	0.398	0.0081
108.4129	¹³ CN	27505	1 0 5 0 1 - 0 5 1 1	5.23	3.14×10^{-6}	0.6	0.3362	6.4727	0.2293	0.0149	0.0061	0.0095	0.0066
108.4269	¹³ CN	27505	1 0 5 0 1 - 0 5 1 2	5.23	6.27×10^{-6}	1.0888	0.1526	6.4242	0.0683	0.0281	0.0035	0.0326	0.0061
108.6311	¹³ CN	27505	1 0 5 1 0 - 0 5 0 1	5.21	9.58×10^{-6}	0.8704	0.4786	6.524	0.1355	0.02	0.0085	0.0185	0.0129
108.6369	¹³ CN	27505	1 0 5 1 1 - 0 5 0 1	5.21	9.61×10^{-6}	0.7891	0.2192	6.4745	0.0661	0.041	0.009	0.0344	0.0122
108.6382	¹³ CN	27505	1 1 5 1 1 - 0 5 1 0	5.24	3.59×10^{-6}	0.8052	0.332	6.5093	0.1889	0.0187	0.007	0.016	0.0089
108.6436	¹³ CN	27505	1 1 5 1 2 - 0 5 1 1	5.24	2.56×10^{-6}	0.9111	0.7578	6.3187	0.3332	0.0149	0.0107	0.0145	0.0159
108.6443	¹³ CN	27505	1 1 5 1 0 - 0 5 1 1	5.24	9.58×10^{-6}	1.3329	0.4169	6.3607	0.1591	0.0135	0.0034	0.0191	0.0077
108.6451	¹³ CN	27505	1 1 5 1 1 - 0 5 1 1	5.24	2.74×10^{-6}	0.7289	0.6121	6.9352	0.3309	0.0175	0.0121	0.0135	0.0147
108.6513	¹³ CN	27505	1 0 5 1 2 - 0 5 0 1	5.21	9.78×10^{-6}	1.003	0.1229	6.54	0.055	0.0682	0.0074	0.0729	0.0119
108.6576	¹³ CN	27505	1 1 5 1 2 - 0 5 1 2	5.24	7.23×10^{-6}	0.9159	0.2634	6.5474	0.0994	0.0444	0.0105	0.0433	0.0161
108.6589	¹³ CN	27505	1 1 5 1 1 - 0 5 1 2	5.24	3.33×10^{-6}	0.856	0.5159	6.5619	0.2923	0.0176	0.01	0.016	0.0133
108.7802	¹³ CN	27505	1 1 5 2 3 - 0 5 1 2	5.25	1.05×10^{-5}	0.9486	0.0951	6.5336	0.0442	0.0992	0.0089	0.1002	0.0135
108.7824	¹³ CN	27505	1 1 5 2 2 - 0 5 1 1	5.25	7.75×10^{-6}	0.9642	0.2041	6.4883	0.1007	0.0608	0.0118	0.0624	0.0179
108.7870	¹³ CN	27505	1 1 5 2 1 - 0 5 1 0	5.25	5.72×10^{-6}	0.8527	0.7044	6.4887	0.2265	0.0279	0.0182	0.0254	0.0267
108.7964	¹³ CN	27505	1 1 5 2 2 - 0 5 1 2	5.25	2.75×10^{-6}	0.9409	0.2911	6.5075	0.1343	0.0196	0.0054	0.0468	0.0067
109.6896	C ¹⁵ N	27506	1 0 5 1 - 0 5 1	5.27	7.10×10^{-6}	2.186	0.3771	6.3965	0.1578	0.0167	0.0025	0.0387	0.0088
110.0235	C ¹⁵ N	27506	1 1 5 1 - 0 5 0	5.28	7.16×10^{-6}	1.5393	0.3334	6.4387	0.1364	0.0159	0.0029	0.0261	0.0074
110.0246	C ¹⁵ N	27506	1 1 5 2 - 0 5 1	5.28	1.09×10^{-5}	1.2789	0.1386	6.4818	0.0582	0.0344	0.0032	0.0468	0.0081
115.2712	CO	28503	1 - 0	5.53	7.20×10^{-8}	4.4482	0.0697	6.1208	0.0285	9.6441	0.1276	45.6646	0.9365
110.2014	¹³ CO	29501	1 - 0	5.29	6.33×10^{-8}	1.7909	0.0193	6.3648	0.0081	7.6232	0.0707	14.5322	0.2066
112.3588	C ¹⁷ O	29503	1 1.5 - 0 2.5	5.39	6.70×10^{-8}	1.305	0.0222	5.9325	0.0093	0.5985	0.0087	0.8314	0.0186

Table A.1 continued

Freq. (GHz)	Species	Tag	Transition	E_{up} (K)	A_{ij} (s $^{-1}$)	FWHM (km s $^{-1}$)	δFWHM (km s $^{-1}$)	v (km s $^{-1}$)	δ_v (km s $^{-1}$)	Int (K)	δInt (K)	Flux (K km s $^{-1}$)	δFlux (K km s $^{-1}$)
112.359	C 17 O	29503	1 3.5 - 0 2.5	5.39	6.70×10^{-8}	-	6.4795	0.0093	-	-	-	-	-
112.36	C 17 O	29503	1 2.5 - 0 2.5	5.39	6.70×10^{-8}	0.9913	0.0312	6.3496	0.0145	0.3744	0.0106	0.3951	0.0167
109.7822	C 18 O	30502	1 - 0	5.27	6.27×10^{-8}	1.1511	0.0143	6.3523	0.0059	3.1462	0.0333	3.8552	0.0629
104.7114	$^{13}\text{C}^{18}\text{O}$	31502	1 0.5 - 0 0.5	5.03	5.45×10^{-8}	1.0402	0.0713	6.3889	0.03	0.0571	0.0034	0.0632	0.0057
97.981	CS	44501	2 0 - 1 0	7.05	1.68×10^{-5}	1.5431	0.0265	6.6987	0.0111	2.4843	0.0366	4.0806	0.0923
146.969	CS	44501	3 0 - 2 0	14.11	6.07×10^{-5}	1.2504	0.0237	6.7168	0.01	2.99	0.0488	3.9797	0.0995
92.4943	^{13}CS	45501	2 0 - 1 0	6.66	1.41×10^{-5}	1.1264	0.0374	6.8505	0.017	0.0814	0.0024	0.0976	0.0043
138.7393	^{13}CS	45501	3 0 - 2 0	13.32	5.11×10^{-5}	1.0073	0.1372	6.8162	0.0538	0.0606	0.0068	0.0649	0.0115
97.1721	C 33 S	45502	2 0 - 1 0	7.0	1.64×10^{-5}	1.3763	0.1622	7.3976	0.069	0.0306	0.0031	0.0448	0.007
96.4129	C 34 S	46501	2 0 - 1 0	6.94	1.60×10^{-5}	1.2175	0.0304	6.6883	0.0123	0.2301	0.0048	0.2983	0.0097
144.6171	C 34 S	46501	3 0 - 2 0	13.88	5.78×10^{-5}	1.3348	0.0678	6.6382	0.0283	0.2405	0.0105	0.3417	0.0229
88.6304	HCN	27601	1 1 - 0 1	4.25	2.41×10^{-5}	1.3596	0.0133	6.4677	0.0057	1.2644	0.0108	1.8299	0.0238
88.6318	HCN	27601	1 2 - 0 1	4.25	2.41×10^{-5}	1.4178	0.0321	6.4611	0.013	1.6185	0.0308	2.4426	0.0722
88.6339	HCN	27601	1 0 - 0 1	4.25	2.41×10^{-5}	1.1017	0.0085	6.427	0.0037	1.1343	0.0075	1.3303	0.0135
72.4135	DCN	28509	1 0 0 1 - 0 0 0 1	3.48	1.31×10^{-5}	0.9917	0.0468	6.3174	0.0252	0.1953	0.0072	0.2062	0.0123
72.4149	DCN	28509	1 0 0 2 - 0 0 0 1	3.48	1.31×10^{-5}	1.0128	0.0848	6.2813	0.011	0.322	0.0239	0.3471	0.0388
72.417	DCN	28509	1 0 0 0 - 0 0 0 1	3.48	1.31×10^{-5}	0.9924	0.0916	6.3741	0.0537	0.0681	0.0049	0.072	0.0084
144.8266	DCN	28509	2 0 0 2 - 1 0 0 2	10.45	3.16×10^{-5}	1.0128	-	6.0273	0.047	0.1286	0.0122	0.1386	0.0202
144.8268	DCN	28509	2 0 0 1 - 1 0 0 0	10.45	7.01×10^{-5}	-	-	-	-	-	-	-	-
144.8228	DCN	28509	2 0 0 2 - 1 0 0 1	10.45	9.46×10^{-5}	1.041	0.0335	6.1564	0.0141	0.4704	0.013	0.5212	0.0221
144.8281	DCN	28509	2 0 0 3 - 1 0 0 2	10.45	1.26×10^{-4}	-	-	-	-	-	-	-	-
144.8303	DCN	28509	2 0 0 1 - 1 0 0 1	10.45	5.26×10^{-5}	1.3024	0.3456	6.3186	0.145	0.0491	0.0112	0.0681	0.0238
86.3387	H 13 CN	28002	1 1 - 0 1	4.14	2.22×10^{-5}	0.9649	0.0529	6.3653	0.018	0.113	0.0049	0.1161	0.0081
86.3402	H 13 CN	28002	1 2 - 0 1	4.14	2.22×10^{-5}	0.9444	0.0183	6.3994	0.0121	0.1765	0.0031	0.1774	0.0046
86.3423	H 13 CN	28002	1 0 - 0 1	4.14	2.22×10^{-5}	1.049	0.1071	6.2965	0.0507	0.0384	0.0034	0.0429	0.0058
86.055	HC 15 N	28506	1 - 0	4.13	2.20×10^{-5}	0.9428	0.0574	6.3787	0.0252	0.0768	0.0038	0.0771	0.006
90.6636	HNC	27502	1 0 0 - 0 0 0	4.35	2.69×10^{-5}	1.4285	0.0186	6.4424	0.0079	3.9207	0.0442	5.9618	0.1027
76.3057	DNC	28508	1 - 0	3.66	1.60×10^{-5}	1.2192	0.0066	6.3053	0.0038	0.6352	0.0033	0.8244	0.0062
152.6097	DNC	28508	2 - 1	10.99	1.54×10^{-4}	0.8188	0.0072	6.211	0.003	0.9612	0.0073	0.8377	0.0097
87.0908	H N^{13}C	28515	1 - 0	4.18	2.38×10^{-5}	1.1031	0.0226	6.4151	0.0072	0.3214	0.0052	0.3774	0.0099
88.8657	H ^{15}NC	28006	1 - 0	4.26	1.98×10^{-5}	0.8461	0.034	6.4276	0.0249	0.0815	0.0028	0.0734	0.0039
87.9252	HNCO	43511	4 0 4 - 3 0 3	10.55	8.78×10^{-6}	0.8916	0.0992	6.4079	0.0292	0.082	0.0074	0.0778	0.0111
109.9057	HNCO	43511	5 0 5 - 4 0 4	15.82	1.75×10^{-5}	0.9643	0.0575	6.3283	0.0273	0.0767	0.0041	0.0788	0.0063
153.8651	HNCO	43511	7 0 7 - 6 0 6	29.54	4.94×10^{-5}	1.0906	0.0877	6.2855	0.037	0.0637	0.0044	0.0739	0.0078
86.6708	HCO	29004	1 0 1 1.5 2 - 0 0 0 0.5 1	4.18	4.69×10^{-6}	1.1674	0.0552	6.6994	0.0249	0.0796	0.0033	0.0989	0.0062
86.7084	HCO	29004	1 0 1 1.5 1 - 0 0 0 0.5 0	4.16	4.60×10^{-6}	1.3098	0.0799	6.796	0.0307	0.0565	0.0029	0.0788	0.0063
86.7775	HCO	29004	1 0 1 0.5 1 - 0 0 0 0.5 1	4.18	4.61×10^{-6}	1.4258	0.1218	6.6627	0.0494	0.0429	0.0031	0.065	0.0073
86.8058	HCO	29004	1 0 1 0.5 0 - 0 0 0 0.5 1	4.18	4.71×10^{-6}	1.119	0.3272	6.7118	0.096	0.0187	0.0042	0.0223	0.0082
89.1885	HCO $^+$	29507	1 - 0	4.28	4.19×10^{-5}	1.9361	0.0239	6.6458	0.01	3.4334	0.0364	7.0759	0.1151
72.0393	DCO $^+$	30510	1 - 0	3.46	2.21×10^{-5}	1.0109	0.0044	6.4304	0.029	1.3335	0.0046	1.435	0.008

Table A.1 continued

Freq. (GHz)	Species	Tag	Transition	E_{up} (K)	A_{ij} (s $^{-1}$)	FWHM (km s $^{-1}$)	δFWHM (km s $^{-1}$)	v (km s $^{-1}$)	δv (km s $^{-1}$)	Int (K)	δInt (K)	Flux (K km s $^{-1}$)	δFlux (K km s $^{-1}$)
144.0773	DCO $^+$	30510	2 - 1	10.37	2.12×10^{-4}	0.8829	0.0082	6.3531	0.0036	2.0437	0.0166	1.9206	0.0237
86.7543	H 13 CO $^+$	30504	1 - 0	4.16	3.85×10^{-5}	1.0178	0.0029	6.4251	0.0011	2.1066	0.0048	2.2824	0.0083
85.1622	HC 18 O $^+$	31506	1 - 0	4.09	3.64×10^{-5}	0.8862	0.0192	6.3814	0.011	0.2181	0.0038	0.2058	0.0057
87.0575	HC 17 O $^+$	30505	1 - 0	4.18	3.89×10^{-5}	1.398	0.2885	7.4925	0.1179	0.0201	0.0035	0.03	0.0081
141.4651	D 13 CO $^+$	31508	2 - 1	10.18	2.00×10^{-4}	0.7108	0.0848	6.2895	0.0441	0.077	0.0086	0.0582	0.0095
72.7838	HC $_3$ N	51501	8 - 7	15.72	2.94×10^{-5}	1.0714	0.0053	6.5523	0.0038	0.8467	0.0037	0.9656	0.0064
81.8815	HC $_3$ N	51501	9 - 8	19.65	4.21×10^{-5}	1.0834	0.0159	6.49	0.0047	0.7053	0.0081	0.8133	0.0152
90.979	HC $_3$ N	51501	10 - 9	24.01	5.81×10^{-5}	0.9894	0.0055	6.5835	0.0033	0.8446	0.0045	0.8895	0.0068
100.0764	HC $_3$ N	51501	11 - 10	28.82	7.77×10^{-5}	1.002	0.0167	6.4029	0.0055	0.8084	0.0107	0.8622	0.0184
109.1736	HC $_3$ N	51501	12 - 11	34.06	1.01×10^{-4}	1.0776	0.0119	6.4035	0.0047	0.6568	0.0061	0.7534	0.0109
136.4644	HC $_3$ N	51501	15 - 14	52.4	1.99×10^{-4}	1.0688	0.0313	6.4055	0.0132	0.3487	0.0088	0.3967	0.0153
145.561	HC $_3$ N	51501	16 - 15	59.38	2.42×10^{-4}	1.1277	0.0522	6.4151	0.022	0.3737	0.0149	0.4486	0.0274
154.6573	HC $_3$ N	51501	17 - 16	66.8	2.91×10^{-4}	1.1345	0.022	6.3906	0.0092	0.3674	0.0061	0.4436	0.0113
75.9871	DC $_3$ N	52508	9 - 8	18.23	3.39×10^{-5}	1.0319	0.1665	6.3182	0.1042	0.0259	0.0035	0.0284	0.0006
84.4298	DC $_3$ N	52508	10 - 9	22.29	4.67×10^{-5}	0.9814	0.1458	6.3564	0.0848	0.0257	0.0033	0.0269	0.0053
92.8724	DC $_3$ N	52508	11 - 10	26.74	6.24×10^{-5}	1.2468	0.2526	6.4446	0.0979	0.0164	0.0028	0.0218	0.0058
101.3148	DC $_3$ N	52508	12 - 11	31.61	8.13×10^{-5}	1.3387	0.235	6.4093	0.0979	0.0188	0.0028	0.0267	0.0061
109.7571	DC $_3$ N	52508	13 - 12	36.87	1.04×10^{-4}	1.2234	0.2253	6.3567	0.0956	0.018	0.0029	0.0234	0.0057
79.3505	H 13 CCCN	52509	9 - 8	19.04	3.84×10^{-5}	1.4118	0.3402	6.7187	0.1472	0.016	0.0034	0.0241	0.0077
88.1668	H 13 CCCN	52509	10 - 9	23.27	5.29×10^{-5}	1.2918	0.274	6.847	0.1257	0.0147	0.0028	0.0203	0.0058
90.5931	HC 13 CCN	52510	10 - 9	23.91	5.74×10^{-5}	0.8386	0.3068	6.32	0.1206	0.0191	0.0056	0.017	0.008
108.7105	HC 13 CCN	52510	12 - 11	33.91	1.00×10^{-4}	1.6973	0.401	6.7207	0.167	0.0154	0.0031	0.0279	0.0087
72.4821	HCC 13 CN	52511	8 - 7	15.65	2.90×10^{-5}	1.0073	0.3037	6.5908	0.1877	0.0199	0.0047	0.0213	0.0082
81.542	HCC 13 CN	52511	9 - 8	19.57	4.16×10^{-5}	1.0852	0.4153	6.1925	0.2316	0.0147	0.0051	0.017	0.0088
90.6018	HCC 13 CN	52511	10 - 9	23.92	5.74×10^{-5}	0.7743	0.4046	6.4472	0.1556	0.0189	0.0085	0.0156	0.0108
99.6615	HCC 13 CN	52511	11 - 10	28.7	7.67×10^{-5}	1.2975	0.2882	6.412	0.1185	0.0144	0.0027	0.0199	0.0058
71.8896	HC $_3$ N	75503	27 - 26	48.3	3.98×10^{-5}	1.2435	0.2942	6.3641	0.0858	0.0338	0.0062	0.0448	0.0134
74.5520	HC $_3$ N	75503	28 - 27	51.88	4.44×10^{-5}	1.3301	0.1763	6.3597	0.0568	0.0365	0.0038	0.0516	0.0087
77.2144	HC $_3$ N	75503	29 - 28	55.59	4.94×10^{-5}	1.0055	0.5181	6.4037	0.1255	0.0356	0.0151	0.0381	0.0254
79.8767	HC $_3$ N	75503	30 - 29	59.42	5.47×10^{-5}	1.2166	0.5409	6.5644	0.1605	0.0301	0.0103	0.0389	0.0218
82.5390	HC $_3$ N	75503	31 - 30	63.38	6.04×10^{-5}	1.0136	0.3168	6.4606	0.088	0.0361	0.0089	0.0389	0.0155
85.2013	HC $_3$ N	75503	32 - 31	67.47	6.64×10^{-5}	1.0232	0.1158	6.3626	0.0633	0.0342	0.0034	0.0372	0.0056
87.8636	HC $_3$ N	75503	33 - 32	71.69	7.29×10^{-5}	1.0778	0.153	6.4016	0.0662	0.03	0.0036	0.0344	0.0064
90.5259	HC $_3$ N	75503	34 - 33	76.03	7.98×10^{-5}	0.9398	0.0874	6.4881	0.0519	0.031	0.0026	0.031	0.0039
93.1881	HC $_3$ N	75503	35 - 34	80.5	8.71×10^{-5}	1.5446	0.2429	6.4086	0.1022	0.0188	0.0026	0.031	0.0065
95.8503	HC $_3$ N	75503	36 - 35	85.1	9.48×10^{-5}	1.4334	0.3041	6.3352	0.1275	0.015	0.0027	0.023	0.0064
98.5125	HC $_3$ N	75503	37 - 36	89.83	1.03×10^{-4}	1.3221	0.2292	6.4132	0.0966	0.0193	0.0029	0.0271	0.0062
101.1747	HC $_3$ N	75503	38 - 37	94.69	1.12×10^{-4}	1.5524	0.2592	6.321	0.1089	0.0192	0.0028	0.0317	0.007
103.8368	HC $_3$ N	75503	39 - 38	99.67	1.21×10^{-4}	1.2262	0.3389	6.2926	0.1387	0.0151	0.0036	0.0198	0.0072
106.4989	HC $_3$ N	75503	40 - 39	104.78	1.30×10^{-4}	0.7871	0.2165	6.4959	0.0956	0.0184	0.0042	0.0154	0.0055

Table A.1 continued

Freq. (GHz)	Species	Tag	Transition	E_{up} (K)	A_{ij} (s $^{-1}$)	FWHM (km s $^{-1}$)	δFWHM (km s $^{-1}$)	v (km s $^{-1}$)	δv (km s $^{-1}$)	Int (K)	δInt (K)	Flux (K km s $^{-1}$)	δFlux (K km s $^{-1}$)
111.823	HC ₅ N	75503	42-41	115.39	1.51×10^{-4}	0.6287	0.5692	6.5253	0.1695	0.017	0.0139	0.0114	0.0139
72.8379	H ₂ CO	30501	1 0 1 - 0 0 0	3.5	8.15×10^{-6}	1.37	0.0049	6.5274	0.0023	1.845	0.0059	2.6906	0.0129
140.8395	H ₂ CO	30501	2 1 2 - 1 1 1	21.92	5.30×10^{-5}	1.2424	0.0175	6.5256	0.0074	2.5873	0.0314	3.4217	0.0636
145.6029	H ₂ CO	30501	2 0 2 - 1 0 1	10.48	7.81×10^{-5}	1.094	0.0155	6.5035	0.0065	2.4974	0.0305	2.9081	0.0544
110.8378	D ₂ CO	32502	2 1 2 - 1 1 1	13.37	2.58×10^{-5}	0.7804	0.0736	6.3784	0.0231	0.1297	0.0096	0.1077	0.0129
88.8657	H ₂ ¹³ CO	28006	1 - 0	4.26	1.98×10^{-5}	0.8461	0.034	6.4276	0.0249	0.0815	0.0028	0.0734	0.0039
137.45	H ₂ ¹³ CO	31002	2 1 2 - 1 1 1	21.72	4.93×10^{-5}	1.0044	0.0823	6.4142	0.0347	0.1014	0.0072	0.1084	0.0118
141.9837	H ₂ ¹³ CO	31002	2 0 2 - 1 0 1	10.22	7.25×10^{-5}	0.8463	0.1223	6.4364	0.0488	0.0726	0.0088	0.0654	0.0123
146.6357	H ₂ ¹³ CO	31002	2 1 1 - 1 1 0	22.38	5.99×10^{-5}	0.9927	0.1583	6.4326	0.0667	0.106	0.0146	0.112	0.0236
80.8321	H ₂ CCO	42501	4 0 4 - 3 0 3	9.7	5.52×10^{-6}	1.2744	0.4216	6.3262	0.1817	0.0239	0.0068	0.0325	0.0142
80.0767	H ₂ CCO	42501	4 1 4 - 3 1 3	22.66	5.04×10^{-6}	1.4818	0.2949	6.5811	0.1305	0.0311	0.0054	0.049	0.0129
81.5862	H ₂ CCO	42501	4 1 3 - 3 1 2	22.84	5.33×10^{-6}	1.0989	0.1786	6.5079	0.1057	0.0398	0.0061	0.0466	0.0104
100.0945	H ₂ CCO	42501	5 1 5 - 4 1 4	27.46	1.03×10^{-5}	1.2177	0.0933	6.3905	0.0377	0.0514	0.0033	0.0666	0.0067
101.0366	H ₂ CCO	42501	5 0 5 - 4 0 4	14.55	1.10×10^{-5}	1.286	0.1635	6.4647	0.07	0.0278	0.0031	0.038	0.0064
101.9814	H ₂ CCO	42501	5 1 4 - 4 1 3	27.74	1.09×10^{-5}	1.0365	0.0846	6.318	0.0328	0.047	0.0032	0.0518	0.0055
140.1275	H ₂ CCO	42501	7 1 7 - 6 1 6	39.95	2.96×10^{-5}	1.3759	0.2371	6.2926	0.0993	0.0375	0.0055	0.0549	0.0124
142.7689	H ₂ CCO	42501	7 1 6 - 6 1 5	40.46	3.13×10^{-5}	0.8304	0.177	6.5126	0.0783	0.0466	0.0088	0.0412	0.0117
85.3479	HCS ⁺	45506	2 - 1	6.14	1.11×10^{-5}	1.4625	0.0731	6.6913	0.0318	0.0507	0.0022	0.079	0.0052
101.4778	H ₂ CS	46509	3 1 3 - 2 1 2	22.91	1.26×10^{-5}	1.2996	0.0472	6.5797	0.0196	0.0987	0.0031	0.1365	0.0066
103.0404	H ₂ CS	46509	3 0 3 - 2 0 2	9.89	1.48×10^{-5}	1.2056	0.0662	6.6341	0.0271	0.0695	0.0032	0.0892	0.0064
104.617	H ₂ CS	46509	3 1 2 - 2 1 1	23.21	1.38×10^{-5}	1.3077	0.0478	6.6409	0.0199	0.0924	0.0029	0.1287	0.0062
135.2983	H ₂ CS	46509	4 1 4 - 3 1 3	29.4	3.27×10^{-5}	1.2714	0.1088	6.5431	0.0457	0.083	0.0061	0.1123	0.0127
137.3712	H ₂ CS	46509	4 0 4 - 3 0 3	16.48	3.65×10^{-5}	1.5378	0.221	6.7233	0.0928	0.0549	0.0068	0.0898	0.0117
139.4837	H ₂ CS	46509	4 1 3 - 3 1 2	29.91	3.58×10^{-5}	1.5708	0.1332	6.8413	0.0558	0.0719	0.0052	0.1202	0.0134
100.5985	H ₂ C ³³ S	47506	3 1 3 3 5 - 2 1 2 2 . 5	22.83	1.05×10^{-5}	1.0832	0.1875	6.7737	0.0892	0.0193	0.003	0.0223	0.0052
85.5315	HOCO ⁺	45522	4 0 4 - 3 0 3	10.26	2.36×10^{-5}	1.447	0.2183	6.5053	0.0894	0.0216	0.0028	0.0333	0.0066
106.9135	HOCO ⁺	45522	5 0 5 - 4 0 4	15.39	4.71×10^{-5}	1.4084	0.2902	6.6109	0.1224	0.0161	0.0029	0.0242	0.0066
83.9006	HOCN	43510	4 0 4 - 3 0 3	10.07	4.22×10^{-5}	2.1866	0.458	6.3093	0.1847	0.0083	0.0014	0.0194	0.0052
104.8747	HOCN	43510	5 0 5 - 4 0 4	15.1	8.42×10^{-5}	1.8967	0.4506	6.1099	0.1885	0.0063	0.0013	0.0128	0.004
85.9248	NH ₂ D	18501	1 1 1 0 0 - 1 0 1 1 1	20.73	7.80×10^{-6}	0.8075	0.0603	6.3697	0.027	0.1255	0.0078	0.1079	0.0105
85.9257	NH ₂ D	18501	1 1 1 0 2 - 1 0 1 1 1	20.73	1.95×10^{-6}	0.8535	0.0229	6.2586	0.016	0.1674	0.0036	0.1521	0.0052
85.9263	NH ₂ D	18601	1 1 1 0 2 - 1 0 1 1 2	20.73	5.85×10^{-6}	0.8607	0.0146	6.2933	0.0111	0.4862	0.0069	0.4455	0.0099
85.9263	NH ₂ D	18501	1 1 1 0 1 - 1 0 1 1 1	20.73	1.95×10^{-6}	-	-	-	-	-	-	-	-
85.9269	NH ₂ D	18501	1 1 1 0 1 - 1 0 1 1 2	20.73	3.25×10^{-6}	0.8337	0.0195	6.3453	0.0153	0.1711	0.0032	0.1519	0.0045
85.9277	NH ₂ D	18501	1 1 1 0 1 - 1 0 1 1 0	20.73	2.60×10^{-6}	0.7573	0.2132	6.2022	0.0114	0.1379	0.0436	0.1111	0.047
110.1521	NH ₂ D	18501	1 1 1 0 0 - 1 0 1 0 1	21.31	1.65×10^{-5}	1.1071	0.1048	6.2361	0.0416	0.0462	0.0036	0.0545	0.0067
110.1530	NH ₂ D	18501	1 1 1 1 2 - 1 0 1 0 1	21.31	4.12×10^{-6}	0.9693	0.0945	6.2357	0.032	0.0576	0.0042	0.0594	0.0072
110.1536	NH ₂ D	18501	1 1 1 1 2 - 1 0 1 0 2	21.31	1.23×10^{-5}	0.8548	0.0222	6.2715	0.01	0.1851	0.0041	0.1685	0.0058
110.1542	NH ₂ D	18501	1 1 1 1 1 - 1 0 1 0 2	21.31	6.85×10^{-6}	1.0793	0.0885	6.3274	0.0377	0.0537	0.0037	0.0617	0.0066

Table A.1 continued

Freq. (GHz)	Species	Tag	Transition	E_{up} (K)	A_{ij} (s $^{-1}$)	FWHM (km s $^{-1}$)	v (km s $^{-1}$)	δv (km s $^{-1}$)	Int (K)	δInt (K)	Flux (K km s $^{-1}$)	δFlux (K km s $^{-1}$)
110.155	NH ₂ D	18501	1 1 1 1 1 - 1 0 1 0 0	21.31	5.49×10^{-6}	0.7911	0.0886	6.1538	0.0393	0.0534	0.005	0.045
93.1716	N ₂ H ⁺	29506	1 1 0 - 0 1 1	4.47	3.63×10^{-5}	1.5746	0.0363	5.3850	0.0152	1.744	0.0345	2.9232
93.1719	N ₂ H ⁺	29506	1 1 2 - 0 1 1	4.47	5.62×10^{-6}	-	-	6.3339	0.0154	-	-	0.0888
93.1719	N ₂ H ⁺	29506	1 1 2 - 0 1 2	4.47	3.07×10^{-5}	-	-	6.3339	0.0160	-	-	-
93.1720	N ₂ H ⁺	29506	1 1 1 - 0 1 0	4.47	1.85×10^{-5}	-	-	6.7751	0.0155	-	-	-
93.1720	N ₂ H ⁺	29506	1 1 1 - 0 1 1	4.47	4.33×10^{-6}	-	-	6.7751	0.0165	-	-	-
93.1720	N ₂ H ⁺	29506	1 1 1 - 0 1 2	4.47	1.35×10^{-5}	-	-	6.7751	0.0165	-	-	-
93.1735	N ₂ H ⁺	29506	1 2 2 - 0 1 1	4.47	3.07×10^{-5}	1.9781	0.0312	5.6839	0.013	2.2895	0.0308	4.8209
93.1735	N ₂ H ⁺	29506	1 2 2 - 0 1 2	4.47	5.62×10^{-6}	-	-	5.6839	0.0128	-	-	-
93.1738	N ₂ H ⁺	29506	1 2 3 - 0 1 2	4.47	3.63×10^{-5}	-	-	6.6379	0.0134	-	-	-
93.1740	N ₂ H ⁺	29506	1 2 1 - 0 1 0	4.47	1.14×10^{-5}	-	-	7.2624	0.0130	-	-	-
93.1740	N ₂ H ⁺	29506	1 2 1 - 0 1 1	4.47	2.35×10^{-5}	-	-	7.2625	0.0152	-	-	-
93.1740	N ₂ H ⁺	29506	1 2 1 - 0 1 2	4.47	1.43×10^{-6}	-	-	7.2624	0.0134	-	-	-
93.1763	N ₂ H ⁺	29506	1 0 1 - 0 1 0	4.47	6.46×10^{-6}	1.1068	0.0279	6.3655	0.0092	0.965	0.0192	1.1369
93.1763	N ₂ H ⁺	29506	1 0 1 - 0 1 1	4.47	8.45×10^{-6}	-	-	6.3655	0.0101	-	-	-
93.1763	N ₂ H ⁺	29506	1 0 1 - 0 1 2	4.47	2.14×10^{-5}	-	-	6.3655	0.0092	-	-	-
77.1075	N ₂ D ⁺	30509	1 1 0 - 0 1 1	3.7	2.06×10^{-5}	1.1393	0.0396	4.9053	0.0241	0.1109	0.0036	0.1345
77.1078	N ₂ D ⁺	30509	1 1 2 - 0 1 1	3.7	3.18×10^{-6}	-	-	6.0525	0.0253	-	-	-
77.1078	N ₂ D ⁺	30509	1 1 2 - 0 1 2	3.7	1.74×10^{-5}	-	-	6.0532	0.0244	-	-	-
77.1079	N ₂ D ⁺	30509	1 1 1 - 0 1 0	3.7	1.05×10^{-5}	-	-	6.5897	0.0241	-	-	-
77.1079	N ₂ D ⁺	30509	1 1 1 - 0 1 1	3.7	2.44×10^{-6}	-	-	6.5893	0.0282	-	-	-
77.1079	N ₂ D ⁺	30509	1 1 1 - 0 1 2	3.7	7.63×10^{-6}	-	-	6.5895	0.0278	-	-	-
77.1093	N ₂ D ⁺	30509	1 2 2 - 0 1 1	3.7	1.74×10^{-5}	1.9302	0.0545	5.3554	0.0227	0.1188	0.0029	0.244
77.1093	N ₂ D ⁺	30509	1 2 2 - 0 1 2	3.7	3.18×10^{-6}	-	-	5.3552	0.0241	-	-	-
77.1096	N ₂ D ⁺	30509	1 2 3 - 0 1 2	3.7	2.06×10^{-5}	-	-	6.5086	0.0238	-	-	-
77.1098	N ₂ D ⁺	30509	1 2 1 - 0 1 0	3.7	6.39×10^{-6}	-	-	7.2812	0.0238	-	-	-
77.1098	N ₂ D ⁺	30509	1 2 1 - 0 1 1	3.7	1.34×10^{-5}	-	-	7.2811	0.0230	-	-	-
77.1098	N ₂ D ⁺	30509	1 2 1 - 0 1 2	3.7	8.13×10^{-7}	-	-	7.2811	0.0236	-	-	-
77.1121	N ₂ D ⁺	30509	1 0 1 - 0 1 1	3.7	4.77×10^{-6}	0.9748	0.0843	6.3649	0.0614	0.0490	0.0036	0.0508
77.1121	N ₂ D ⁺	30509	1 0 1 - 0 1 2	3.7	1.21×10^{-5}	-	-	6.3621	0.1269	-	-	-
77.1121	N ₂ D ⁺	30509	1 0 1 - 0 1 0	3.7	3.67×10^{-6}	-	-	6.2976	0.0614	-	-	-
154.2150	N ₂ D ⁺	30509	2 2 2 - 1 2 3	11.1	7.63×10^{-6}	1.2691	0.1057	5.4496	0.0443	0.0543	0.0039	0.0733
154.2154	N ₂ D ⁺	30509	2 2 1 - 1 2 1	11.1	5.88×10^{-5}	-	-	5.7023	0.0445	-	-	-
154.2154	N ₂ D ⁺	30509	2 2 3 - 1 2 3	11.1	4.96×10^{-5}	-	-	5.9399	0.0451	-	-	-
154.2153	N ₂ D ⁺	30509	2 2 1 - 1 2 2	11.1	1.95×10^{-5}	-	-	6.0263	0.0451	-	-	-
154.2153	N ₂ D ⁺	30509	2 1 1 - 1 0 1	11.1	1.06×10^{-4}	-	-	6.2031	0.0456	-	-	-
154.2156	N ₂ D ⁺	30509	2 1 2 - 1 0 1	11.1	1.10×10^{-4}	-	-	6.6017	0.0441	-	-	-
154.2156	N ₂ D ⁺	30509	2 2 1 - 1 2 2	11.1	9.44×10^{-6}	-	-	6.6659	0.0446	-	-	-
154.2156	N ₂ D ⁺	30509	2 2 3 - 1 2 2	11.1	6.26×10^{-6}	-	-	6.5169	0.0449	-	-	-
154.2159	N ₂ D ⁺	30509	2 1 0 - 1 0 1	11.1	1.16×10^{-4}	-	-	7.1206	0.0453	-	-	-

Table A.1 continued

Freq. (GHz)	Species	Tag	Transition	E_{up} (K)	A_{ij} (s $^{-1}$)	FWHM (km s $^{-1}$)	δFWHM (km s $^{-1}$)	ν (km s $^{-1}$)	$\delta\nu$ (km s $^{-1}$)	Int (K)	δInt (K)	Flux (K km s $^{-1}$)	δFlux (K km s $^{-1}$)
154.2167	N ₂ D ⁺	30509	2 2 2 - 1 1 1	11.1	1.18 × 10 $^{-4}$	-	-	5.4529	0.0134	0.2343	0.0082	0.1936	0.0147
154.2168	N ₂ D ⁺	30509	2 3 3 - 1 2 3	11.1	1.62 × 10 $^{-5}$	-	-	5.5740	0.0136	-	-	-	-
154.2169	N ₂ D ⁺	30509	2 2 2 - 1 1 2	11.1	4.90 × 10 $^{-5}$	-	-	5.7212	0.0137	-	-	-	-
154.2170	N ₂ D ⁺	30509	2 2 1 - 1 1 1	11.1	3.37 × 10 $^{-5}$	-	-	6.0918	0.0134	-	-	-	-
154.2171	N ₂ D ⁺	30509	2 3 3 - 1 2 2	11.1	1.81 × 10 $^{-4}$	-	-	6.1501	0.0135	-	-	-	-
154.2171	N ₂ D ⁺	30509	2 3 2 - 1 2 1	11.1	1.56 × 10 $^{-4}$	-	-	6.1942	0.0130	-	-	-	-
154.2171	N ₂ D ⁺	30509	2 2 3 - 1 1 2	11.1	1.42 × 10 $^{-4}$	-	-	6.2111	0.0139	-	-	-	-
154.2172	N ₂ D ⁺	30509	2 3 4 - 1 2 3	11.1	1.97 × 10 $^{-4}$	-	-	6.3436	0.0134	-	-	-	-
154.2175	N ₂ D ⁺	30509	2 2 1 - 1 1 0	11.1	9.24 × 10 $^{-5}$	-	-	6.9343	0.0133	-	-	-	-
154.2176	N ₂ D ⁺	30509	2 3 2 - 1 2 2	11.1	3.79 × 10 $^{-5}$	-	-	7.1574	0.0131	-	-	-	-
154.2181	N ₂ D ⁺	30509	2 1 2 - 1 2 3	11.1	4.50 × 10 $^{-6}$	-	-	8.1211	0.0133	-	-	-	-
154.2196	N ₂ D ⁺	30509	2 1 1 - 1 1 1	11.1	3.09 × 10 $^{-5}$	0.8769	0.1677	5.6292	0.0715	0.0247	0.0041	0.0231	0.0058
154.2197	N ₂ D ⁺	30509	2 1 1 - 1 1 2	11.1	3.96 × 10 $^{-5}$	-	-	5.8976	0.0709	-	-	-	-
154.2198	N ₂ D ⁺	30509	2 1 2 - 1 1 1	11.1	2.47 × 10 $^{-5}$	-	-	6.0276	0.0710	-	-	-	-
154.2199	N ₂ D ⁺	30509	2 1 2 - 1 1 2	11.1	5.56 × 10 $^{-5}$	-	-	6.2962	0.0708	-	-	-	-
154.2200	N ₂ D ⁺	30509	2 1 1 - 1 1 0	11.1	1.73 × 10 $^{-5}$	-	-	6.4710	0.0713	-	-	-	-
154.2201	N ₂ D ⁺	30509	2 1 0 - 1 1 1	11.1	7.32 × 10 $^{-5}$	-	-	6.5463	0.0710	-	-	-	-
115.5246	NS	46515	3 - 1 2.5 1.5 - 2 1 1.5	8.89	5.65 × 10 $^{-6}$	0.9086	0.205	6.8745	0.1015	0.0361	0.0075	0.0349	0.0107
72.9768	OCS	60503	6 - 5	12.26	1.07 × 10 $^{-6}$	3.8139	1.3639	6.3449	0.6485	0.015	0.0022	0.0609	0.0235
72.9768	OCS	60503	6 - 5	12.26	1.07 × 10 $^{-6}$	1.7904	1.1207	9.1125	0.4403	0.009	0.0059	0.0172	0.0156
85.1391	OCS	60503	7 - 6	16.34	1.71 × 10 $^{-6}$	4.3501	0.6374	6.3099	0.3386	0.0188	0.0016	0.0871	0.0148
85.1391	OCS	60503	7 - 6	16.34	1.71 × 10 $^{-6}$	1.276	0.3463	8.5335	0.0908	0.0185	0.0039	0.0251	0.0086
97.3012	OCS	60503	8 - 7	21.01	2.58 × 10 $^{-6}$	3.9536	0.6245	6.3435	0.3281	0.0215	0.0015	0.0903	0.0156
97.3012	OCS	60503	8 - 7	21.01	2.58 × 10 $^{-6}$	1.4444	0.2734	8.6227	0.0746	0.0238	0.0046	0.0367	0.0099
109.4631	OCS	60503	9 - 8	26.27	3.70 × 10 $^{-6}$	4.9584	0.4109	6.7041	0.2145	0.0267	0.0019	0.1408	0.0154
109.4631	OCS	60503	9 - 8	26.27	3.70 × 10 $^{-6}$	0.788	0.2742	8.5396	0.0609	0.0287	0.0062	0.0241	0.0099
145.9468	OCS	60503	12 - 11	45.53	8.88 × 10 $^{-6}$	0.5159	0.4199	6.2249	0.1323	0.0653	0.0358	0.0359	0.0352
145.9468	OCS	60503	12 - 11	45.53	8.88 × 10 $^{-6}$	2.3657	0.6212	7.8116	0.2376	0.0699	0.0109	0.1759	0.0537
158.1074	OCS	60503	13 - 12	53.12	1.13 × 10 $^{-5}$	2.1464	0.2452	4.8175	0.118	0.0496	0.0036	0.1133	0.0153
158.1074	OCS	60503	13 - 12	53.12	1.13 × 10 $^{-5}$	2.9129	0.2335	7.8807	0.1007	0.0701	0.0029	0.2175	0.0196
106.7874	OC ³⁴ S	62505	9 - 8	25.63	3.44 × 10 $^{-6}$	2.2436	0.9101	6.8835	0.3586	0.0068	0.0022	0.0163	0.0085
86.0939	SO	48501	2 2 - 1 1	19.31	5.25 × 10 $^{-6}$	1.3286	0.067	6.4479	0.028	0.0714	0.0031	0.101	0.0067
99.2999	SO	48501	2 3 - 1 2	9.23	1.13 × 10 $^{-5}$	1.43	0.0159	6.4155	0.0067	0.4583	0.0044	0.6976	0.0102
100.0296	SO	48501	5 4 - 4 4	38.58	1.08 × 10 $^{-6}$	2.0931	0.3477	6.9242	0.1452	0.0173	0.0025	0.0386	0.0085
109.2522	SO	48501	3 2 - 2 1	21.05	1.08 × 10 $^{-5}$	1.5927	0.0478	6.6101	0.02	0.1073	0.0028	0.182	0.0072
138.1786	SO	48501	3 4 - 2 3	15.86	3.17 × 10 $^{-5}$	1.3817	0.0241	6.327	0.0101	0.5583	0.0084	0.8211	0.0189
158.9718	SO	48501	4 3 - 3 2	28.68	4.23 × 10 $^{-5}$	1.5708	0.0307	6.4958	0.0129	0.3429	0.0057	0.5733	0.0147
97.7153	³⁴ SO	50501	2 3 - 1 2	9.09	1.07 × 10 $^{-5}$	1.4251	0.2671	6.2182	0.1118	0.0155	0.0025	0.0236	0.0058
135.7757	³⁴ SO	50501	3 4 - 2 3	15.61	3.00 × 10 $^{-5}$	1.4094	0.2404	6.6969	0.1011	0.0368	0.0054	0.0553	0.0124
104.0294	SO ₂	64502	3 1 3 - 2 0 2	7.74	1.01 × 10 $^{-5}$	1.5138	0.2605	6.3711	0.1091	0.0192	0.0028	0.0309	0.007

Table A.1 continued

Freq. (GHz)	Species	Tag	Transition	E_{up} (K)	A_{ij} (s $^{-1}$)	FWHM (km s $^{-1}$)	δFWHM (km s $^{-1}$)	v (km s $^{-1}$)	δv (km s $^{-1}$)	Int (K)	δInt (K)	Flux (K km s $^{-1}$)	δFlux (K km s $^{-1}$)
104.2393	SO ₂	64502	10 1 9 – 10 0 10	54.71	1.12×10^{-5}	1.4989	0.8661	8.2976	0.3503	0.0076	0.0027	0.0121	0.0082
135.696	SO ₂	64502	5 1 5 – 4 0 4	15.66	2.21×10^{-5}	1.8259	0.3714	6.5288	0.1554	0.0313	0.0055	0.0608	0.0163
151.3786	SO ₂	64502	2 2 0 – 2 1 1	12.58	1.87×10^{-5}	1.1768	0.2715	6.4535	0.114	0.0172	0.0034	0.0215	0.0065
158.1997	SO ₂	64502	3 2 2 – 3 1 3	15.34	2.53×10^{-5}	1.3234	0.2433	6.5312	0.1019	0.0242	0.0038	0.0341	0.0082

Appendix B: Fits of the data

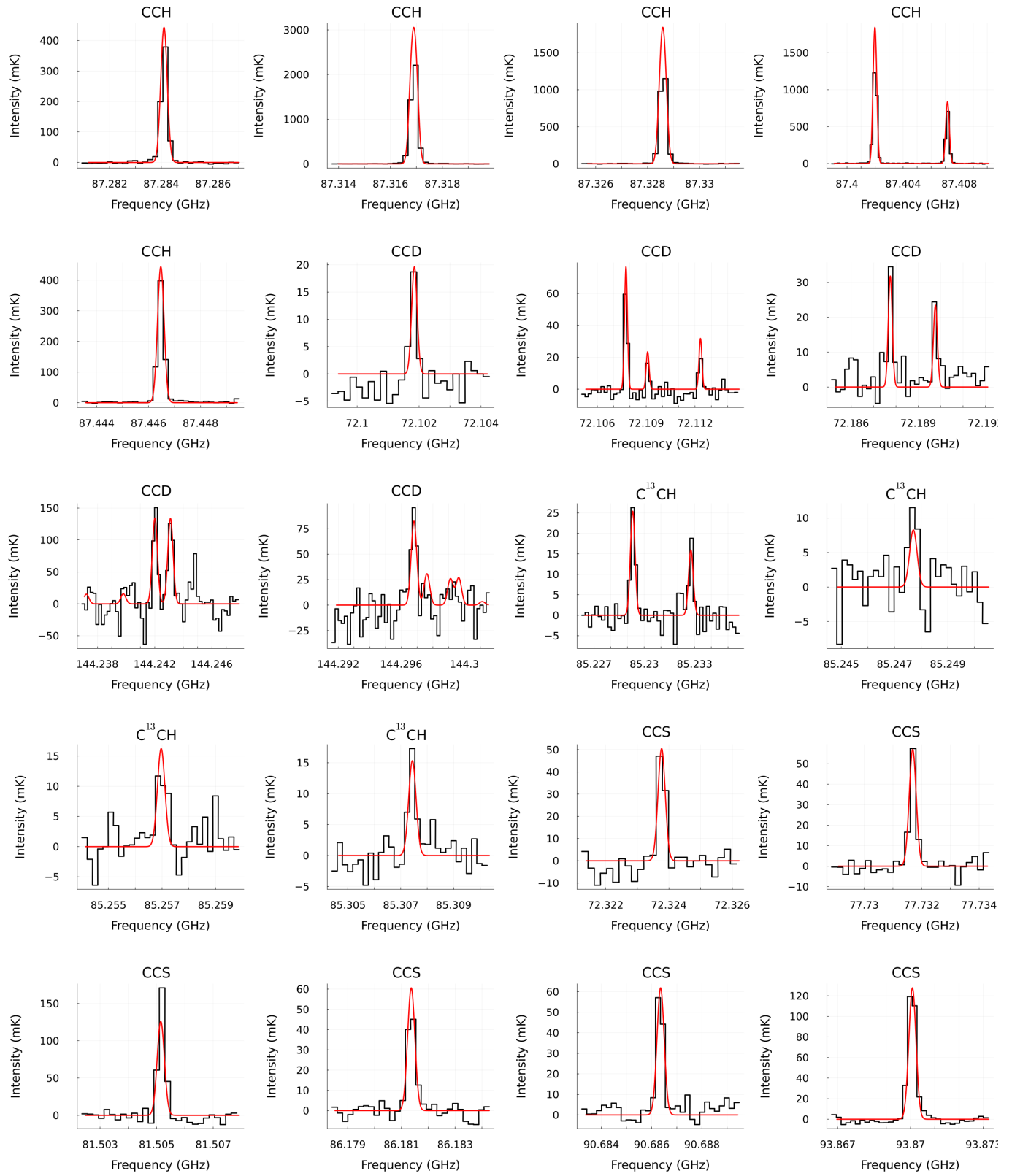
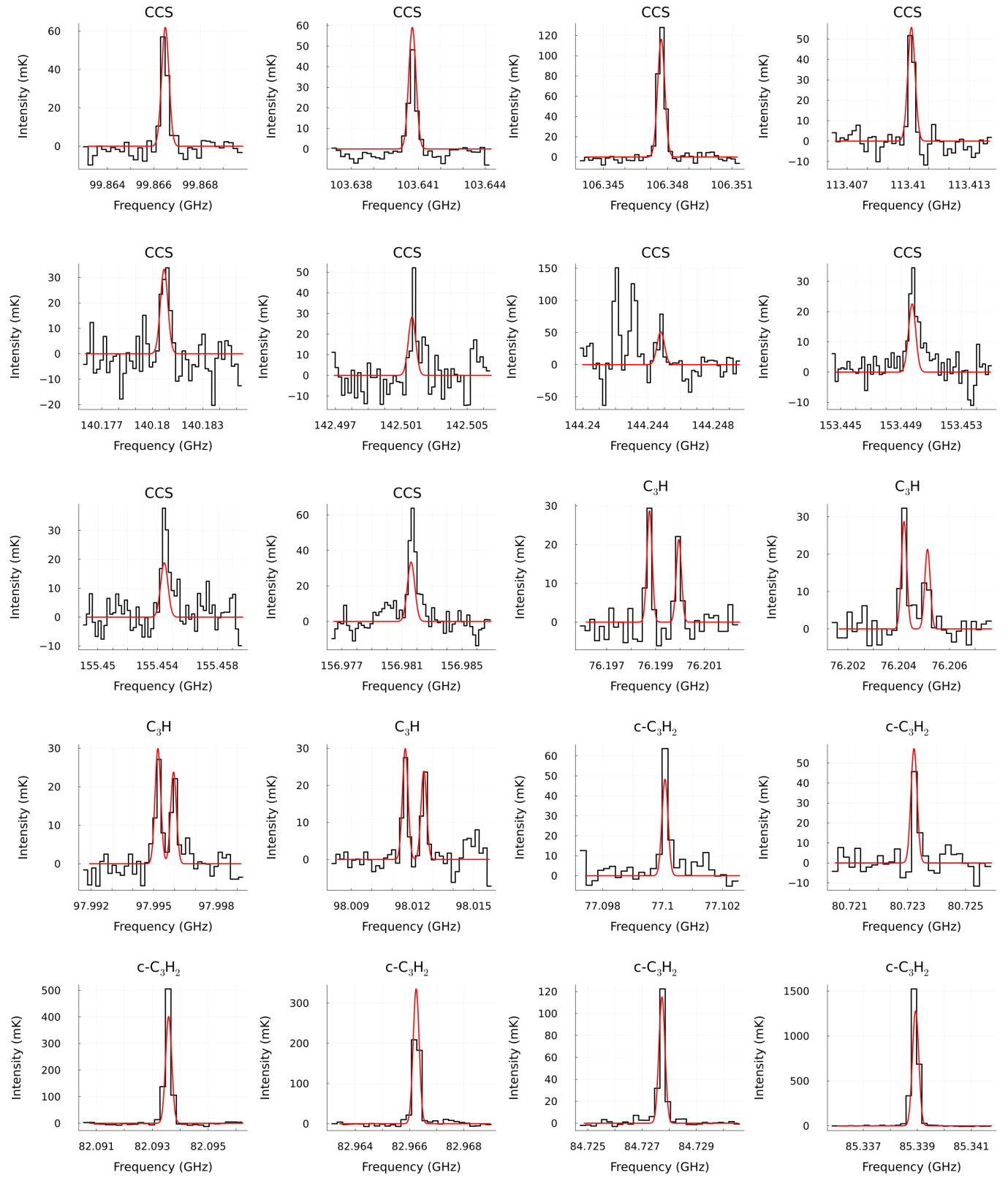


Fig. B.1: Observed spectrum (black histogram) and LTE radiative transfer model of the transition lines (red curves), for species listed in Table 3.

**Fig. B.1 continued.**

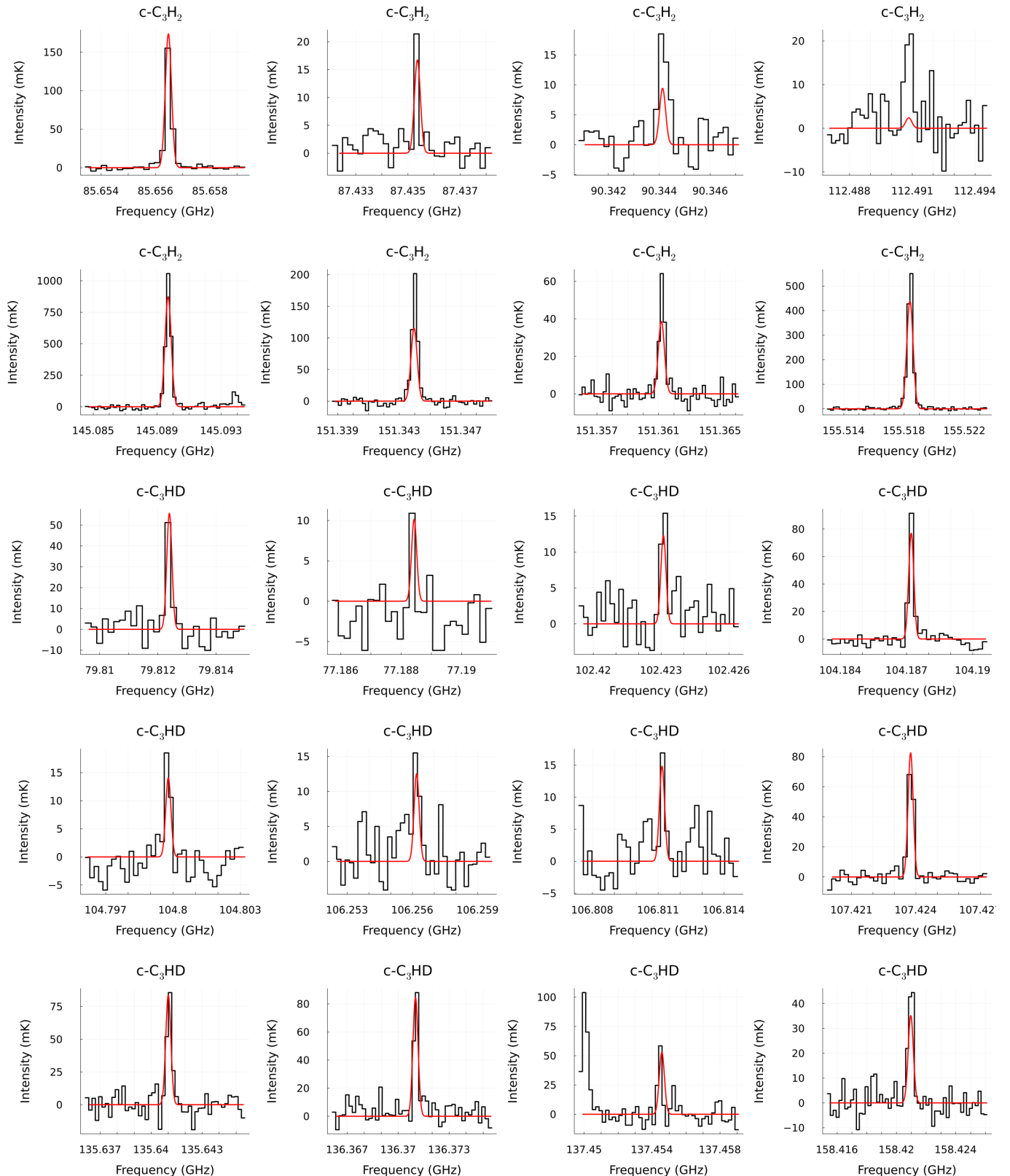
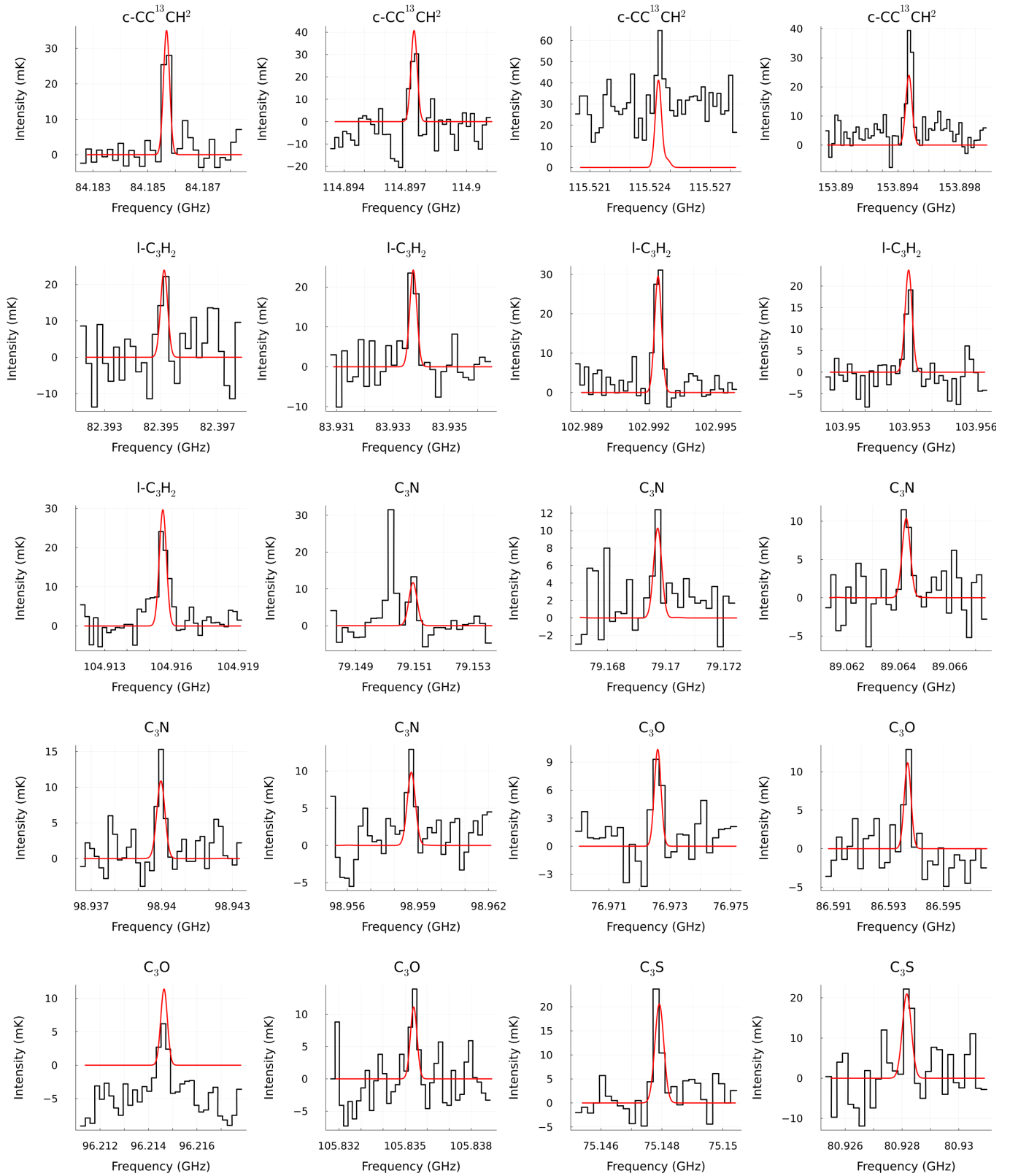


Fig. B.1 continued.

**Fig. B.1 continued.**

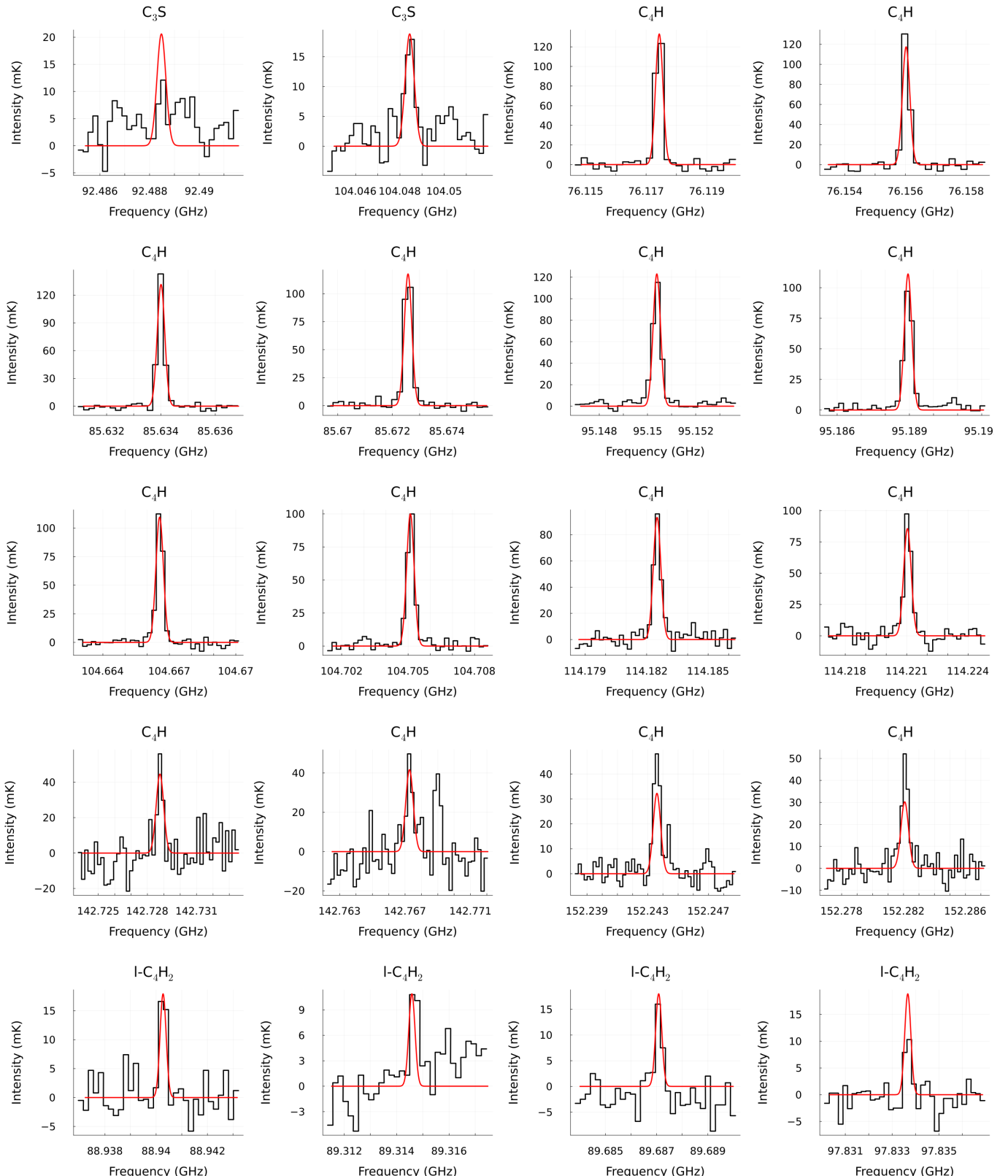
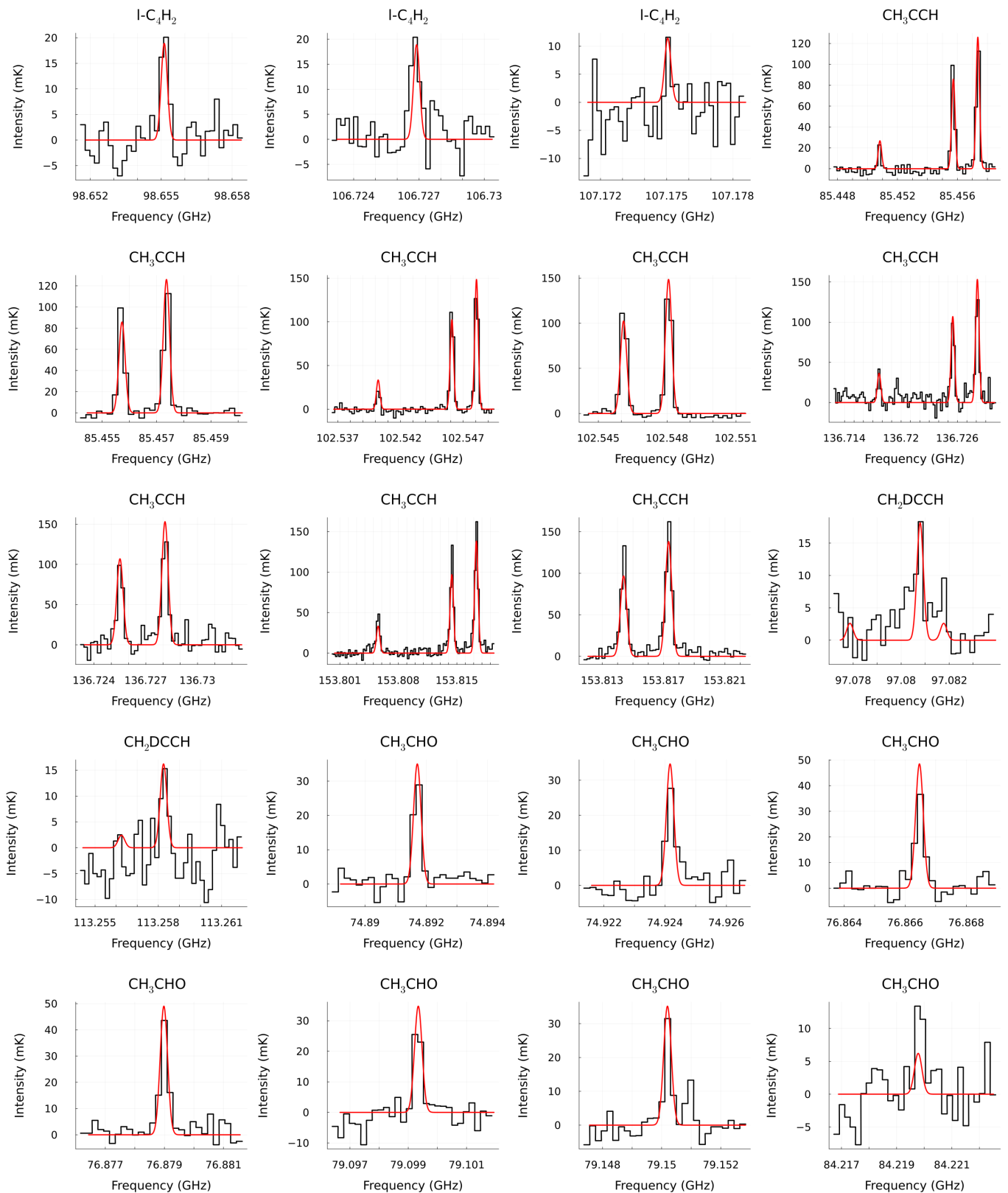


Fig. B.1 continued.

**Fig. B.1 continued.**

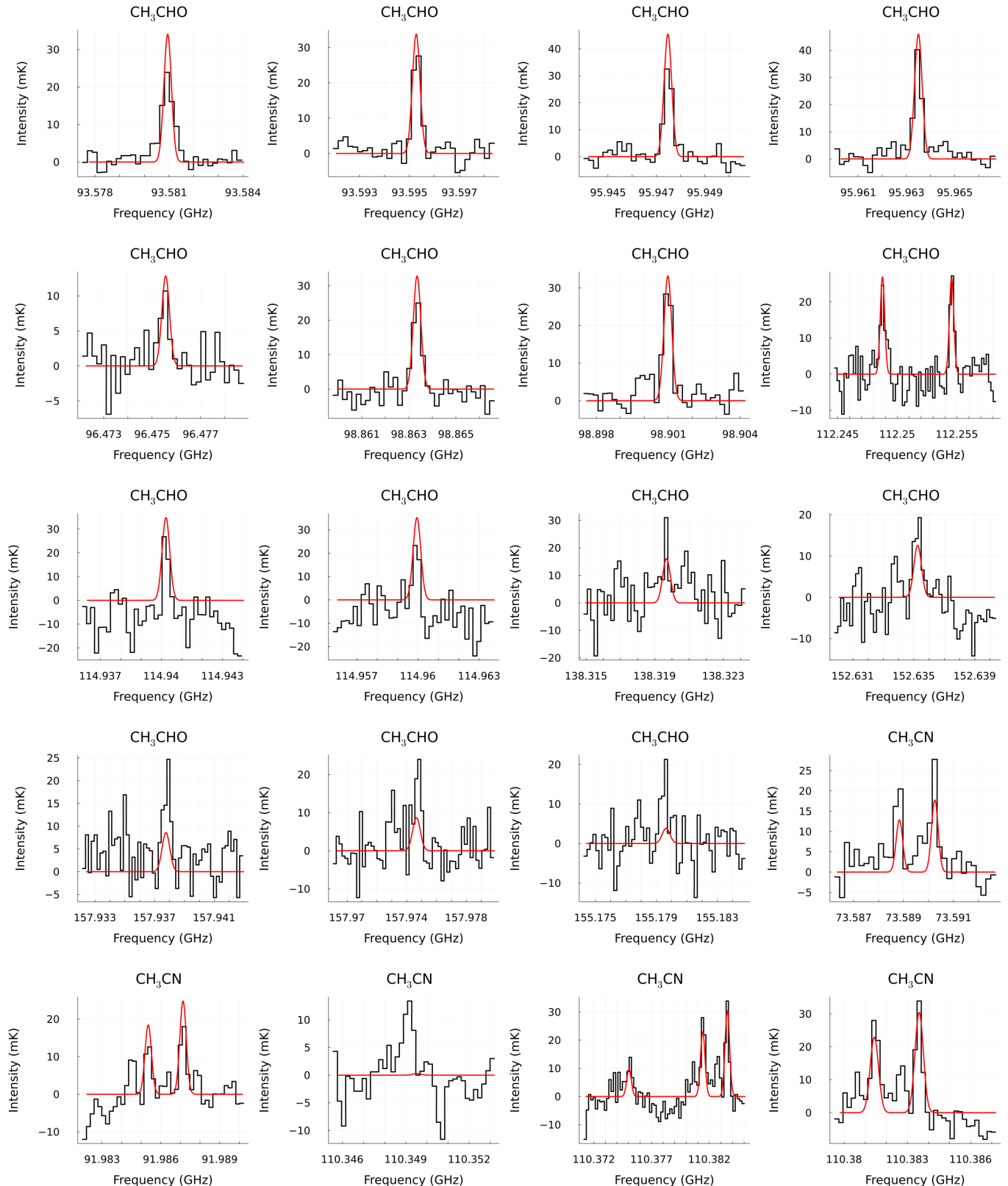


Fig. B.1 continued.

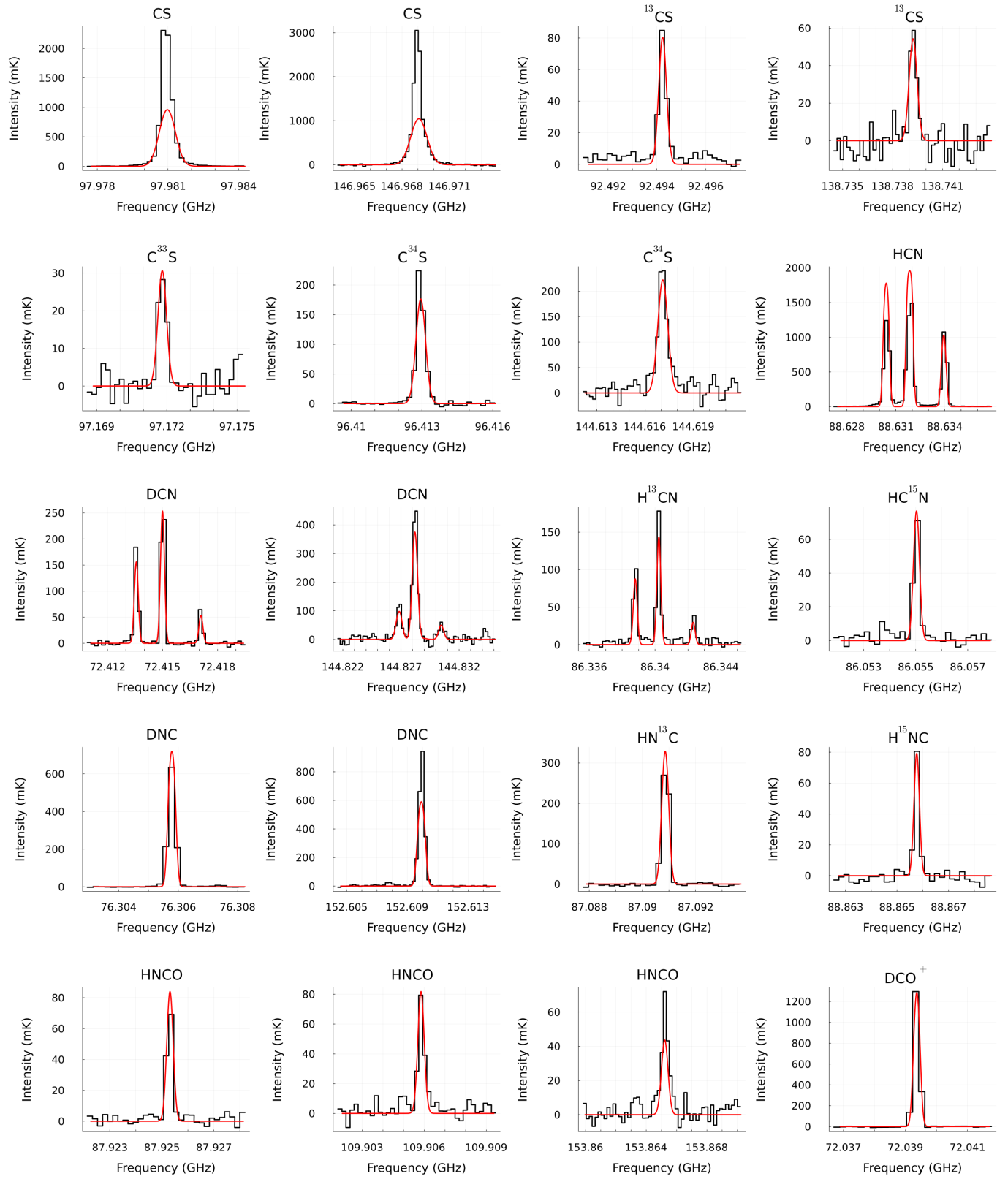


Fig. B.1 continued.

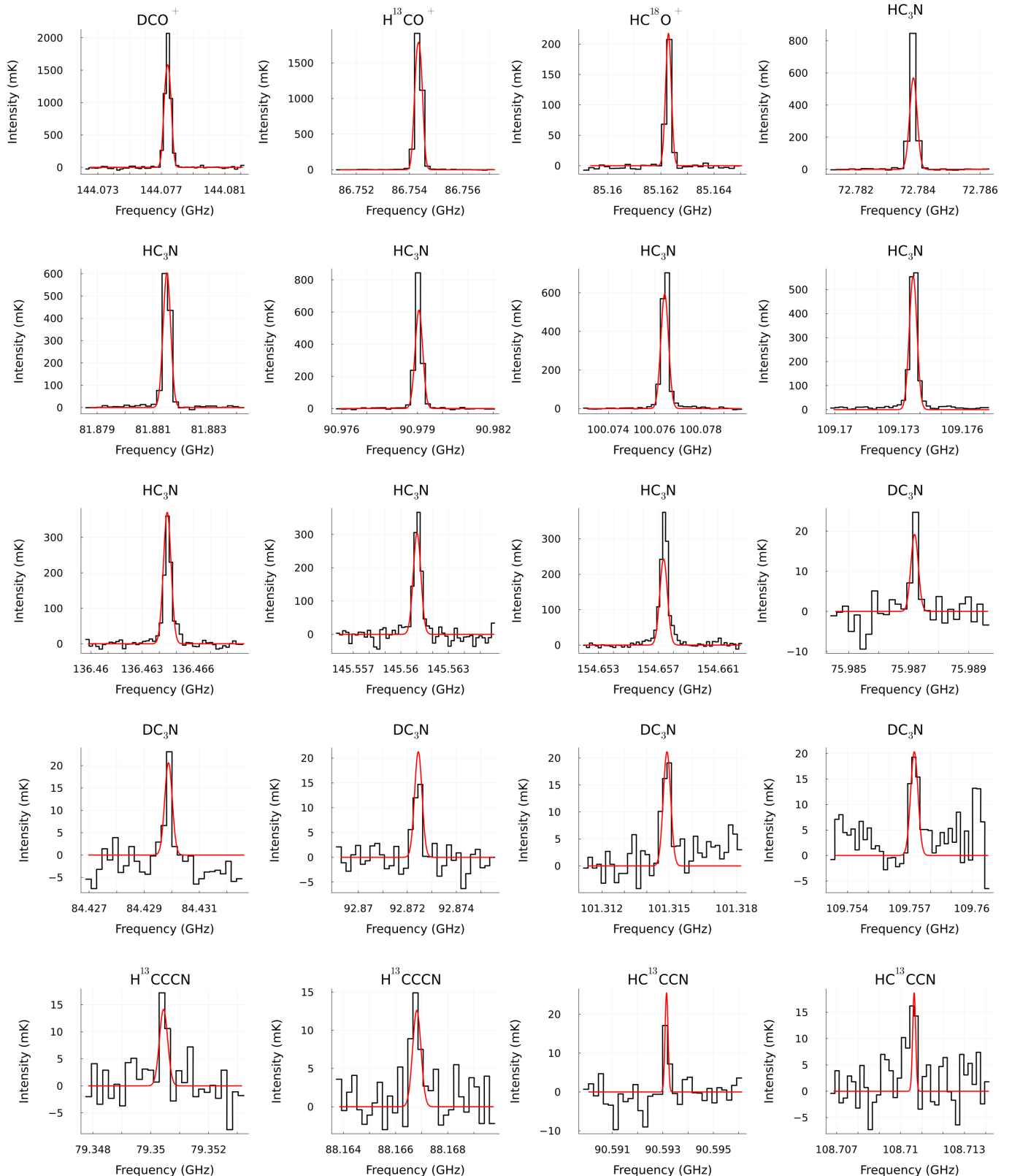
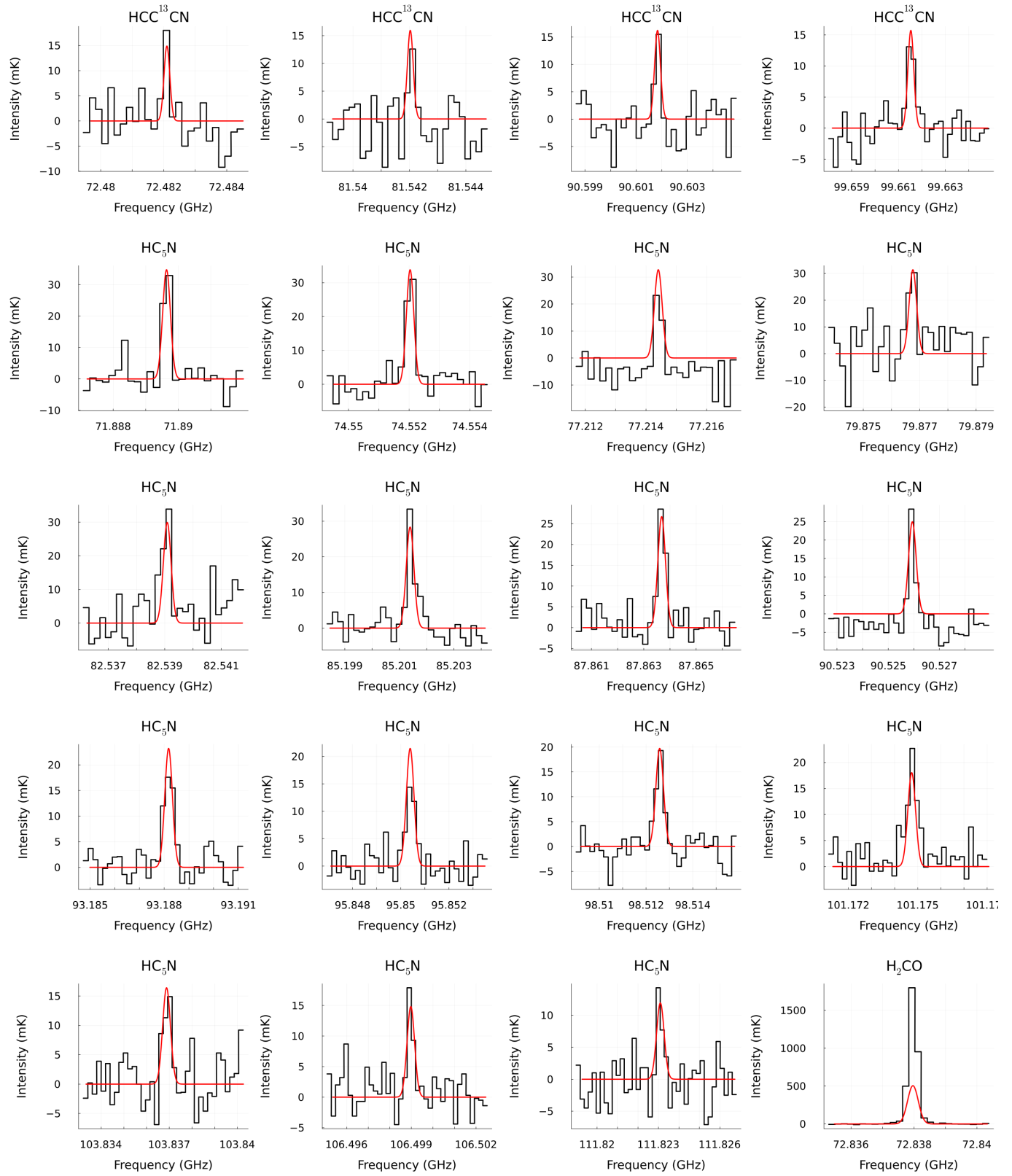


Fig. B.1 continued.

**Fig. B.1 continued.**

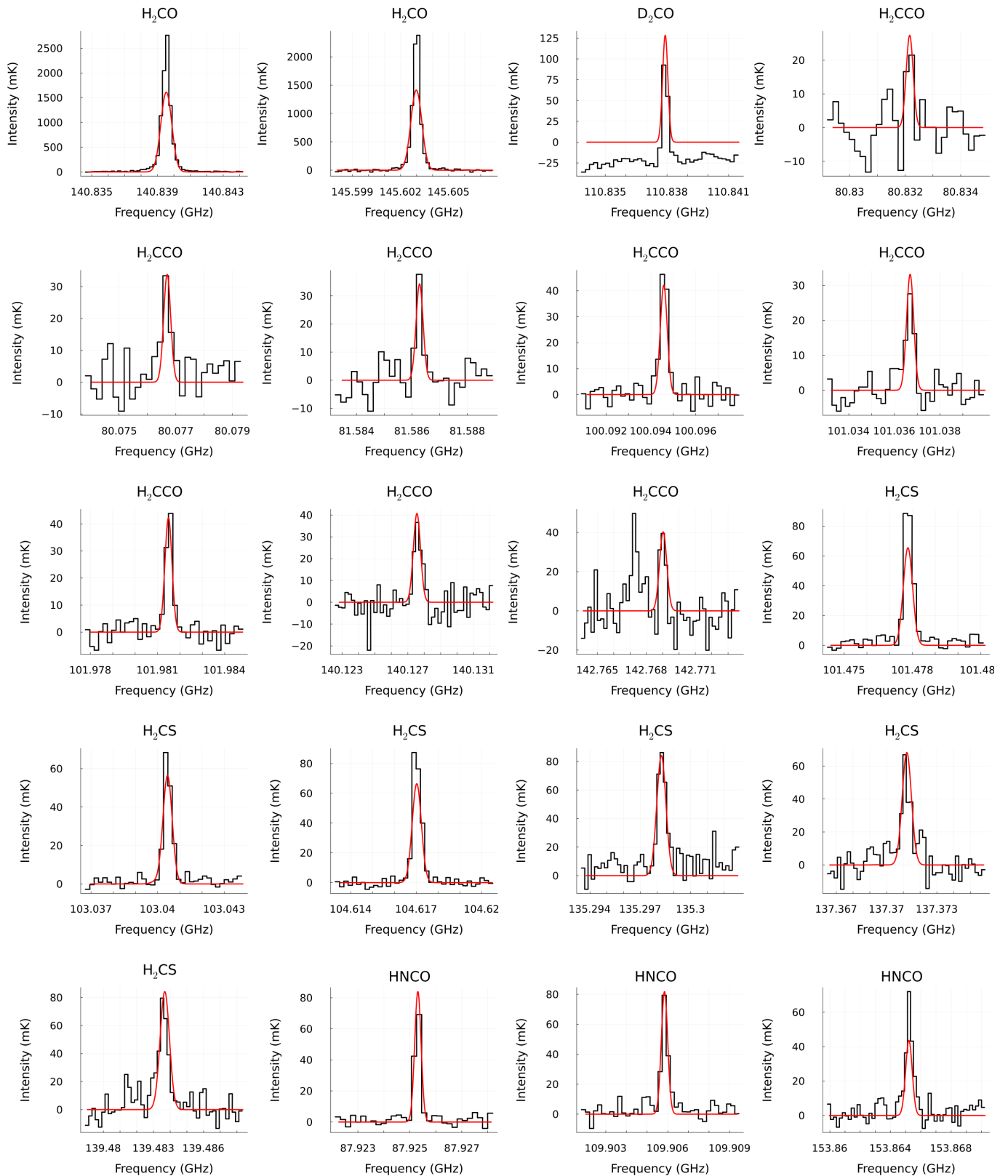


Fig. B.1 continued.

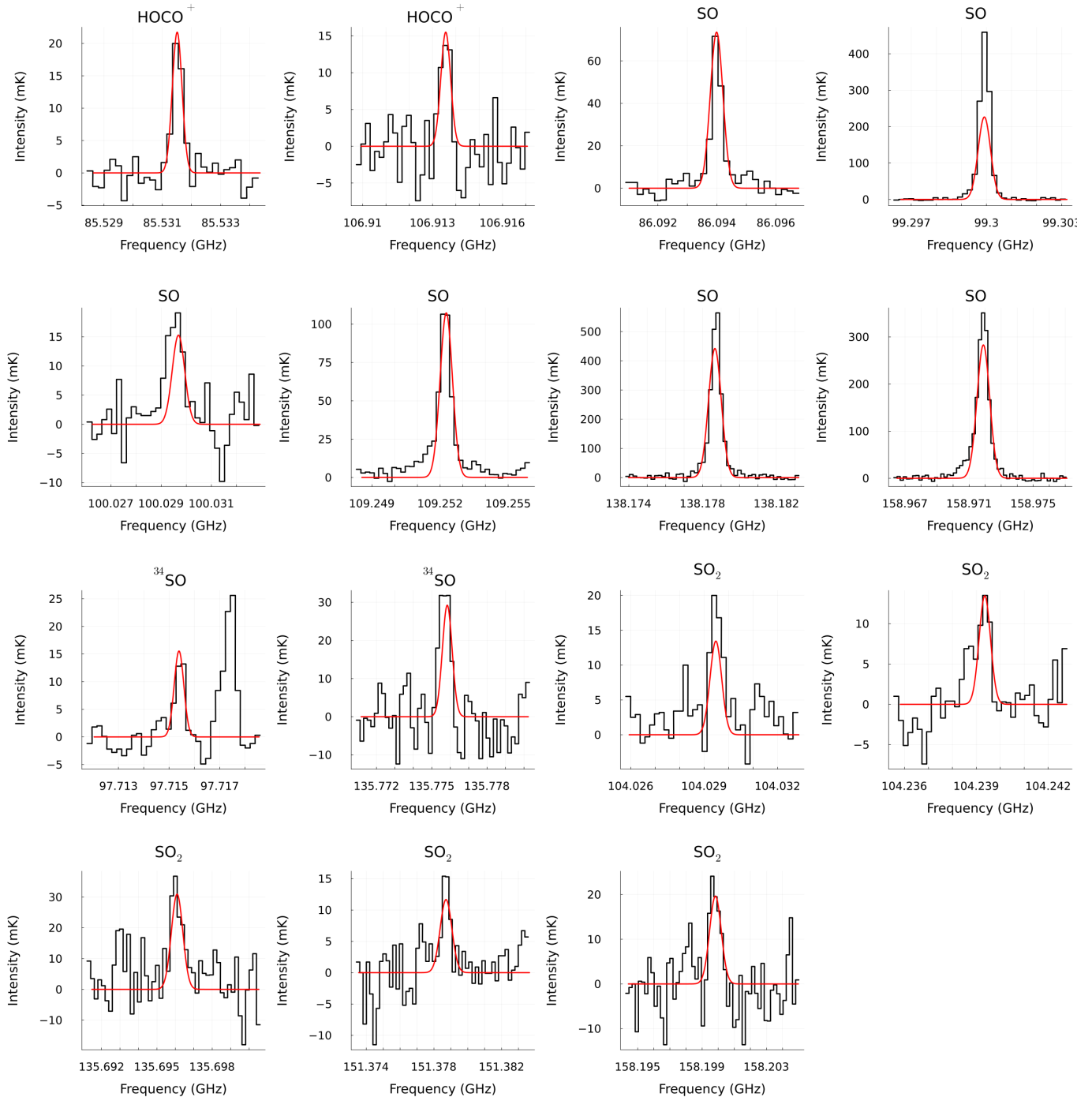


Fig. B.1 continued.

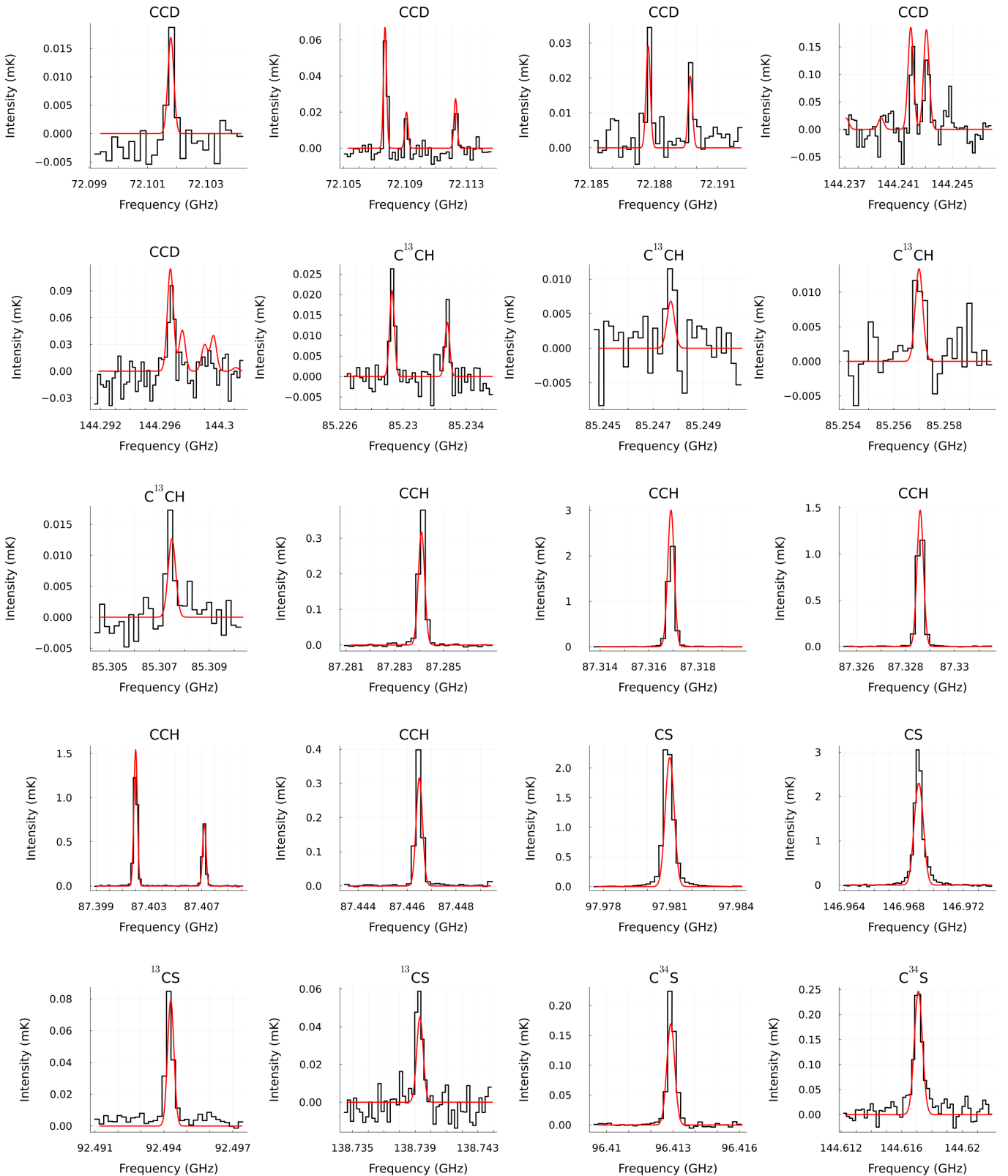
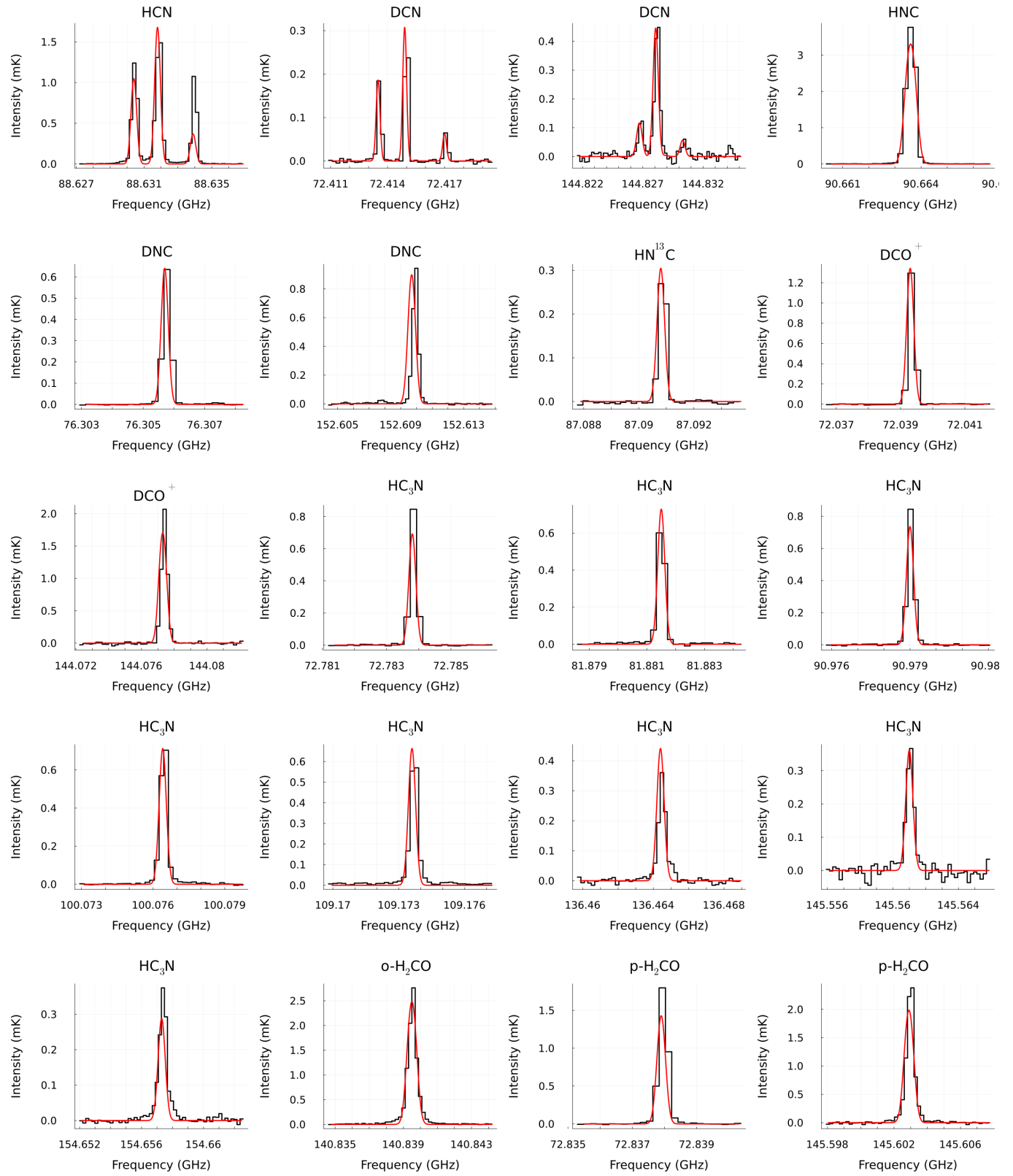


Fig. B.2: Same as Figure B.1 for the non-LTE radiative transfer models.

**Fig. B.2 continued.**

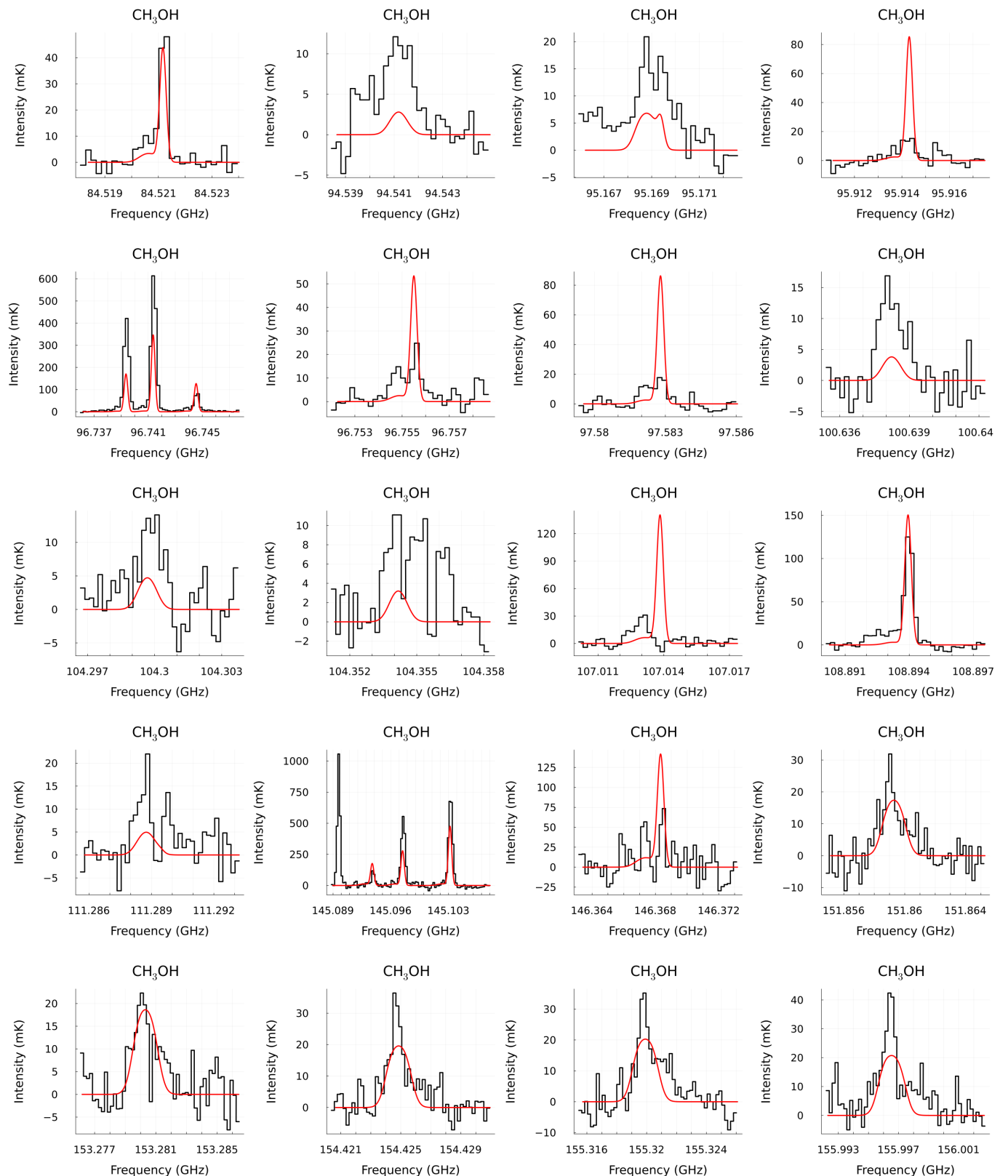
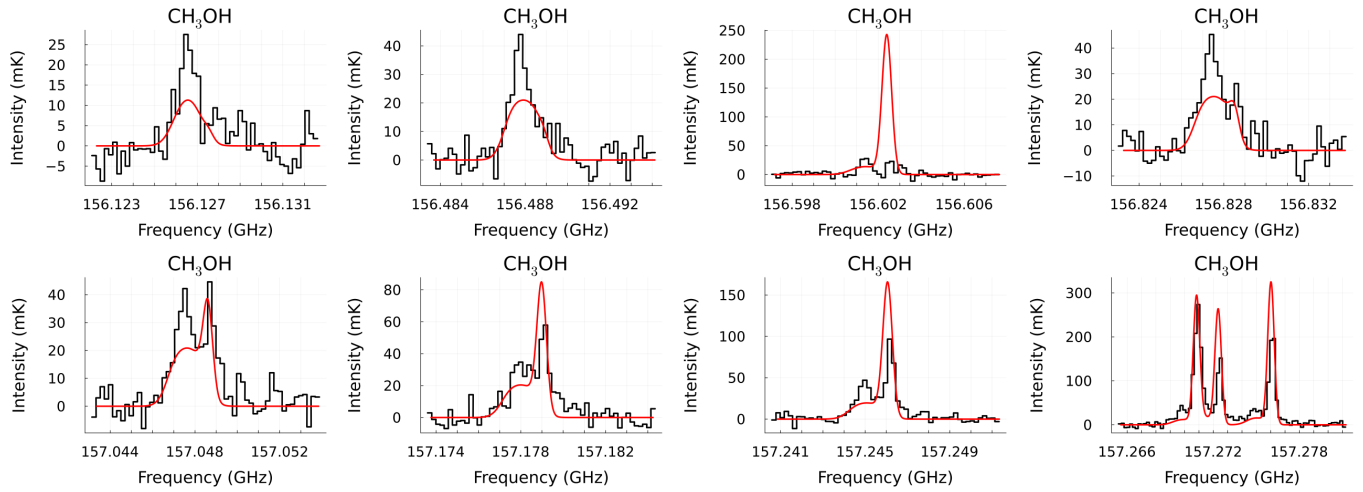


Fig. B.3: Reproduction of CH_3OH emission from its rotational diagram (see Sect. 3.2.3).

**Fig. B.3** continued.